

This file is part of the following work:

**Kazum, Oluwole (2018) *Mechanisms of hydrogen-induced cracking in ultrahigh-strength steels*. PhD Thesis, James Cook University.**

Access to this file is available from:

<https://doi.org/10.25903/5bfb5cd842ccb>

Copyright © 2018 Oluwole Kazum

The author has certified to JCU that they have made a reasonable effort to gain permission and acknowledge the owners of any third party copyright material included in this document. If you believe that this is not the case, please email

[researchonline@jcu.edu.au](mailto:researchonline@jcu.edu.au)

Mechanisms of hydrogen-induced cracking  
in ultrahigh-strength steels

Thesis submitted by

Oluwole Kazum (B. Eng, M. Phil)

July 2018

for the degree of  
Doctor of Philosophy (Chemical Engineering)  
in the College of Science and Engineering

James Cook University

## **Acknowledgements**

I express my appreciation to my academic supervisors, A/Prof. Bobby Mathan and Prof. Yinghe He for their support, advice and critical analysis of every stage of my work at James Cook University, Townsville. I also want to acknowledge the contributions of Dr. Hossein Beladi, for supplying some of the samples and for his contribution to technical discussions.

My thanks go to my entire family for their strong support and encouragement during my postgraduate studies. I express my gratitude to my immediate family, my wife, my children, my brother and his family for their encouragement throughout my study.

I am equally grateful for the assistance and words of reassurance from my colleagues R. Walter and A. Baloch. Furthermore, appreciation goes to the entire academic and administrative staff of the College of Science and Engineering, James Cook University, Townsville.

Finally, I wish to acknowledge the enormous financial support provided towards my research work at James Cook University by the Australian Government through the JCUIPRS and AINSE PGRA scholarship scheme.

## Statement on the Contribution of Others

| Nature of Assistance | Contribution                 | Names, Titles and Affiliations of Co-Contributors  |
|----------------------|------------------------------|--|
| Intellectual support | Supervisory Assistance       | A/Prof. Bobby Mathan, College of Science and Engineering, James Cook University                                  |
|                      |                              | Prof. Yinghe He, College of Science and Engineering, James Cook University                                       |
|                      |                              | Dr. Hossein Beladi (Institute for Frontier Materials, Deakin University).  |
|                      | Editorial Assistance         | A/Prof. Bobby Mathan, College of Science and Engineering, James Cook University                                  |
|                      | Experimental Assistance      | Katharine J Fowler, language editing and formatting  |
|                      | SEM micrographs              | Shane Askew, Advanced Analytical Centre (AAC) of James Cook University   |
| Financial support    | Hydrogen depth profiling     | Dr. Mihail Ionescu at the Centre for Accelerator Science, Australian Nuclear Science and Technology Organization |
|                      | Fee offset/waiver            | Postgraduate Research Scholarship Award (JCUIPRS) and the Australian Government through James Cook University.   |
|                      | Stipend                      |  |
|                      | Top-up scholarship (stipend) | AINSE PGRA Scholarship scheme.   |

## **Abstract**

There has been a significant increase in the application of high-strength steels in the engineering and offshore industry. Nanostructured bainitic steels (BS-200 and BS-350) and austenitic twinning-induced plasticity (TWIP) steel have emerged as two promising materials for engineering and offshore applications, due to their extraordinary mechanical properties. Generally, steel corrosion is a major problem, especially in the offshore industry. Hence, several corrosion protection techniques such as protective coating, alloying and cathodic protection have widely been employed. The cathodic protection system is preferred by corrosion experts in the offshore industry as it provides a more effective method of protecting steels from general corrosion. However, high-strength metallic materials, in general, are prone to a localized form of corrosion known as hydrogen-induced cracking (HIC).

The diffusion of hydrogen can occur during the cathodic protection potentials and cause catastrophic failure of the material under tensile loading. HIC undermines the integrity of structural components and leads to huge financial losses, as well as potential environmental pollution. The degree of HIC susceptibility is influenced by the microstructure of the material. Generally, steels containing a predominantly ferrite phase are more susceptible to HIC than those containing an austenite phase. Ultrahigh-strength steels generally contain refined microstructures with different phases, grain sizes and other features such as dislocations, twinning and precipitates. These features can trap or enhance the mobility of hydrogen and thus affect the steel's susceptibility to HIC. Therefore, it is critical to study the HIC susceptibility of ultrahigh-strength nanostructured bainitic steels and TWIP steels to determine their potential applications for steel pipeline and structural components in the offshore oil industry. This thesis aims to determine the HIC susceptibility of these ultrahigh-strength steels by experimentally

calculating the hydrogen diffusivity in these materials, and by mechanical property testing in conducive environments.

Nanostructured bainitic steels comprised of refined microstructures including ferrite with a large component of dislocation density and austenite phases. The microstructural features contribute to the steel's superior tensile strength ( $> 800$  MPa) and ductility ( $\geq 30$  pct). To understand the HIC susceptibility of the nanostructured bainitic steels, electrochemical hydrogen permeation tests and micro-hardness tests were carried out on the steel, and the results were compared to those from a nominal mild steel. Electrochemical hydrogen permeation results showed that the nanostructured bainitic steel containing 79 pct of ferrite phase (BS-200) exhibited lower effective hydrogen diffusivity compared to steel containing 47 pct ferrite phase (BS-350) and mild steel by about two orders of magnitude. The effective hydrogen diffusivity for each steel was found to increase as the cathodic charging current density was increased. However, the increase was not significant in BS-200 compared to the other steels. This was attributed to the trapping effect of the refined microstructural constituents: bainitic ferrite laths, retained austenite films and higher dislocation density in the bainitic ferrite of the BS-200 steel.

In order to understand how hydrogen diffusion and hydrogen concentration in the steel affect the mechanical properties, micro-hardness tests were performed on charged samples. The results showed softening in nanostructured bainitic steel and hardening in mild steel. The BS-200 and BS-350 nanostructured bainitic steels softened by  $\sim 5\%$  and  $12\%$ , respectively. The softening was higher in BS-350 nanostructured bainitic steel. This was attributed to the interaction of hydrogen with dislocations, which enhanced dislocation mobility and hence softening. For the mild steel, the hardness was attributed to supersaturation of dissolved hydrogen that gave rise to the formation of voids and

cracks. This generated additional stress and new dislocation that enhanced hardening. The effect of hydrogen diffusion on hardness was, however, found to be limited to the subsurface region of BS-200 compared to BS-350 nanostructured bainitic steel and mild steel.

In TWIP steel, the microstructure is comprised of a single austenite phase stabilized by a high amount of manganese. TWIP steel has an excellent combination of strength and elongation which is achieved through work hardening, deformation twinning and small grains size  $\sim 5 \mu\text{m}$ . The hydrogen permeation rate in TWIP steel was about three orders of magnitude lower than the permeation rate in mild steel. Interestingly, the effective hydrogen diffusivity in TWIP steel was about two times higher compared to mild steel. The higher hydrogen diffusivity in TWIP steel compared to mild steel can be attributed to diffusion been primarily through the low energy grain boundaries of TWIP steel, as austenite grains have very low effective hydrogen diffusivity. Tensile tests were carried out in pre-charged and in-situ hydrogen charged conditions to evaluate the HIC susceptibility of the steel. The resistance to HIC based on the susceptibility indices ( $I_{HIC}$ ) for elongation ( $\mathcal{E}_l$ ) and reduction in area ( $RA$ ) showed that TWIP steel was about 60% more resistant in its pre-charged condition than mild steel. The fractured surface analysis of the pre-charged sample revealed ductile failure in TWIP steel characterized by a uniform distribution of fine dimples and micro-voids. In mild steel, the surface showed brittle fractures. However, in the in-situ condition, TWIP steel exhibited brittle failure with a mix of dimples and large cracks attributable to more cathodically evolved hydrogen available for diffusion along the grain boundaries for crack propagation. The findings from this study have been disseminated through the following publications.

## List of Candidate's Publications

- Kazum, O., Beladi, H., Timokhina, I. B., He, Y., Bobby Kannan, M. (2016). "Hydrogen permeation in nanostructured bainitic steel." *Mettal. Mater. Trans. A*, 47, 4896-4903.
- Kazum, O., Bobby Kannan, M. (2017). "Effect of cathodic hydrogen-charging current density on the hydrogen diffusivity in nanostructured bainitic steels." *Mater. Sci. Tech.*, DOI:10.1080/02670836.2017.1342944. 33, 1548-1552.
- Kazum, O., Beladi, H., Bobby Kannan, M. (2018). "Hydrogen permeation in twinning-induced plasticity (TWIP) steel." *Int. J. Hydrogen Energ.*, (Accepted).
- Kazum, O., Ionescu, M., Bobby Kannan, M. "Hydrogen depth profiling in nanostructured bainitic steel." *Int. J. Hydrogen Energ.*, (Submitted).
- Kazum, O., Beladi, H., Bobby Kannan, M., "Hydrogen-induced cracking behavior of pre-charged and in-situ charged TWIP steel." (In preparation).



# Table of Contents

|  |      |
|--|------|
| Acknowledgements .....   | ii   |
| Statement on the Contribution of Others.....                       | iii  |
| Abstract.....  | iv   |
| List of Candidate's Publications.....                              | vii  |
| Table of Contents .....  | viii |
| List of Tables.....  | xi   |
| List of Figures.....   | xii  |
| List of Plates .....   | xv   |
| List of Symbols.....   | xvi  |
| Chapter 1    Introduction .....                                    | 1    |
| 1.1    Background – Ultrahigh-Strength Steel.....                  | 1    |
| 1.2    Alloying/Solid Solution Strengthening.....                  | 1    |
| 1.3    Grain Boundary Strengthening .....                          | 2    |
| 1.4    Work Hardening .....  | 3    |
| 1.5    Bainitic Steels .....                                       | 4    |
| 1.6    TWIP Steel.....   | 4    |
| 1.7    Cathodic Protection (CP).....                               | 5    |
| 1.8    Objectives .....  | 7    |
| Chapter 2    Literature Review .....                               | 9    |
| 2.1    Hydrogen in Steel .....                                     | 9    |
| 2.2    Hydrogen Induced Cracking (HIC) .....                       | 9    |
| 2.3    Mechanism of HIC .....                                      | 10   |
| 2.3.1    The Internal Pressure Model.....                          | 10   |
| 2.3.2    Hydrogen Induced Decohesion Model .....                   | 11   |
| 2.3.3    Hydrogen Enhanced Localised Plasticity (HELP) Model ..... | 11   |
| 2.3.4    Hydrogen-Rich Phases Model .....                          | 11   |
| 2.4    Hydrogen Permeation and Diffusivity .....                   | 12   |

|   |  |    |
|---|--|----|
| 2.4.1   | Microstructural Influence .....  | 11 |
| 2.4.2   | Effect of charging condition .....   | 11 |
| 2.4.3   | Alloying Influence .....   | 11 |
| 2.5   | HIC - Tensile and Slow Strain Rate Test.....   | 16 |
| 2.6   | Hardness Test.....   | 16 |
| 2.7   | Optical Image.....   | 16 |
| Chapter 3 Materials and Experimental Procedure .....                              |  | 23 |
| 3.1   | Materials .....  | 23 |
| 3.1.1   | Composition.....   | 23 |
| 3.1.2   | Nanostructured Bainitic steel.....   | 23 |
| 3.1.3   | TWIP steel .....   | 24 |
| 3.2   | Microstructural Analysis .....   | 25 |
| 3.3   | Electrochemical Permeation Test .....  | 27 |
| 3.4   | Hydrogen Depth Profiling Analysis .....  | 29 |
| 3.4.1   | Micro hardness.....  | 30 |
| 3.4.2   | Elastic Recoil Detection Analysis (ERDA) technique.....  | 31 |
| 3.5   | Mechanical Tensile Test .....  | 32 |
| Chapter 4 Hydrogen Permeation in Nanostructured Bainitic Steel (Publication)..... |  | 35 |
| 4.1   | Introduction.....  | 35 |
| 4.1.1   | Optical microstructures.....   | 35 |
| 4.1.2   | TEM microstructures .....  | 35 |
| 4.1.3   | Effective hydrogen diffusivity .....   | 37 |
| 4.2   | Effect of Hydrogen-Charging Current Density on Hydrogen Diffusion in Nanostructured Bainitic Steels (Publication)..... | 44 |
| 4.2.1   | Effective hydrogen diffusivity .....   | 44 |
| 4.3   | Summary.....   | 50 |
| Chapter 5 Hydrogen Depth Profiling in Nanostructured Bainitic Steel.....          |  | 51 |
| 5.1   | Introduction.....  | 51 |
| 5.2   | Microhardness.....   | 51 |
| 5.3   | Cross-Section Hardness Profile .....   | 54 |
| 5.4   | Subsurface Hydrogen Concentration by ERDA Analysis .....   | 55 |

|            |  |    |
|------------|--|----|
| 5.5        | Summary.....   | 57 |
| Chapter 6  | Hydrogen Permeation in TWIP Steel .....                              | 58 |
| 6.1        | Introduction.....  | 58 |
| 6.2        | Microstructure.....  | 59 |
| 6.3        | Hydrogen Permeation Rate at Room Temperature.....                    | 60 |
| 6.3.1      | Electrolyte temperature on hydrogen permeation rate.....             | 62 |
| 6.3.2      | Multi-transient permeation curves: irreversible traps analysis ..... | 64 |
| 6.3.3      | Effective hydrogen diffusivity .....                                 | 65 |
| 6.4        | Discussion.....  | 67 |
| Chapter 7  | Hydrogen Induced Cracking (HIC) in TWIP Steel .....                  | 73 |
| 7.1        | Introduction.....  | 73 |
| 7.2        | Tensile Properties of Pre-charged Samples .....                      | 73 |
| 7.3        | Macrographs of Fractured Samples .....                               | 76 |
| 7.4        | Fractography .....   | 78 |
| 7.5        | HIC Susceptibility of Pre-charged Samples .....                      | 82 |
| 7.6        | Slow Strain Rate Testing of In-situ Charged Samples.....             | 83 |
| 7.7        | Macrographs of Fractured Samples .....                               | 87 |
| 7.8        | Fractography Analysis .....  | 90 |
| 7.9        | HIC Susceptibility .....   | 93 |
| 7.10       | Summary.....   | 94 |
| Chapter 8  | Conclusions .....  | 96 |
| References | .....  | 97 |

## List of Tables

|  |    |
|--|----|
| Table 2.1 Price and corrosion rate of common metals .....  | 12 |
| Table 2.2 Summary of literature on the susceptibility of steels to embrittlement.....  | 20 |
| Table 3.1 Chemical composition of the steels used in this study (weight percent).....  | 23 |
| Table 4.1 Hydrogen permeation data for the mild steel and nanostructured bainitic<br>steel (first transient).....  | 38 |
| Table 4.2 Hydrogen permeation data for the mild steel and nanostructured bainitic<br>steel (second transient). ....  | 40 |
| Table 4.3 Hydrogen permeation data for mild steel, BS-200 and BS-350<br>nanostructured bainitic steels. ....   | 46 |
| Table 6.1 Hydrogen permeation parameters of the mild steel and TWIP steel<br>cathodically charged (10 mA/cm <sup>2</sup> ) at 25 °C. ....                              | 61 |
| Table 6.2 Permeation parameters of the mild steel and TWIP steel cathodically<br>charged (10 mA/cm <sup>2</sup> ) at different temperatures. ....                      | 63 |
| Table 6.3 Permeation current density from the multi-transient curves for the mild<br>steel and TWIP steel cathodically charged (10 mA/cm <sup>2</sup> ) at 30 °C. .... | 65 |
| Table 6.4 Effective hydrogen diffusivity and breakdown time for the mild steel<br>and TWIP steel cathodically charged at different temperatures. ....                  | 66 |
| Table 7.1 The I <sub>HE</sub> susceptibility indices for mild steel and TWIP steel .....   | 82 |
| Table 7.2 The <i>I<sub>HE</sub></i> susceptibility indices for mild steel and TWIP steel .....   | 93 |

## List of Figures

|  |    |
|--|----|
| Figure 1.1 Schematic illustrating strained lattice by the addition of substitutional and interstitial solute. ....   | 2  |
| Figure 1.2 Schematic illustrating the concept of dislocation pile up and its effect on the strength of the material. ....  | 3  |
| Figure 1.3 Cathodic protection using sacrificial anode. ....   | 6  |
| Figure 1.4 Cathodic protection using impressed current. ....   | 6  |
| Figure 2.1 Typical hydrogen permeation curve. ....   | 15 |
| Figure 2.2 Typical stress strain curve. ....   | 17 |
| Figure 3.1 Heat treatment process for nanostructured bainitic steel. ....  | 24 |
| Figure 3.2 Heat treatment process for TWIP steel. ....   | 25 |
| Figure 3.3 Schematic diagram of Devanathan-Stachurski permeation cell set-up. ....   | 27 |
| Figure 3.4 The geometry of tensile specimen used for mechanical tests. ....  | 32 |
| Figure 3.5 Experimental set up of in-situ charged sample. ....   | 33 |
| Figure 4.1 Hydrogen permeation curves for the nanostructured bainitic steel and mild steel. ....   | 37 |
| Figure 4.2 Hydrogen permeation curves for the steels showing double transient curves. ....   | 39 |
| Figure 4.3 Overlay of the double transient curves for the steels (Note: $T_a$ is the first transient and $T_b$ is the second transient). ....  | 39 |
| Figure 4.4 Hydrogen permeation curves for the mild steels showing multiple transient curves. ....  | 41 |
| Figure 4.5 Schematic model illustrating interaction between hydrogen and the different microstructure of (a) mild steel, (b) BS-200, and (c) BS-350. (Note: not drawn to scale). ....        | 42 |
| Figure 4.6 Hydrogen permeation curves for mild steel, BS-200 and BS-350 nanostructured bainitic steels, cathodically hydrogen-charged at different hydrogen-charging current densities. .... | 45 |

|   |    |
|---|----|
| Figure 4.7 Normalised percentage increase of the hydrogen diffusivity in mild steel, BS-200 and BS-350 nanostructured bainitic steels, normalised against hydrogen diffusion at 10 mA/cm <sup>2</sup> ..... | 48 |
| Figure 5.1 Vickers surface hardness of the steels.....  | 53 |
| Figure 5.2 Micro-hardness values for uncharged and H-charged steels taken laterally.....  | 55 |
| Figure 5.3 (a) Hydrogen depth profile and (b) hydrogen concentration in at% for the mild steel. ....  | 56 |
| Figure 6.1 Hydrogen permeation curves for the mild steel and TWIP steel cathodically charged (10 mA/cm <sup>2</sup> ) at room temperature; i.e. (25 °C). ....   | 60 |
| Figure 6.2 Hydrogen permeation curves and peak permeation current for: (a) mild steel, and (b) TWIP steel cathodically charged (10 mA/cm <sup>2</sup> ) at different temperatures. ....                     | 62 |
| Figure 6.3 Multiple transients of hydrogen permeation curves for the mild steel and TWIP steel cathodically charged (10 mA/cm <sup>2</sup> ) at 30 °C.....  | 65 |
| Figure 6.4 Hydrogen permeation rate of the mild steel and TWIP steel cathodically charged (10 mA/cm <sup>2</sup> ) at different temperatures. ....  | 67 |
| Figure 6.5 Arrhenius plot of the effective hydrogen diffusivity of mild steel compared with the literature values. ....   | 69 |
| Figure 6.6 Schematic diagram illustrating hydrogen permeation in mild steel and TWIP steel.....   | 71 |
| Figure 7.1 Stress-strain plots of mild steel samples in uncharged and H-charged conditions. ....  | 74 |
| Figure 7.2 % elongation of mild steel samples plotted in bar charts.....  | 74 |
| Figure 7.3 Stress-strain plots of TWIP steel samples in uncharged and H-charged conditions. ....  | 75 |
| Figure 7.4 Elongation of TWIP steel samples plotted in bar charts.....  | 76 |
| Figure 7.5 % reduction in area ( <i>RA</i> ) of the samples plotted in bar charts.....  | 78 |

|   |    |
|---|----|
| Figure 7.6 The $I_{HE}$ susceptibility indices (a) elongation and (b) reduction in area<br>for mild steel and TWIP steel plotted in bar charts.....   | 83 |
| Figure 7.7 Stress-strain plots of mild steel samples in: (a) pre-charged and (b) in-<br>situ charged conditions. ....                                 | 84 |
| Figure 7.8 Ultimate tensile strength of the mild steel samples plotted in bar charts.....   | 84 |
| Figure 7.9 % elongation ( $\mathcal{E}_f$ ) of mild steel samples plotted in bar charts. ....   | 85 |
| Figure 7.10 Stress-strain plots of TWIP steel samples in: (a) pre-charged and (b)<br>in-situ charged conditions. ....                                 | 86 |
| Figure 7.11 Ultimate tensile strength of the TWIP steel samples plotted in bar<br>charts. ....  | 86 |
| Figure 7.12 % elongation ( $\mathcal{E}_f$ ) of TWIP steel samples plotted in bar charts.....   | 87 |
| Figure 7.13 % reduction in area ( $RA$ ) of mild steel samples plotted in bar charts. ....  | 89 |
| Figure 7.14 % reduction in area ( $RA$ ) of TWIP steel samples plotted in bar charts.....   | 89 |
| Figure 7.15 The $I_{HIC}$ susceptibility indices (a) elongation and (b) reduction in area<br>for mild steel and TWIP steel plotted in bar charts..... | 93 |

## List of Plates

|  |    |
|--|----|
| Plate 4.1 Optical micrographs of: (a) BS-200 nanostructured bainitic steel, (b) BS-350 nanostructured bainitic steel and (c) mild steel.....   | 36 |
| Plate 4.2 TEM micrographs of nanostructured bainitic steel: (a) BS-200 and (b) BS-350 (c) TEM micrograph showing dislocation in white arrows.<br>(Note: RA is retained austenite and BF is bainitic ferrite). .... | 36 |
| Plate 5.1 Images of microhardness indent of the steels surface in uncharged and H-charged conditions of mild steel, BS-200 steel and BS3-50 steel. ....  | 52 |
| Plate 6.1 (a) Optical micrograph of mild steel, and (b) EBSD micrograph of TWIP steel.....   | 59 |
| Plate 7.1 Macrographs of the fractured tensile specimens uncharged (a, b), H-charged 25° C (c, d), H-charged 30° C (e, f) and H-charged 50° C (g, h). ....   | 77 |
| Plate 7.2 Fractured surfaces of mild steel showing the edge, full and centre section: uncharged, H-charged 25 °C, H-charged 30 °C and H-charged 50 °C.....   | 79 |
| Plate 7.3 Fractured surfaces of TWIP steel showing the edge, full and centre section: uncharged, H-charged 25 °C, H-charged 30 °C and H-charged 50 °C.....   | 80 |
| Plate 7.4 Macrographs of the fractured tensile specimen of uncharged and charged steels at the strain rates $2 \times 10^{-4}$ /s (a, b) and $5 \times 10^{-6}$ /s (c, d). ....                                    | 88 |
| Plate 7.5 Fractured surfaces showing centre section of uncharged and charged steels at the strain rates $2 \times 10^{-4}$ /s (a, b) and $5 \times 10^{-6}$ /s (c, d).....   | 91 |



## List of Symbols

| <i>Symbols</i>     |   | Description                                       |
|--------------------|---|---|
| $^{\circ}\text{C}$ | = | Degree Celsius                                    |
| <i>BS-200</i>      | = | Bainitic steel produced at 200 $^{\circ}\text{C}$ |
| <i>BS-350</i>      | = | Bainitic steel produced at 350 $^{\circ}\text{C}$ |
| <i>TWIP</i>        | = | Twinning-induced plasticity steel                 |
| <i>Pct</i>         | = | Percent   |
| <i>SCC</i>         | = | Stress corrosion cracking                         |
| <i>HIC</i>         | = | Hydrogen induced cracking                         |
| <i>HE</i>          | = | Hydrogen embrittlement                            |
| $I_{\text{HIC}}$   | = | Susceptibility index for HIC                      |
| <i>ERDA</i>        | = | Electrical Recoil                                 |
| <i>CP</i>          | = | Cathodic protection                               |
| <i>DS</i>          | = | Devanathan-Stachurski                             |
| <i>DC</i>          | = | Direct current                                    |
| <i>RA</i>          | = | Retained austenite                                |
| <i>BF</i>          | = | Bainitic ferrite                                  |
| <i>F</i>           | = | Faraday constant (96485 coulomb/mole)             |
| $T_a$              | = | First transient                                   |
| $T_b$              | = | Second transient                                  |
| <i>at%</i>         | = | Atomic weight percentage                          |
| <i>TEM</i>         | = | Transmission electron microscope                  |
| <i>SiC</i>         | = | Silicon-carbide                                   |
| <i>SEM</i>         | = | Scanning electron microscope                      |

|                 |   |  |
|-----------------|---|--|
| $Rpm$           | = | Revolution per minute                    |
| $HSR$           | = | High strain rate                         |
| $LSR$           | = | Low/slow strain rate                     |
| $UTS$           | = | Ultimate tensile stress                  |
| $\mathcal{E}_f$ | = | Elongation                               |
| $RA$            | = | Reduction in area                        |
| $S$             | = | Second                                   |
| $H$             | = | hour                                     |
| $EBSD$          | = | Electron back scattering diffraction     |
| $EDM$           | = | Electrical discharge machining           |
| $I_p$           | = | Steady/Peak current density              |
| $t_b$           | = | Breakthrough time                        |
| $J$             | = | Hydrogen permeation flux                 |
| $Q$             | = | Hydrogen permeation rate                 |
| $D$             | = | Effective hydrogen diffusivity           |
| $A$             | = | Dislocation density                      |
| $N_X$           | = | Number of intersections with dislocation |
| $Xt$            | = | Radom line length of thickness $t$       |
| $BCC$           | = | Body cubic centre                        |
| $FCC$           | = | Face cubic centre                        |

---

# **Chapter 1      Introduction**

## **1.1 Background – Ultrahigh-Strength Steel**

Steels are generally in high demand for engineering application in the automobile, chemical, oil and gas industries due to their mechanical and corrosion resistance properties. For certain structural installations, mechanical properties such as yield strength, tensile strength and ductility often play a more major role in material selection compared to corrosion resistance properties. This is due to steel being generally susceptible to some degree of corrosion, which can be reduced further by using a combination of corrosion protection methods. Hence, the strength of steel is often a paramount concern in the construction of structural components. The enhancement of mechanical properties requires prohibiting the mobility of large number of dislocations, which cause plastic deformation. The trapping of high density of dislocation helps slows down plastic deformation and therefore enhances the material strength. This improvement in mechanical properties is advantageous due to increased strength to weight ratio, the improvement of safety standards, and the reduction in installation and construction costs. Ultrahigh-strength steels are thus preferable to low strength steel in modern construction where strength is critical. A number of techniques can be used to improve the strength of steel: alloying, grain boundary strengthening and work hardening.

## **1.2 Alloying/Solid Solution Strengthening**

Alloying elements form either substitutional or interstitial solute atoms in the parent material and cause lattice defects in the crystal structure. The lattice distortion impedes dislocation motion and hence increases the yield stress of the material. These solute atoms of the alloying element also impact either compressive or tensile stresses to the

lattice and, depending on the size of the solute, act as potential barriers to dislocation propagation (Figure 1.1).

An increase in the concentration of the solute atoms will increase the yield strength of the material to an optimum level. The solid solution strengthening is also dependent on shear modulus of solute atoms, size, valency of solute atoms and solute stress field. Common alloying elements such as carbon C and chromium Cr are used in steel to enhance its mechanical properties.

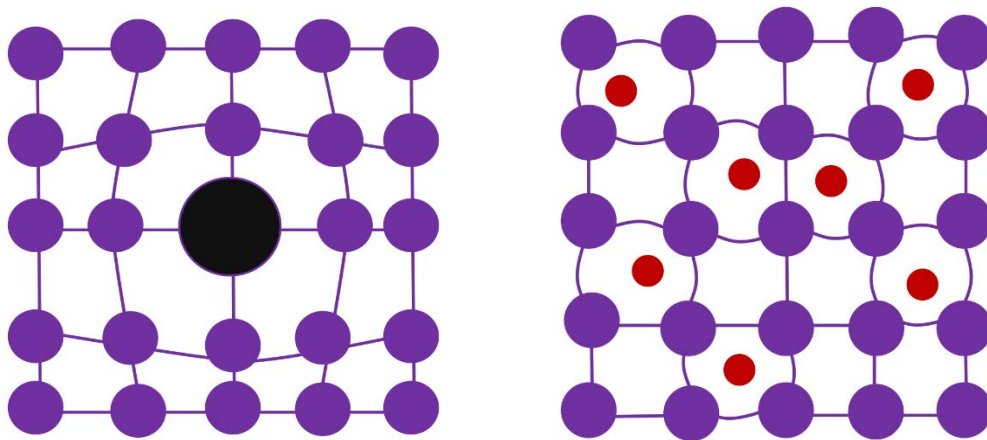


**Figure 1.1** Schematic illustrating strained lattice by the addition of substitutional and interstitial solute.

### **1.3 Grain Boundary Strengthening**

The grain size of polycrystalline metal has a major effect on the strength of metallic materials. Given that the crystallographic orientation of each grain differs, grain boundaries arise which act as impediments to dislocation motion. It is generally known that the stress required to move a dislocation from one grain to another to cause plastic deformation is dependent on grain size. As the average dislocation density per grain decreases with average grain size, it can be anticipated that a lower dislocation pile up will be seen at the grain boundaries. Therefore, more force is required to move the dislocation into adjacent small grains (Figure 1.2). Essentially smaller grain size

enhances the tensile properties of the material, but the relationship has an optimizing effect, as the continuous reduction of grain size leads to sliding instead; a phenomenon known as grain-boundary sliding. In general, heat treatment methods have been shown to be effective for grain refinement and hence the enhancement of mechanical properties of steel materials (Timokhina et al. 2011).

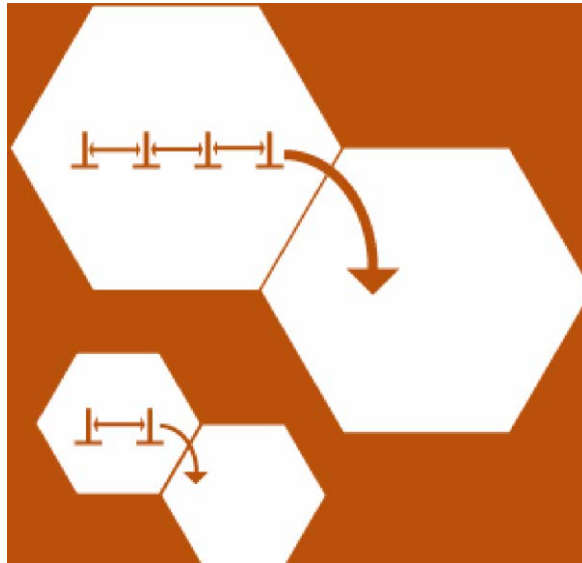


**Figure 1.2 Schematic illustrating the concept of dislocation pile up and its effect on the strength of the material.**

## **1.4 Work Hardening**

Dislocations are responsible for work hardening when they interact with each other by generating stress fields in the material. The stress field can impede dislocation motion. Additionally, the entanglement of high dislocations causes formation of jog that acts as pinning points, which further inhibits dislocation motion. Work hardening can typically be achieved by forging, rolling, drawing or extrusion, and reports suggest that a moderate dislocation density value, in the range of  $10^7$ - $10^9$  dislocation/ $m^2$ , is exhibited by material with low mechanical strength. At a dislocation density of  $10^{14}$  dislocation/ $m^2$  or higher, the strength of the material increases to an optimal level, beyond which point the material

can lose its crystalline structure. Therefore, work hardening can improve the mechanical properties of steels (Kusakin et al. 2014).

In recent years, the use of these strengthening techniques has led to the development of new categories of ultrahigh-strength steels: High strength bainitic steel and TWIP steel. They are formed by the processes of grain refinement and deformation respectively. The steels can exhibit strength ( $> 900$  MPa) and high elongation (30-60%). The high strength to weight ratio makes them suitable for application in oil and gas structures, where strength is critical to prevent the collapse of oilrig structures.

## **1.5 Bainitic Steels**

Bainitic steels are formed by the grain refinement technique using low temperature transformation. Relatively low temperatures of 150-350 °C (Beladi et al. 2009; Timokhina et al. 2011) are used in bainite formation. In general, the microstructure is comprised of aggregated bainitic ferrite and carbon rich retained austenite layers. This structure is created when a high carbon, silicon steel is transformed into bainite. The carbon that is partitioned into residual austenite does not precipitate into cementite, making it stable at ambient temperature. The strength ( $\sim 2.3$  GPa) of this material is derived from the fine grain size of the ferrite plate and retained austenite, which range from 20 to 300 nm in thickness depending on the isothermal holding temperature (Garcia-Mateo et al. 2003; Caballero et al. 2007; Caballero and Bhadeshia 2004; Peet et al. 2004). The mean free slip distance is thus shortened, and the strength of the material is enhanced.

## **1.6 TWIP Steel**

The TWIP steel is a high manganese (Mn) single-phase austenite steel, which makes the steel stable at ambient temperature. It is formed by continuous casting and hot rolling of the material into thick plates after reheating to  $\sim 1000$  °C. This is followed by air-cooling

to room temperature and cold rolling again to achieve thinner plates (Park et al. 2012; Kusakin et al. 2014). The steel achieves its superior tensile properties (over 800 MPa, ductility 50%) from the deformation twinning (Yang et al. 2013; Bouaziz and Guelton 2001). This twinning acts as subsidiary grain boundaries to pin down dislocation and hence improve strength.

Corrosion has been a major issue in the steel industries. Steels can become susceptible to different forms of corrosion depending on various factors, such as the type and phases present in the steel, the steel's alloying content, the nature of corrosive environment, levels of temperature, humidity and the steel's nearness to ocean. Generally, steel in the oil and gas industries can be susceptible to uniform, localized or stress corrosion cracking. While a combination of different corrosion protection methods can be adopted (coating, alloying and cathodic protection (CP) to mitigate corrosion, a more common problem is the hydrogen-induced cracking (HIC) which can develop during cathodic protection (CP).

## **1.7 Cathodic Protection (CP)**

CP is an effective technique used to control the corrosion of metal by making the material to be protected cathodic in an electrochemical cell. It is commonly employed for corrosion prevention in storage tanks, pipeline and marine structures. CP can be accomplished by two methods:

**Sacrificial Anode:** This method involves coupling the structure to be protected for example, pipeline steel, with a more active metal such as zinc or magnesium, in order to form a galvanic cell. The active metal becomes the anode, which provides a flow of electrons to the pipeline steel or the cathode. The cathode is thus protected while the anode progressively corrodes; hence its name: the sacrificial anode (Figure 1.3).

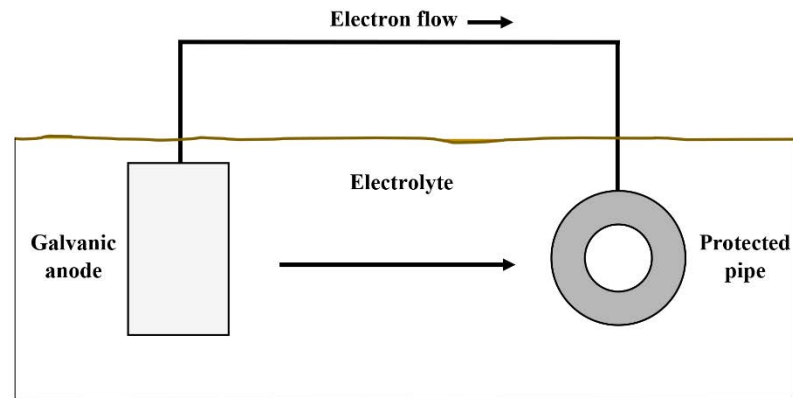


**Figure 1.3 Cathodic protection using sacrificial anode.**

**Impressed Current:** This method is gaining popularity, especially in those situations where electricity is plentiful and the volume of steel to be protected is large. The method involves impressing a direct current between an inert anode and the structure to be protected. The structure is thus protected, since electrons flow into the cathode (Figure 1.4).

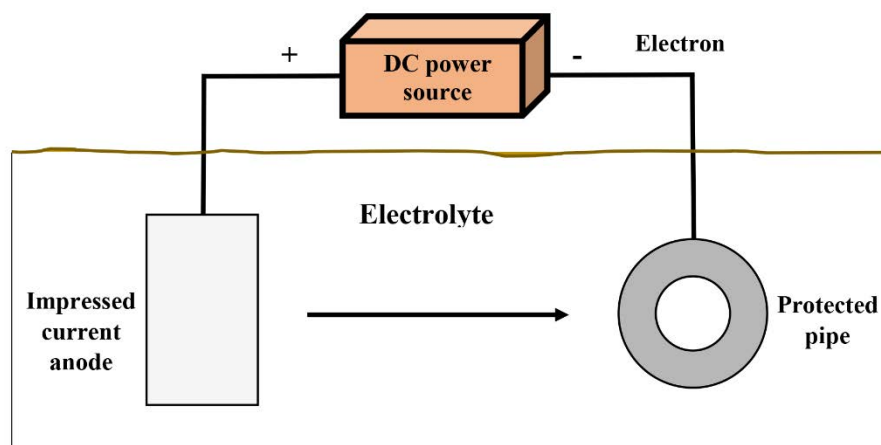


**Figure 1.4 Cathodic protection using impressed current.**

CP is effective against stress corrosion cracking (SCC), however while SCC is reduced the formation of hydrogen during cathodic charging can result into a different localised



form of corrosion known as hydrogen induced cracking (HIC) or hydrogen embrittlement (HE).

It is known that ultrahigh-strength steel has an advantage over low strength steel due to the potential reduction in welding and other construction costs from the reduction in the quantity of materials required. Although the corrosion protection of steels in the oil and gas industries by CP impressed current method may be effective, the absorption of hydrogen from seawater that is promoted when CP is applied to steel is of great concern. High strength steels are known to be more prone to HIC (Hilditch et al. 2003; Depover et al. 2014), but austenitic steels are less prone to HIC compared to ferritic steel, due to the low hydrogen diffusivity in austenite (Kim et al. 2008). Recent reports have indicated some uncertainty over the susceptibility of high strength austenitic steel to HIC (So et al. 2009; Chin et al. 2011; Koyama et al. 2012; Kim et al. 2008), given that the nanostructured bainitic steel and TWIP steel have varying contents of austenitic phase, and are also high strength due to their refined microstructural features such grain size and dislocation density. The distribution of these features within the microstructure of the steel can influence the mobility of hydrogen generated during CP and influence their HIC behaviour. Hence, it is critical to understand the HIC susceptibility of the steels to finally determine their suitability for use in the oil and gas sector.

## **1.8 Objectives**

The main research objectives of this study are therefore:

- To understand the role of the microstructure on the hydrogen permeation in nanostructured bainitic steel.
- To evaluate the effect of increased hydrogen generated by charging current density on the hydrogen diffusivity of nanostructured bainitic steel.

- Understand the role of hydrogen on the mechanical property at different depth of nanostructured bainitic steel.
- To understand the hydrogen diffusion behaviour in austenite TWIP steel in comparison to ferritic mild steel.
- To identify the effect of hydrogen concentration and hydrogen diffusivity on the mechanical properties of TWIP steel in different charging conditions.

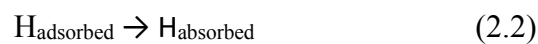
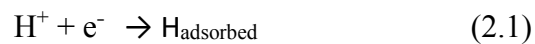
## Chapter 2 Literature Review

### 2.1 Hydrogen in Steel

The presence and interaction of hydrogen with steel can result into the loss of ductility and hence the tensile property of steel. Hydrogen can interact and diffuse into the bulk of steel from a number of processes such as:

- Pickling in mineral acids;
- Electroplating;
- Welding;
- Exposure to H<sub>2</sub>S sour environment; and
- Cathodic protection.

Generally, hydrogen in its atomic form can diffuse through the grain boundaries or crystal lattice and concentrations as low as a few parts per million can lead to catastrophic failure such as HIC (Dean 2005; Brass et al. 1994), hydrogen blistering, cracking from hydride formation, hydrogen attack and cracking from the precipitation of internal hydrogen (Dean 2005; Elhoud et al. 2010; Perng and Altstetter 1987). HIC is more common in the oil and gas industries. Adsorption followed by absorption of hydrogen atoms through the chemical reactions in equations 2.1 and 2.2 to stress-concentrated regions of the material (e.g., crack sites or voids) would reduce the mechanical properties of the bulk material.



### 2.2 Hydrogen Induced Cracking (HIC)

Hydrogen induced cracking (HIC) occurs as a result of the diffusion and interaction of nascent hydrogen with the steel microstructure when the material is under some form of

loading. While the microstructure, including such elements as grain size, grain boundaries, dislocation density, inclusions and precipitate (Haq et al. 2013; Robertson et al. 1980) play a vital role in HIC susceptibility, it is generally known that susceptibility increases with the increase in the strength of material (Loidl and Kolk 2011; Hilditch et al. 2003; Depover et al. 2014) and the amount of body-centred cubic (BCC) crystal structure present in the steel. Depending on the size, these features can either facilitate hydrogen diffusion or trap hydrogen reversibility/irreversibility and reduce diffusivity (Kimura and Birnbaum 1988; Chou and Tsai 1999; Szost et al. 2013).

The steels under investigation in this study exhibit varying microstructures: from BCC, face-centred cubic (FCC) to a mixture of both. Since they have interesting microstructures as a result of strength enhancement, it is necessary to study their HIC behaviour in susceptible environments.

## **2.3 Mechanism of HIC**

There are a number of mechanisms proposed to explain the effect of hydrogen interaction with metals. These are:

- The Internal Pressure model;
- The Hydrogen Induced Decohesion model;
- The Hydrogen Enhanced Localised Plasticity (HELP) model and
- The Hydrogen Rich Phases model.

### **2.3.1 *The Internal Pressure Model***

This model attributes HIC to the internal pressure developed during precipitation of molecular hydrogen at the sites of internal defects such as in voids or around non-metallic inclusions. The internal pressure enhances void and crack propagation, which, in addition

to externally applied stresses, lowers the apparent fracture stress (Zappfe and Sims 1941 et. al).

### **2.3.2     *Hydrogen Induced Decohesion Model***

Dissolved lattice hydrogen is proposed to cause a reduction in the cohesive strength of the interatomic bonds, and thus promotes decohesion. Observation of the fractography along the transgranular fractures are often quasi-cleavage in nature in this model.

### **2.3.3     *Hydrogen Enhanced Localised Plasticity (HELP) Model***

The absorption of hydrogen and its solid solution is thought to increase the ease of dislocation motion or its generation, especially at crack tips. It is a localised deformation that leads to highly localised failure by ductile processes, while the bulk of the material can experience small deformations. The presence of hydrogen in solid solution decreases the barriers to dislocation motion, thereby increasing the amount of deformation that occurs in a localised region adjacent to the fracture's surface.

### **2.3.4     *Hydrogen-Rich Phases Model***

Hydrogen-rich phases such as those that can form hydrides from zirconium, titanium, tantalum and rare earth metals have mechanical properties that are different from those of the matrix. The model proposes that cracks could develop along the brittle hydride and progress to failure. Interestingly, the steel used in this study had no hydride-forming metals in their composition.

Usually, a single model or a combination of the models can explain the HIC behaviour of a steel sample. In general, the HIC susceptibility of a material can be evaluated by electrochemical and mechanical tests.

## 2.4 Hydrogen Permeation and Diffusivity

Mild steel, carbon steel, and low-alloy steel are the commonly used material for transportation and storage in the oil and gas industry due to relative cost in comparison to austenite stainless steel (Kappes et al. 2014; Worldsteel 2018), copper, nickel (Dailymetal 2018) and titanium (Agmetalmminer 2018) materials. Table 2.1 demonstrates that carbon steel exhibit a higher corrosion rate (CR) in sulphuric acid ( $\text{H}_2\text{SO}_4$ ) environment than austenite stainless steel (UNS 304) (API 2008) however, CP can mitigate corrosion. Hence, the cost steel rather than the corrosion rate of steel is a primary factor in material selection in this industry. For carbon steel, the price is significantly lower by ~72% compared with austenite steel (Worldsteel 2018), and so it is preferred by most industries. The cost of maintaining the integrity of carbon steel for its lifetime may, however, be high in the end hence, cheaper form of austenitic steel such as nanostructured bainitic and TWIP steels are being researched.

**Table 2.1** Price and corrosion rate of common metals.

| Materials                     | Price /tonne (US (\$)) | CR in 93 % $\text{H}_2\text{SO}_4$ (mmy <sup>-1</sup> ) |
|-------------------------------|------------------------|---|
| Carbon steel                  | 783                    | 1.91  |
| Austenite stainless (UNS 304) | 2780                   | 1.52  |
| Copper                        | 5709                   | -   |
| Nickel                        | 11470                  | -   |
| Titanium                      | 18500                  | -   |

CP generate hydrogen around the material that is protected, and a poorly managed CP system may result in evolution and ingress of a high amount of hydrogen to the steel microstructure which can cause HIC failure. HIC failures are detrimental, and the cost associated with repairs or replacement could be huge. Research into the new material is

ongoing, and it is therefore critical to identify metallic material that is less susceptible to HIC for possible application in this industry. In general, HIC susceptibility of a metallic material can be predicted from its effective hydrogen diffusivity (Escobar et al. 2011). This chapter, therefore, provides an overview of literature relevant to the prediction and determination of HIC susceptibility, and how it can be useful for this work.

#### ***2.4.1 Microstructural Influence***

The general opinion is that high strength steels are more susceptible to HIC (Park et al. 2002). However, the microstructure is now known to play a vital role in hydrogen diffusivity and hence the structural integrity of metallic materials (Depover et al. 2014; Hirth 1980). It is generally acknowledged that steel containing ferrite microstructure experience high diffusivity and hence HIC compared to one with austenitic structure (Chou et al. 1999). Luu et al. 2002 and Chen et al. 2004 studied a duplex stainless steel and reported that more hydrogen distribution was observed in the ferrite phase using hydrogen microprint technique. Reports suggest that lattice diffusion is predominant in the ferrite (Chen et al. 2004, Ichitani et al. 2003). Ferrite microstructure has a low activation energy of hydrogen diffusion and hence are more susceptible to HIC compared with austenitic structure (Chou et al. 1999; Chen et al. 2004). Also, hydrogen diffusion through the grain boundaries is higher than through the grain lattice (Haq et al. 2013), and in some cases, the grain boundaries may facilitate hydrogen diffusion or trap the same at nodes and juncture to reduce hydrogen diffusivity (Kimura and Birnbaum 1988). Literature suggests that hydrogen diffusivity is enhanced by coarser grains (Hag et al. 2013; Bai et al. 2016; Park et al. 2015) and hence HIC due to local accumulation of hydrogen. The microstructural refinement of the steel features such as grain size, grain boundary, twinning, dislocation density, precipitates, interface and the phases of steel

present are features that can influence hydrogen diffusivity (Haq et al. 2013; Turnbull et al. 1989).

#### ***2.4.2 Effect of Charging Condition***

Time (Akiyama et al. 2011), temperature (Addachi et al. 2005; Zheng et al. 2013) and charging current density (Li et al. 2013; Dong et al. 2009) have also shown to increase diffusible hydrogen content on ferritic and austenitic steel. Also, the pH condition of the electrolyte is known to affect the rate at which hydrogen is evolved. For steels charged under a similar electrochemical condition, less hydrogen concentration and hydrogen damage were found in the alkaline electrolyte when compared to an acidic environment (Escobar et al. 2011). To reduce permeation and hydrogen diffusivity, zinc coating on mild steel showed an impressive result at low current density. However, at high current density there was a breakdown of the coating layer (Boiadjieva et al. 2013). In general, austenitic steel is a more suitable material considering its lower hydrogen diffusion when compared with ferritic steel. However, certain metastable austenitic steel (which transform to martensite when exposed to tensile load) can be embrittled in the presence of hydrogen.

#### ***2.4.3 Alloying Influence***

Addition of alloying elements such as Ni and Al to steel has received some interest, but the cost Ni addition has been a drawback. Al addition has however been suggested to enhance HIC by retarding brittle failure in steel. More recently, austenite is stabilized by a high amount of manganese to form stable austenite such as TWIP steel (Koyama et al. 2012). These steels have been reported to show different HIC report, with some showing significant HIC (Koyama et al. 2014) and others are exhibiting marginal HIC (Ronevich et al. 2012; So et al. 2009). While austenite reduces hydrogen diffusion by trapping hydrogen when compared to ferrite, it is still unclear if microstructure containing higher



hydrogen trap sites are effective at reducing HIC due to less amount of diffusible hydrogen available to propagate cracks or the higher the hydrogen concentration due to efficient trapping is an indicator of higher vulnerability of steel to HIC. It therefore essential to first evaluate the hydrogen permeation behaviour of this new steel to determine its suitability as an engineering material.

Electrochemical hydrogen permeation test was carried out using a two-cell Devanathan-Stachurski (DS) cell setup. The sample to be tested is sandwich between the two cells and cathodically charged from one side in an electrolyte. The anodic side is polarised to determine the rate at which hydrogen is diffused through the sandwich membrane. The result is plotted as a curve of hydrogen permeation current density against time. Figure 2.1 is a typical hydrogen permeation curve, from which the effective diffusivity can be estimated using Fick's law of diffusion.

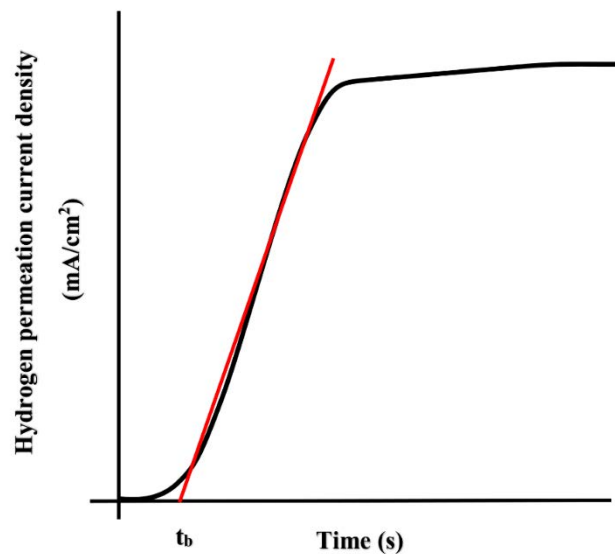


**Figure 2.1 Typical hydrogen permeation curve.**

The hydrogen permeation flux  $J$  ( $\text{mol}/\text{cm}^2 \text{ s}$ ) is calculated from the steady state permeation current density  $I_p$  ( $\text{A}/\text{cm}^2$ ) using the following relationship (Turnbull A. 1994):

$$J = DC_o/L = I_p/nF \quad (2.3)$$

where D (cm<sup>2</sup>/s) is the lattice diffusion coefficient, C (mole/cm<sup>3</sup>) is hydrogen concentration and L (cm) is sample thickness) n is the number of electrons transferred and F is Faraday's constant.

It is understood that the rate of diffusion will suggest the rate at which hydrogen travels to crack tips, voids or traps, which in turn ultimately causes failure of the material.

The rate of hydrogen diffusion differs for each material, and hence the susceptibility to HIC is influenced by microstructure features such as grain size, grain boundary, precipitates, dislocation density, inclusion, interface and the phases present in the steel. In addition, the susceptibility of a material to HIC through diffusivity is affected by temperature and charging current density, due to increase mobility or an increase in available hydrogen for diffusion (Cwiek 2010).

## **2.5 HIC - Tensile and Slow Strain Rate Test**

The results from electrochemical hydrogen permeation tests are useful for determining the hydrogen permeation rate, effective hydrogen diffusivity and hydrogen solubility in the material. To predict the HIC susceptibility of the material, further tests are required to determine changes in the mechanical property of the hydrogen charged in comparison with hydrogen uncharged conditions. The mechanical properties of material such as its ductility, strength, hardness and toughness can often be tested using a tensile test, slow strain test, hardness test, impact test and fatigue test procedures. However, the tensile test and the slow strain test methods are the commonly used test methods to determine material susceptibility to HIC. Tests are carried out on standard dog shaped samples (according to ASTM) charged with hydrogen, in a condition similar to a simulated service environment. The results of the mechanical tests are then compared to those of uncharged samples.

Test results can be presented as stress-strain curves for elongation and tensile strength analysis as shown in the typical plot Figure 2.2. A brittle failure exhibited a low elongation compared to a ductile failure. The susceptibility of the material to HIC is calculated using the susceptibility index (Kannan et al. 2006), based on % elongation or reduction in area of the sample.

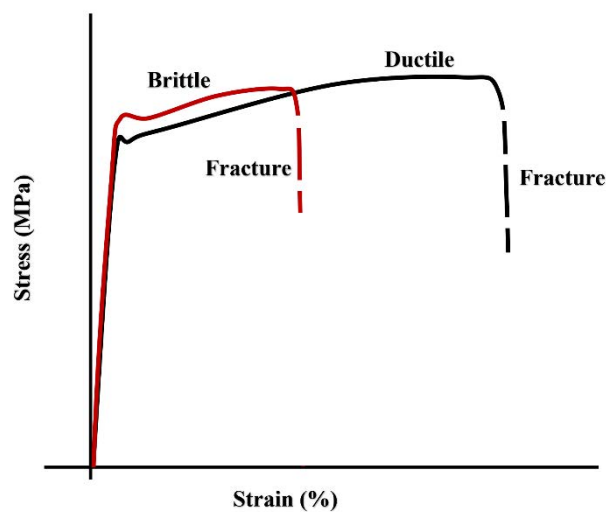


**Figure 2.2 Typical stress strain curve.**

In carbon steel (Siddiqui et al. 2005), API grade steel (Arafin et al. 2011), duplex steel (Elhoud et al. 2010; Chen et al. 2004; Luu et al. 2002) and TRIP steel (Depover et al. 2014) significant degree of HIC has been reported. Austenitic steel does not generally suffer HIC due to low diffusivity and high solubility of hydrogen in FCC crystal structures (Park et al. 2015; Kim et al. 2011; Park et al. 2012; So et al. 2009), however (Koyama et al. 2012; Koyama et al. 2014) have reported HIC in certain TWIP steel. Other reports suggest a contrary opinion with TWIP unaffected by hydrogen (Ronevich et al. 2012; Han et al. 2014). Literature reporting HIC of TWIP steel was shown to exhibit a mixture of brittle and ductile failure of the fractured surface. This suggests that hydrogen

was able to concentrate at some vulnerable site by diffusing faster through the steel microstructure other than through the austenite matrix since diffusivity is low in austenite. The literature on TWIP steel hydrogen susceptibility could be categorised into two groups. The first group that showed no significant HIC were found to be tested under the pre-charged condition and the other group showing significant HIC were tested under in-situ charging condition. It is still not very clear if mobile hydrogen (Chang et al. 2001) or soluble hydrogen (Park et al. 2008; Huang et al. 2010) is responsible for HIC. If hydrogen diffusion is low but its solubility is high in austenite, one should expect HIC due to the higher concentration of hydrogen; on the other hand, if hydrogen diffusion is high, more hydrogen is available to participate in propagating cracks. Hence, a more detailed study is required to determine the steel hydrogen diffusivity, concentration and possible HIC behaviour when hydrogen becomes soluble in pre-charged condition or hydrogen is freely mobile in (in-situ) conditions.

## ***2.6 Hardness Test***

The ingress of hydrogen influences the mechanical property. The hardness test is a cheaper means of evaluating a change in this property between an uncharged and charged small-sized samples. This method has been used for material such as Mg alloy (Kannan et al. 2007), carbon steel (Siddiqui et al. 2005) and austenitic steel (Kim et al. 2012; Han et al. 2014 Kirchheim 2012; Barnoush et al. 2012). Reports have shown that certain materials exhibit hardening while others may experience softening in the presence of hydrogen and hence, results from this test are only valuable when similar materials are compared. Kim et al. 2012 reported softening in austenitic steel charged with hydrogen while hardening is reported for materials such as carbon steel (Siddiqui and Abdullah 2005; Asano and Otsuka 1976). It is reported in the literature that a large concentration of dissolved hydrogen in the lattices of iron reduces plasticity (Siddiqui and Abdullah

2005; Asano and Otsuka 1976) and supersaturation can lead to the formation of blisters, voids, and cracks, which generate stress, and new dislocation that enhances hardening. On the other hand, the interaction of a small amount of hydrogen with dislocation can enhance dislocation mobility and hence softening (Kirchheim 2012; Barnoush et al. 2012).

## ***2.7 Optical and Image***

Optical and fracture surface analyses are often carried out to determine the fracture mode of the material. The fractured surfaces could present a brittle, ductile failure or a mix of each mode of failure. Ductile fracture is revealed by a relatively uniform distribution of spherical dimple features and micro-voids, which is a well-known characteristic of ductile fracture (Zan et al. 2015). This type of failure is seen on hydrogen uncharged samples and samples which is not susceptible to HIC (Han et al. 2014). For a brittle failure and material susceptible to HIC, it is revealed by transgranular cracking characterised by cleavage steps, river patterns and feather markings typical of HIC. It is also possible for a material to experience a mixed mode fracture exhibited by both ductile fracture zone and intergranular features, which are prior sites where hydrogen became trapped along the grain boundaries (Zan et al. 2015; Koyama et al. 2014). The brittle failure and the ductile failure can be localised to a depth of regions affected by hydrogen and region unaffected in the material respectively.

A summary of the literature on the susceptibility of steel to embrittlement is presented in Table 2.2. The reports suggest that the ferrite phase is more prone to HIC than the austenite phase, and the microstructure contributes to HIC susceptibility. The results obtained from these analyses are used to formulate strategies for material selection to preserve the integrity of the plant and equipment situated in similarly susceptible environments.

Table 2.2 Summary of literature on the susceptibility of steels to embrittlement.

| Material   | Electrolyte   | Test Methods   | Observation  | Reference                |
|--|---|--|--|--------------------------|
| Mild steel (Zn and Zn-Cr) coated on ingress side | 0.5 M Na <sub>2</sub> SO <sub>4</sub> and 1M NaOH       | Permeation test  | Cr enhances permeation rate while Zn reduces it                                      | Boiadjieva et al. 2013   |
| Austenite stainless steel                        | 1 M H <sub>2</sub> SO <sub>4</sub> and 20 mg/l thiourea | Thermal desorption spectroscopy (TDS)                          | Diffusion is higher in metastable in than stable austenitic steel                    | Yagodzinskyy et al. 2011 |
| Duplex stainless steel                           | 0.05 M H <sub>2</sub> SO <sub>4</sub> and 0.1 M NaOH    | Permeation test and tensile test                               | Permeation, diffusivity and cracks increases in ferrite than in austenitic phase     | Luu et al. 2002          |
| Low carbon steel                                 | 0.1 M NaOH and 1 M NaOH                                 | Permeation test  | Lattice diffusion was predominant. Interfaces acts as traps                          | Ichitani et al. 2003     |
| Iron   | 1 M NaOH  | Permeation test in Cyclic Corrosion Test chamber (CCT) and TDS | Diffusible hydrogen content increase with time                                       | Akiyama et al. 2011      |
| Duplex stainless steel                           | H <sub>2</sub> SO <sub>4</sub> and 0.1 M NaOH           | Permeation test and Tensile test                               | Lattice diffusion in ferrite phase and diffusion is higher in ferrite phase          | Chen et al. 2004         |
| Pipeline steel API X70                           | 0.1 M NaOH  | Permeation test and hardness test                              | Diffusivity is enhanced by coarser grain, increased ferrite and very low dislocation | Hag et al. 2013          |
| Pipeline steel API X100                          | H <sub>2</sub> SO <sub>4</sub>                          | Permeation test and tensile test                               | Hydrogen increases with charging time and current density                            | Dong et al. 2009         |
| Pipeline steel L360NCS                           | 5 % NaCl, 0.2 M NaOH                                    | Permeation test  | Permeation current density increases with test temperature                           | Zheng et al. 2013        |
| Duplex stainless steel                           | 26 % NaCl solution                                      | Permeation test and tensile test                               | Ferrite phase was more susceptible to HIC and diffusivity is lower for finer grain   | Chou et al. 1999         |

|                                       |   |  |  |                      |
|---------------------------------------|---|--|--|----------------------|
| TRIP steel                            | 3 % NaCl solution   | Permeation test                          | Permeation current density and diffusivity is lower in TRIP steel than in ferritic steel                         | Kim et al. 2012      |
| Austenitic 316L steel                 |   | Hardness test and tensile test           | Softening of the steel   | Kim et al. 2011      |
| Austenitic steel                      | 3 % NaCl solution   | Tensile test                             | HE exhibited by intergranular fracture   | Koyama et al. 2014   |
| Austenitic alloy                      | 0.1 M NaOH solution   | Permeation test                          | Cr hydrogen enhances solubility  | Ningshen et al. 2001 |
| TWIP steel                            | H <sub>2</sub> SO <sub>4</sub>                                | Tensile test and TDS                     | Diffusion is limited to near-surface region hence ductile fracture   | Ronevich et al. 2012 |
| Carbon steels                         | 0.1 M NaOH solution   | Permeation test and microprint technique | Grain lattice diffusion, carbide-ferrite interface acts as traps   | Luu et al. 1996      |
| TWIP steel                            | 3 % NaCl solution   | Tensile test and TDS technique           | Grain refinement suppress HE due to less local accumulation of hydrogen  | Bai et al. 2016      |
| TWIP steel                            | 3 % NaCL solution   | Tensile test and TDS technique           | Grain refinement enhanced resistance to HE   | Park et al. 2015     |
| TWIP steel                            | 0.05 M H <sub>2</sub> SO <sub>4</sub> solution                | Tensile test and TDS technique           | Grain refinement suppress HE due to less local accumulation of hydrogen  | Zan et al. 2015      |
| Austenitic stainless steel (AISI 304) | NaOH solution   | Permeation test                          | Diffusivity increases with charging current density  | Li et al. 2013       |
| Austenitic steel                      | Pressurised H gas   | Permeation test                          | Martensitic formation enhances permeation and diffusivity  | Xiukui et al. 1989   |
| 310 stainless steel                   | 0.5 M H <sub>2</sub> SO <sub>4</sub> and thiourea             | Tensile test and fatigue test            | High dissolved hydrogen decreases the fatigue strength. HE enhanced by strain induced martensitic transformation | Kishi et al. 2010    |
| Pipeline steel API grade              | 1 M Na <sub>2</sub> CO <sub>3</sub> and 1M NaHCO <sub>3</sub> | Tensile test                             | Increase in the trapping sites enhances material susceptibility to HE  | Arafin et al. 2011   |

|                               |                                      |                                   |  |                       |
|-------------------------------|--------------------------------------|-----------------------------------|--|-----------------------|
| Austenite steel (Fe-Mn-C)     | 3.5 NaCl solution                    | Tensile test and TDS technique    | Ductility was reduced by 40 % and intergranular and transgranular fracture was observed  | Koyama et al. 2012    |
| TWIP steel                    | 3 % NaCl solution                    | Nanoindentation                   | AI reduced HIC   | Han et al. 2014       |
| Nanostructured bainitic steel | 0.1 M NaOH solution                  | TDS technique                     | Trapping occurs at ferrite/austenite interface   | Szost et al. 2013     |
| Steel                         | 1 M H <sub>2</sub> SO <sub>4</sub>   | Tensile test                      | Permeation rate increases with cathodic polarization. Under critical hydrogen treatment causes softening and overcritical causes hardening | Lunarska et al. 1997  |
| High strength steel (MCM 430) | 0.1 NaOH solution                    | Permeation test                   |  | Nishimura et al. 2004 |
| Pure iron                     | 0.1 M NaOH solution                  | Permeation test and TDS technique | Permeation current and apparent solubility increases with increase in temperature  | Addach et al. 2005    |
| High strength steel           | 0.5 M H <sub>2</sub> SO <sub>4</sub> | Tensile test                      | HE index was 60 % for TRIP steel   | Depover et al. 2014   |
| High strength steel           | 0.5 M H <sub>2</sub> SO <sub>4</sub> | TDS technique                     | Diffusible hydrogen can desorb quite fast  | Escobar et al. 2012   |



## Chapter 3      Materials and Experimental Procedure

### 3.1 Materials

#### 3.1.1 Composition

In this study, two ultrahigh-strength steels; i.e. the nanostructured bainitic steel and the twinning-induced plasticity (TWIP) steel were compared with a nominal mild steel. The chemical composition of the steel samples used for this study are shown in Table 3.1. The composition of the alloys was determined by careful design. For the nanostructured bainitic steel it has a high carbon content of 0.7 wt. % and other high alloying elements (Si and Mn). They were selected to enhance hardenability, significantly reduce martensitic  $M_s = 155\text{ }^{\circ}\text{C}$  and isothermal bainite BS  $= 385\text{ }^{\circ}\text{C}$  transformation temperatures. The TWIP steel, on the other hand, was designed to remain as austenite at room temperature by high Mn  $\sim 17\%$  content.

Table 3.1 Chemical composition of the steels used in this study (weight percent).

| Elements       | C    | Mn   | Co   | Si   | Al   | Cr   | Mo   | Fe  |
|----------------|------|------|------|------|------|------|------|-----|
| Bainitic steel | 0.79 | 1.98 | 1.58 | 1.5  | 1.06 | 0.98 | 0.24 | bal |
| TWIP steel     | 0.6  | 18.4 |      |      | 1.48 |      |      | bal |
| Mild steel     | 0.2  | 0.90 |      | 0.10 |      | 0.40 | 0.15 | bal |

#### 3.1.2 Nanostructured Bainitic steel

Generally, bainite consist of aggregates of plates (sheaves) of ferrite separated by untransformed austenite, which are formed when austenitic steel is slowly cooled at low temperature. The austenite steel transforms by shear and diffusional mechanisms, in which the carbon is rejected into the austenite surrounded by carbon depleted bainitic ferrite laths.

The fully bainitic microstructures, which are formed at relatively low transformation temperature range of 200 to 350 °C, have the chemical composition described above (Table 3.1). They are initially reheated to 1100 °C and held for half an hour in a muffle furnace. In order to form a bainitic structure the steel was isothermally held in a salt bath at 200 °C for 10 days or 350 °C for a day, followed by air cooling, to produce two different nanostructured bainitic steels: BS-200 and BS-350 steels. Figure 3.1 shows the heat treatment process for the steels. Although the two steels have the same composition, they exhibit different microstructures and tensile strength.

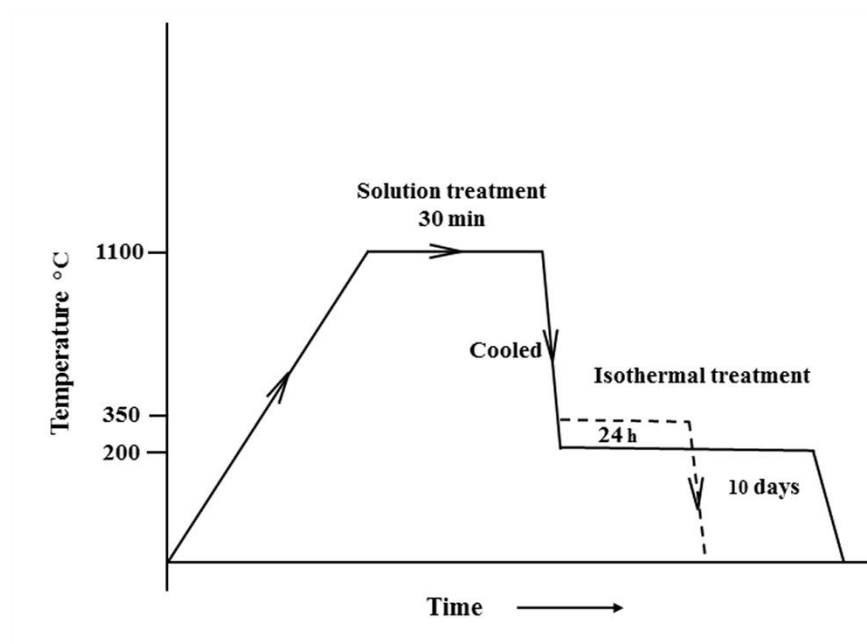


**Figure 3.1 Heat treatment process for nanostructured bainitic steel.**

### **3.1.3 TWIP steel**

In contrast, TWIP steel has a fully austenitic structure even at room temperature. The austenite structure is enhanced by the high manganese content in the chemical composition. TWIP steel is deformed by both gliding of individual dislocations and

mechanical twinning, which leads to an outstanding combination of strength and ductility. The steel is prepared by continuous casting and then hot rolled at 1000 °C to ~40 mm thickness after homogenization at 1200 °C for a period of 2 hours. The finished roll was carried out at room temperature to sheet with a smaller thickness of (2 and 16mm). The heat treatment process for the steel is shown below in Figure 3.2.

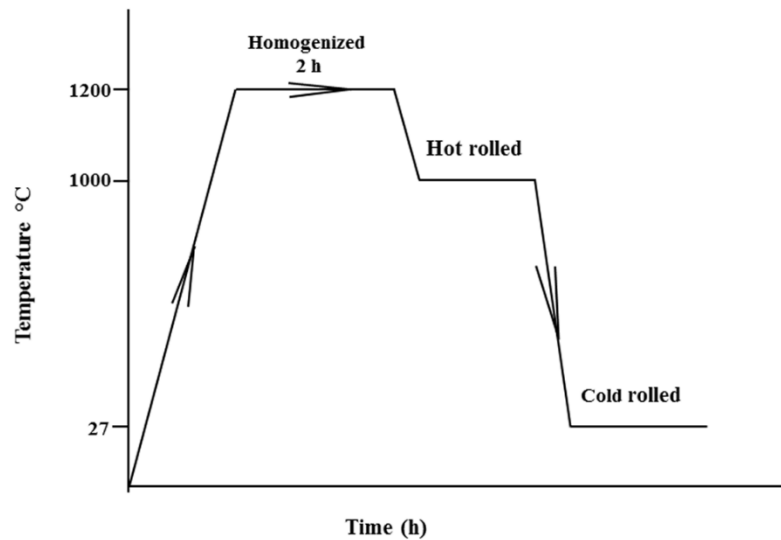


**Figure 3.2 Heat treatment process for TWIP steel.**

### **3.2 Microstructural Analysis**

Optical microscopy, transmission electron microscopy (TEM) and electron back scattering diffraction (EBSD) analyses were carried out to reveal the microstructure of the nanostructured bainitic steel and TWIP steel. The samples were prepared using standard metallographic sample preparation methods, and then etched with 5% Nital solution. The samples were then examined under an optical microscope (model Olympus GX41). The bainite has a refined microstructure and was examined using 200 kV Philips

CM20 operated TEM microscope. Disk foils for TEM examination were made into 3 mm in diameter and 0.07 mm in thickness. The foils were then twin-jet electropolished using a solution of perchloric acid and methanol in a ratio of 5 to 95 pct, at a temperature of -25 °C and a voltage of 50 V. The dislocation density was calculated by measuring the total dislocation line length in a unit volume, giving a parameter in terms of length (m)/m<sup>3</sup>. Using this method, the dislocation density ( $\rho$ ) is given by:

$$\rho = 2N_X/Xt \quad (3.1)$$

where  $N_X$  is the number of intersections with dislocations,  $X$  is the random line length, and  $t$  is the foil thickness.

The total dislocation line length in a unit volume of crystal was measured in terms of length (m) m<sup>-3</sup>. About five bright and dark TEM images at a high magnification (88,000 times) were used. The foil thickness ( $t$ ) was determined as detailed elsewhere (Timokhina et al. 2011; Beladi et al. 2009). The characterisation of the atmosphere around dislocation was determined by maximum separation envelope method using maximum separation distance between atoms of interest of  $d_{\max} = 0.75$  and 1 nm and a grid spacing of 0.1 nm. An average of 20 section was chosen to eliminate fluctuation (Timokhina et al. 2011).

A field emission gun FEGLEO 1530 scanning electron microscope (SEM) operated at 20 kV was used for electron backscatter diffraction (EBSD) analysis of both TWIP and mild steels. The sample preparation for EBSD analysis was done by a standard mechanical grinding followed by polishing with a colloidal silica slurry. The EBSD map was acquired at 20 kV with a step size of 0.15 µm. For the tensile samples, scanning electron microscopy (SEM) (Model: Jeol JSM 541OLV) was then used to evaluate the

ductile or brittle mode of the fractured surfaces of the tensile samples in the hydrogen uncharged and hydrogen charged conditions.

### 3.3 Electrochemical Permeation Test

Electrochemical hydrogen permeation tests were carried out in a polycarbonate Devanathan-Stachurski (DS) cell, constructed in-house. It was comprised of a double compartment with the sample sandwiched between them; i.e. the anodic and cathodic cell. DS cells are used to determine the hydrogen permeation behavior in a wide variety of metals and hence measure the hydrogen diffusivity of such materials. A schematic diagram of the cell set-up is shown in Figure 3.3.

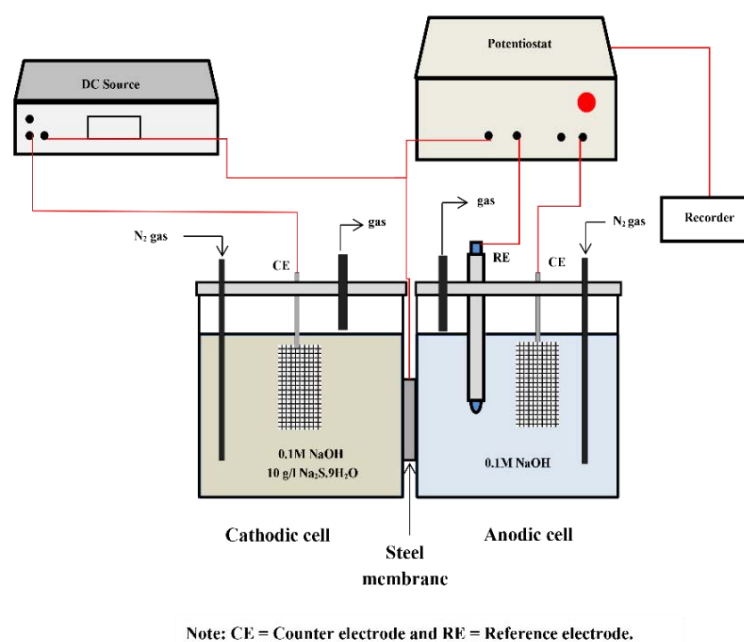


**Figure 3.3 Schematic diagram of Devanathan-Stachurski permeation cell set-up.**

Prior to the test, samples (0.05 cm thick) were ground with SiC papers up to 1200 grit SiC paper and ultrasonically cleaned with distilled water, acetone and ethanol. One side was electroplated with nickel, using a current density of 3 mA/cm<sup>2</sup> for 180 s in a Watt's bath at 60 °C. The Watt's bath contains NiSO<sub>4</sub>·6H<sub>2</sub>O 250 g/l, NiCl<sub>2</sub>·6H<sub>2</sub>O 45 g/l and

$\text{H}_3\text{BO}_3$  40 g/l. The side plated with nickel was exposed to the anodic cell, and a silver/silver chloride (Ag/AgCl) served as reference electrode, while platinum electrodes were used as counter electrode in both compartments. The two compartments were filled with different electrolytes, the anodic compartment being controlled by a potentiostat (Model: Gillac ACM) and the cathodic side controlled by a DC source (Model: Powertech MP-3084). Prior to the testing, the two compartments with electrolytes were vigorously purged with nitrogen for 15 minutes. They were then gently purged throughout the experiment in order to reduce the oxygen concentration in the electrolyte, which could corrode the sample and consequently hinder the hydrogen permeation.

The anodic side of the cell; i.e. the sample side with nickel plating, was filled with 0.1 M NaOH solution. A constant potential of + 300 mV (w.r.t. Ag/AgCl electrode) was applied to the anodic side of the sample. The oxidation current, known as background current, decreased with time to a minimum, which was taken as zero current for the purpose of plotting the hydrogen permeation curves. Once a steady-state minimum current was achieved, hydrogen was generated in the cathodic compartment, which was filled with a solution containing 0.1 M NaOH and a hydrogen promoter (10 g/l of  $\text{Na}_2\text{S} \cdot 9\text{H}_2\text{O}$ ) (Hag et al. 2013), using a constant current density 2, 10, 20, 30 mA/cm<sup>2</sup>. As the polarization of the anodic side continued, the oxidation current was monitored until a steady state current was achieved. In order to identify any significant irreversible trapping sites in the steel samples, after the oxidation current reached a steady state the cathodic charging was stopped, and the anodic current was measured, which subsequently was decreased to a minimum, representing the degassing part of the curve. Three hydrogen permeation transient curves were obtained by hydrogen charging and degassing cycles. The test was carried out at ambient temperature, however to observe the effect of temperature on

hydrogen diffusion, electrolyte was circulated through the system, which was maintained at different temperatures: 30, 40 and 50 °C respectively.

The hydrogen permeation flux  $J$  (mol/cm<sup>2</sup>.s) was calculated from the permeation current density  $I_p$  (A/cm<sup>2</sup>) using the following relationship (Turnbull 1994):

$$J = I_p/nF \quad (3.2)$$

where  $n$  is the number of electrons transferred and  $F$  is Faraday's constant.

The hydrogen permeation rate  $Q$  (mol/cm s) was obtained from the permeation flux, as follows:

$$Q = J.L \quad (3.3)$$

where  $L$  (cm) is the sample thickness.

The effective hydrogen diffusivity  $D$  (cm<sup>2</sup>/s) was calculated from the breakthrough time:

$$D = L^2/15.3t_b \quad (3.4)$$

where  $t_b$  is the breakthrough time, which was taken as the time required for the anodic current to increase after the cathodic charging.

The hydrogen solubility is given by  $C$  (mol/cm<sup>3</sup>):

$$C = Q/D \quad (3.5)$$

### 3.4 Hydrogen Depth Profiling Analysis

This technique of hydrogen depth profile determination by proton elastic recoil detection uses helium ion beams with energy in the range of 2.0 to 2.5 MeV from the Van de Graaff accelerator. The hydrogen concentration profiles were obtained by simulating the experimental proton recoil spectra, taking into account the effects of energy straggling,

multiple scattering in the target and Al stopper foil and the detector energy resolution. The hydrogen depth profile of a material can be evaluated using microhardness measurement and ERDA analysis. These methods are most suitable for small sized materials. The mechanical property (e.g. hardness) of a sample changes with respect to the depth to which hydrogen can diffuse into the material. Hence, these tests were employed on the nanostructured bainitic steel BS-200 and BS-350 to evaluate hardness along its cross-section of steel when charged from one side.

#### **3.4.1     *Micro hardness***

Microhardness tests were carried out on uncharged and hydrogen charged (H-charged) samples of BS-200, BS-350 and mild steel. The small coupon with dimensions: 20×20×2 mm was initially prepared through standard metallographic sample preparation. Samples for hydrogen charging were mounted in a resin to expose one side of the sample to the electrolyte in a typical two-electrode cell, with the sample as the working electrode and a platinum mesh as the counter electrode. The electrolyte contained 0.1 M NaOH and a hydrogen promoter (10 g/l of Na<sub>2</sub>S.9H<sub>2</sub>O) (Haq et al. 2013). Hydrogen was generated by electrochemical cathodic charging using a DC source (Model: Powertech MP-3084). A constant current density of 10 mA/cm<sup>2</sup> was applied for a period of 6 h. Prior to the hydrogen charging, the electrolyte was vigorously purged with nitrogen gas for 15 min. The electrolyte was then gently purged throughout the experiment to reduce the oxygen concentration (to reduce corrosion) in the electrolyte.

Microhardness measurements were carried out using an automated Zwick hardness tester (Model: ZHV<sub>μ</sub>). The hardness measurements were performed immediately after H-charging by applying a load of 200 gf with a load time of 10 s. The hardness test was done both on the surface and along the cross section for depth profile at a distance interval



of 0.2 mm along the cross-section for the uncharged and H-charged steels for comparison.

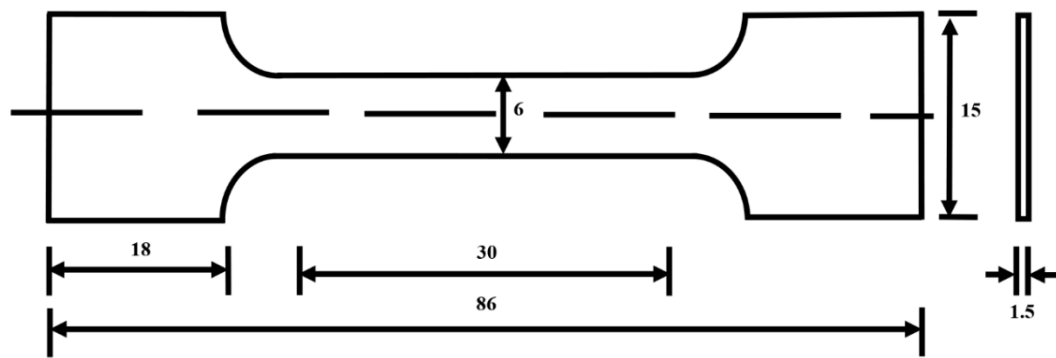
#### ***3.4.2 Elastic Recoil Detection Analysis (ERDA) technique***

ERDA was performed on the H-charged steels at the Australian Nuclear Science and Technology Organisation (ANSTO) Ion Beam Facility within the Centre for Accelerator Science (CAS). The samples were installed on a beamline serviced by the 2MV STAR tandem accelerator. The subsurface hydrogen profile was done using 1.8 MeV He<sup>+</sup> ions impinging on the sample surface at an angle of 72° relative to the sample, which had enough energy to recoil the lighter hydrogen (H) atoms from the sample up to a depth of ~1.5 m. The energy of recoiled H was measured using a silicon surface barrier detector placed at a scattering angle of 32° to the incoming beam, with an 8.5 µm Mylar foil filter used to stop the helium (He) scattered by the sample surface and by a 1 x 2 mm<sup>2</sup> 4-way slits that reduced the energy spread and defined a solid angle of 0.8 msr. The number of He ions impinging upon the sample was monitored by measuring the drain current of the sample holder, which was around 5 nA, and accounting for secondary electrons. The result of H yield versus energy (or channel number) was compared with a calculated result generated with SIMNRA software (Mayer et al. 1997).

The results of H measurement on the samples at room temperature were obtained by integrating the area under the H peak and comparing it with Kapton, which contains 24 at% H, and it is stable under the 1.8 MeV He beam. The depth distribution of H was obtained from the energy loss of He in the sample, by making use of the stopping power data incorporated in the SIMNRA analysis software.

### 3.5 Mechanical Tensile Test

The mechanical properties of an uncharged sample can be compared to an H-charged sample to determine its susceptibility of HIC often by a tensile test machine. The materials that were used for this test were cut into dog bone shape in flat bars. The as-received TWIP steel which was in the form of a block with dimension  $120 \times 87 \times 16$  mm was cut into flat specimens. The flat tensile specimens with gauge dimensions  $(30 \times 6 \times 1.5)$  mm were cut by an Electrical Discharge Machining (EDM) in the rolling direction as shown in Figure 3.4.



Dimensions in mm

Figure 3.4 The geometry of tensile specimen used for mechanical tests.

The specimens were then ground through 1200 grit SiC paper and degreased by ethanol and then acetone prior to the tensile test. The HIC susceptibility of the TWIP steel was studied using tensile test method in order to evaluate the changes in its mechanical properties under uncharged and hydrogen charged (pre-charged and in-situ charged) conditions. Tensile tests were conducted at room temperature  $\sim 25$  °C at a strain rate of  $2 \times 10^{-4}$ /s for the pre-charged conditions and at  $5 \times 10^{-6}$ /s for the in-situ charged conditions (Figure 3.5).

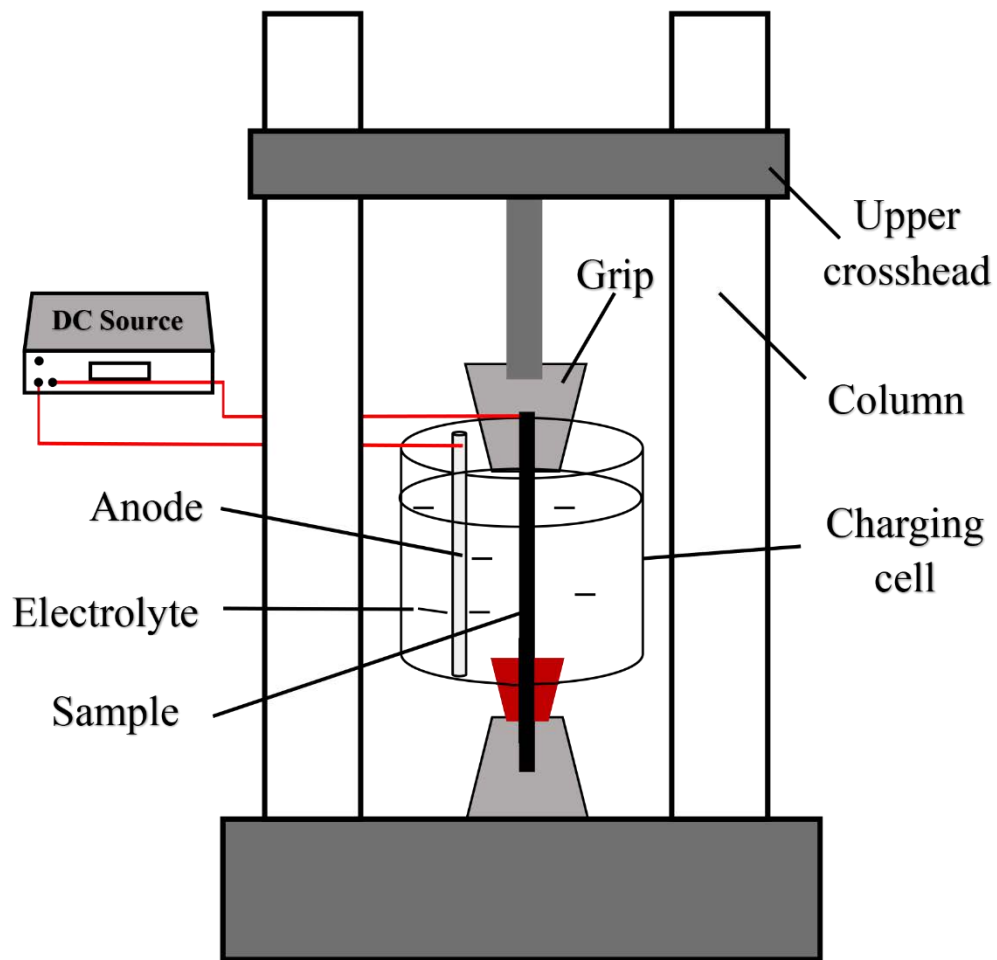


**Figure 3.5 Experimental set up of in-situ charged sample.**

Three tests were done for each uncharged and hydrogen charged specimen to ensure reproducibility. Tests were carried out along the rolling direction (RD) using a United Model SSTM Universal Electro Mechanical Testing Machine. Prior to the test, the gripping sections of samples were sealed with Teflon tape and the exposed portions were charged in an electrolyte solution containing 0.1 M NaOH and a hydrogen promoter (10 g/l of  $\text{Na}_2\text{S} \cdot 9\text{H}_2\text{O}$ ). The specimens were electrochemically charged using a constant current density of  $10 \text{ mA/cm}^2$  for a period of 24 h at room temperature, using stainless steel as counter electrode for pre-charged samples. Tensile tests were carried out on the

pre-charged samples within 5 min from the end of the charging. To understand the effect of temperature on the susceptibility of the steel to HIC, additional tests were done by pre-charging the samples with a constant current density of  $10 \text{ mA.cm}^{-2}$  for a period of 24 h at temperature of 25, 30, 40 and 50 °C.

For the in-situ charged samples, tests were performed at slow strain rate while the samples were being continuously charged in the electrolyte. The strain was determined from the gauge length before and after the tests and a stress-strain curve was obtained from the load-displacement data. The results were then compared to tests done on nominal mild steel samples under the same test conditions.

The HIC susceptibility ( $I_{HIC}$ ) was evaluated using elongation to failure  $\mathcal{E}_f$  (change in gauge length before and after the fracture) and the reduction in area ( $RA$ ) measured in both uncharged and hydrogen charged conditions and given by:

$$I_{HIC} = (\mathcal{E}_f \text{ or } RA)_{air} - (\mathcal{E}_f \text{ or } RA)_{charged} / (\mathcal{E}_f \text{ or } RA)_{air} \quad (3.5)$$

After the mechanical tests, macrographs of the fractured tensile samples were obtained with an optical microscope, and the fractured surfaces were examined on a scanning electron microscope (SEM).

## **Chapter 4      Hydrogen Permeation in Nanostructured Bainitic Steel (Publication)**

### **4.1 Introduction**

Microstructure plays a vital part in the HIC susceptibility of high-strength steels. The degree to which the different microstructural constituents of nanostructured bainitic steel affect the rate of hydrogen diffusion and therefore its susceptibility to HIC is not fully established, hence in this chapter microstructural analysis of the steels (BS-200 and BS-350) having the same chemical composition was performed. In addition, a DS hydrogen permeation cell technique was used on a thin steel membrane in order to understand the hydrogen diffusion mechanism in the nanostructured bainitic steel. The effective hydrogen diffusivity was then determined by Fick's law and results were compared to tests done on mild steel.

#### **4.1.1      *Optical microstructures***

The optical micrographs of the nanostructured bainitic steel and mild steel are shown in Plates 4.1(a) through (c). The micrographs revealed fine needle-like structures in the nanostructured bainitic steel and coarse equiaxed grains in the mild steel. The needle-like structures for BS-200 steel were finer than that of BS-350 steel.

#### **4.1.2      *TEM microstructures***

The TEM micrographs of the nanostructured bainitic steel are shown in Plate 4.2. TEM observations revealed predominant bainite morphology for both the heat-treated conditions. The bainite grains consisted of nano-layers of bainitic ferrite with an average thickness of  $60 \pm 10$  nm and nano-layers of retained austenite with an average thickness of  $30 \pm 5$  nm for the BS-200 steel.

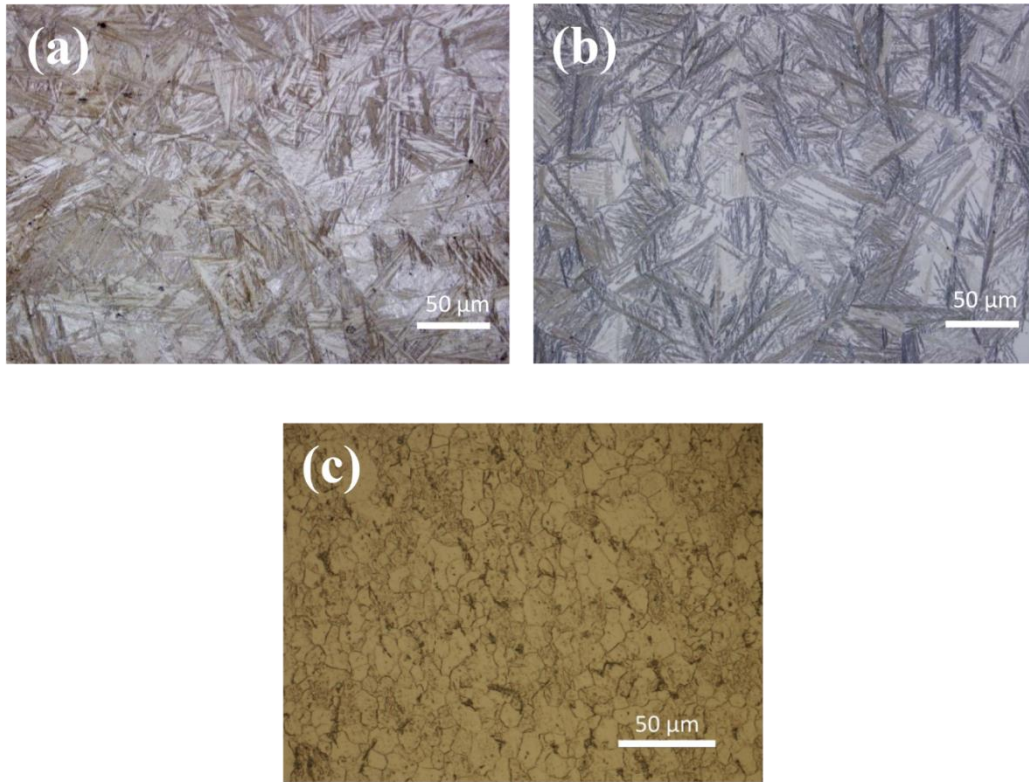


**Plate 4.1 Optical micrographs of: (a) BS-200 nanostructured bainitic steel, (b) BS-350 nanostructured bainitic steel and (c) mild steel.**

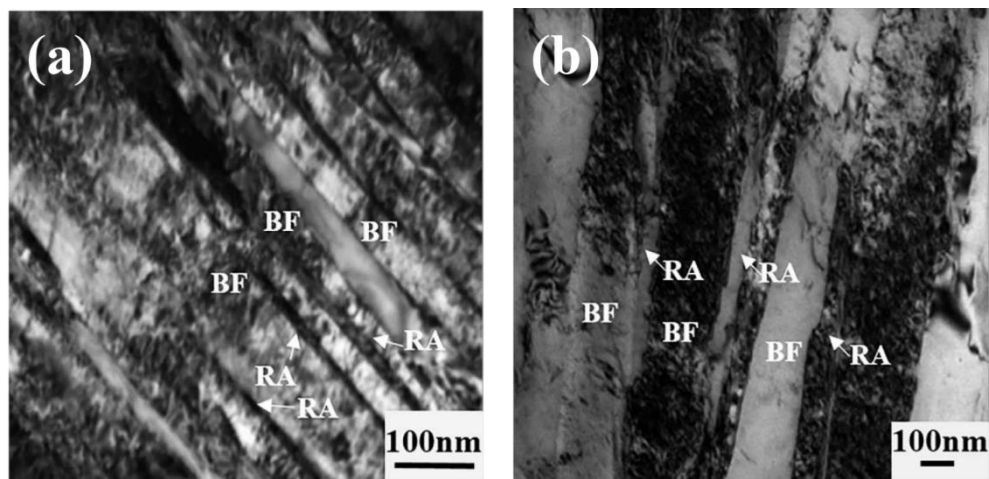


**Plate 4.2 TEM micrographs of nanostructured bainitic steel: (a) BS-200 and (b) BS-350 (Note: RA is retained austenite and BF is bainitic ferrite).**

As compared to BS-200 steel, the bainitic ferrite thickness and also the retained austenite thickness were greater for BS-350 steel; i.e. in the range of 200 to 400 nm and  $70 \pm 30$  nm, respectively. It was observed that the bainitic ferrite and retained austenite layers

formed colonies or sheaves, and the layers or sub-units of bainitic ferrite and residual austenite were parallel to each other. The volume fraction of the bainitic ferrite was  $79 \pm 2$  and  $47 \pm 2$  % for the BS-200 steel and BS-350 steel, respectively. The dislocation density of bainitic ferrite for the BS-200 steel was  $4.7 \times 10^{15}/\text{m}^2$  and  $2 \times 10^{15}/\text{m}^2$  for BS-350 steel.

#### 4.1.3 *Effective hydrogen diffusivity*

The hydrogen permeation curves for the nanostructured bainitic steel and mild steel are shown in Figure 4.1. The electrochemical parameters obtained from the permeation curves are shown in Table 4.1. The permeation curves for the steel samples revealed a region of increasing current density, and a second region where the current density reached a steady state.

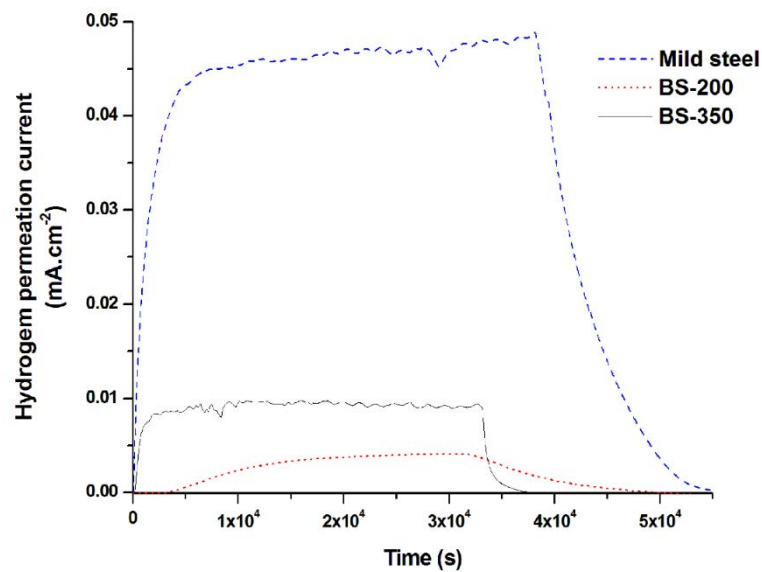


**Figure 4.1** Hydrogen permeation curves for the nanostructured bainitic steel and mild steel.

Table 4.1 Hydrogen permeation data for the mild steel and nanostructured bainitic steel (first transient).

|                              | Mild steel                           | BS-200                               | BS-350                                |
|------------------------------|--------------------------------------|--------------------------------------|---------------------------------------|
| $L$ (cm)                     | 0.05 ( $\pm 0.005$ )                 | 0.05 ( $\pm 0.005$ )                 | 0.05 ( $\pm 0.005$ )                  |
| $t_b$ (s)                    | 90 ( $\pm 30$ )                      | 3150 ( $\pm 260$ )                   | 180 ( $\pm 30$ )                      |
| $I_p$ (A/cm <sup>2</sup> )   | $4.61 \times 10^{-5}$ ( $\pm 0.37$ ) | $3.89 \times 10^{-6}$ ( $\pm 0.26$ ) | $8.89 \times 10^{-6}$ ( $\pm 0.01$ )  |
| $J$ (mol/cm <sup>2</sup> .s) | $4.78 \times 10^{-14}$ ( $\pm 0.3$ ) | $4.03 \times 10^{-15}$ ( $\pm 0.3$ ) | $9.21 \times 10^{-15}$ ( $\pm 0.01$ ) |
| $Q$ (mol/cm.s)               | $2.39 \times 10^{-15}$ ( $\pm 0.3$ ) | $2.02 \times 10^{-16}$ ( $\pm 0.3$ ) | $4.61 \times 10^{-16}$ ( $\pm 0.01$ ) |
| $D$ (cm <sup>2</sup> /s)     | $1.82 \times 10^{-6}$ ( $\pm 0.20$ ) | $5.19 \times 10^{-8}$ ( $\pm 0.31$ ) | $9.08 \times 10^{-7}$ ( $\pm 0.15$ )  |

Mean  $\pm$  Standard deviation; n = 3

The  $t_b$  for mild steel was lower than that of the nanostructured bainitic steel. Hydrogen diffused from the cathodic side of mild steel to the anodic side ( $t_b$ ) in  $\sim 90$  s, whereas it took 3150 s for BS-200 steel and 180 s for BS-350 steel. Notably, the difference in  $t_b$  between BS-200 steel and BS-350 steel was highly significant. The measured  $I_p$  values for mild steel, BS-200 steel and BS-350 steel were  $4.61 \times 10^{-5}$  A/cm<sup>2</sup>,  $3.89 \times 10^{-6}$  A/cm<sup>2</sup> and  $8.89 \times 10^{-6}$  A/cm<sup>2</sup> respectively. The mild steel showed an  $I_p$  which was close to an order of magnitude higher than that of the nanostructured bainitic steel, BS-200 steel, which showed lower  $t_b$  also exhibited lower  $I_p$ . The calculated effective diffusivity values were as follows: mild steel –  $1.82 \times 10^{-6}$  cm<sup>2</sup>/s; BS-200 –  $5.19 \times 10^{-8}$  cm<sup>2</sup>/s; BS-350 –  $9.08 \times 10^{-7}$  cm<sup>2</sup>/s. The effective diffusivity results clearly suggested that nanostructured bainitic steel is more resistant to hydrogen diffusion compared to mild steel. The results also suggested that the microstructural difference between the BS-200 and BS-350 has significantly contributed to the difference in their hydrogen diffusion behaviours.

In order to identify any irreversible traps, a secondary permeation cycle; i.e. after degassing of the first cycle, was conducted, and the permeation curves are presented in Figure 4.2.



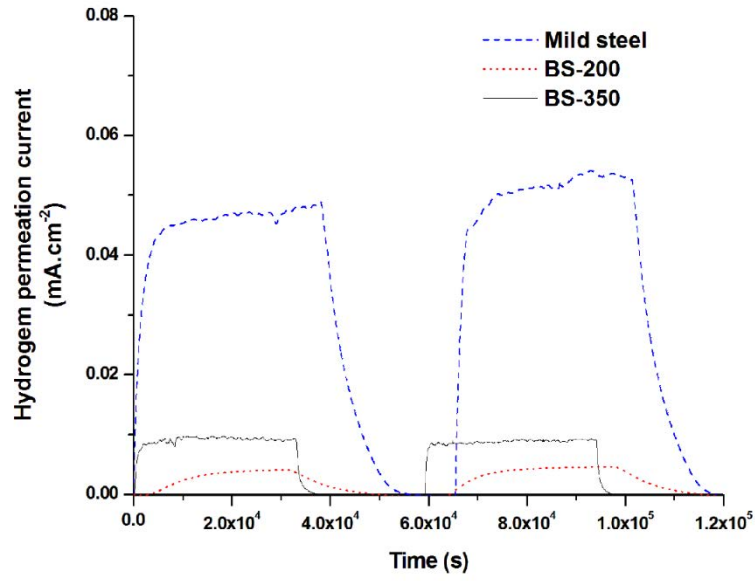


**Figure 4.2 Hydrogen permeation curves for the steels showing double transient curves.**

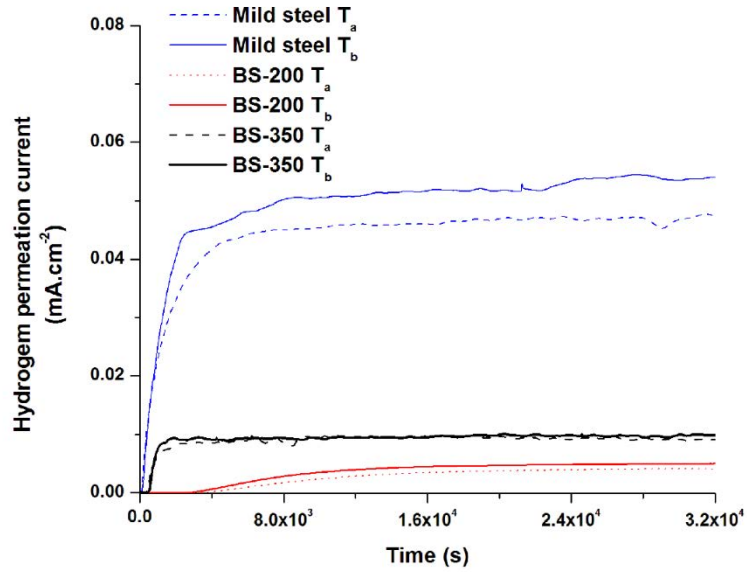


**Figure 4.3 Overlay of the double transient curves for the steels (Note:  $T_a$  is the first transient and  $T_b$  is the second transient).**

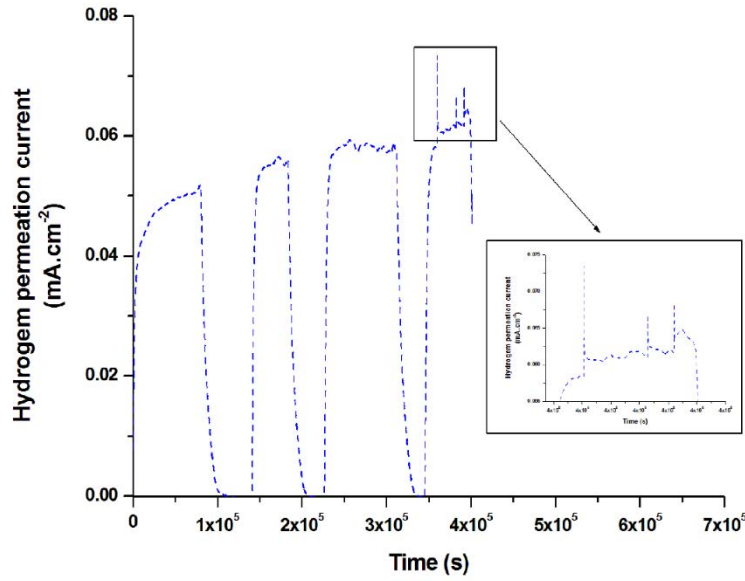
For comparison, the permeation curves for the second cycle was overlayed with the first cycle (Figure 4.3). The electrochemical parameters obtained from the second permeation curves are presented in Table 4.2.

Table 4.2 Hydrogen permeation data for the mild steel and nanostructured bainitic steel (second transient).

|                              | Mild steel                           | BS-200                               | BS-350                               |
|------------------------------|--------------------------------------|--------------------------------------|--------------------------------------|
| $L$ (cm)                     | 0.05 ( $\pm 0.005$ )                 | 0.05 ( $\pm 0.005$ )                 | 0.05 ( $\pm 0.005$ )                 |
| $t_b$ (s)                    | 80 ( $\pm 30$ )                      | 3000 ( $\pm 230$ )                   | 150 ( $\pm 60$ )                     |
| $I_p$ (A/cm <sup>2</sup> )   | $5.13 \times 10^{-5}$ ( $\pm 0.32$ ) | $4.40 \times 10^{-6}$ ( $\pm 0.22$ ) | $9.10 \times 10^{-6}$ ( $\pm 0.21$ ) |
| $J$ (mol/cm <sup>2</sup> .s) | $5.32 \times 10^{-14}$ ( $\pm 0.3$ ) | $4.56 \times 10^{-15}$ ( $\pm 0.2$ ) | $9.43 \times 10^{-15}$ ( $\pm 0.2$ ) |
| $Q$ (mol/cm.s)               | $2.66 \times 10^{-15}$ ( $\pm 0.3$ ) | $2.28 \times 10^{-16}$ ( $\pm 0.2$ ) | $4.72 \times 10^{-16}$ ( $\pm 0.2$ ) |
| $D$ (cm <sup>2</sup> /s)     | $2.04 \times 10^{-6}$ ( $\pm 0.26$ ) | $5.45 \times 10^{-8}$ ( $\pm 0.27$ ) | $1.09 \times 10^{-6}$ ( $\pm 0.20$ ) |

Mean  $\pm$  Standard deviation; n = 3

The  $I_p$  values for the second permeation curves were marginally higher compared to those of the first permeation curves for all the steel samples. As compared to the first cycle, the  $t_b$  values of the second cycles were marginally lower, for mild steel (80 s), BS-200 steel (3000 s) and BS-350 steel (150 s). Accordingly, the measured effective diffusivity did not change significantly (as compared to the first cycle) for mild steel ( $2.04 \times 10^{-6}$  cm<sup>2</sup>/s), for BS-200 steel ( $5.45 \times 10^{-8}$  cm<sup>2</sup>/s) and BS-350 steel ( $1.09 \times 10^{-6}$  cm<sup>2</sup>/s). The similarity of the first and second transients (Figure 4.3) for both the nanostructured bainitic steel, indicated that irreversible traps have no significant effect on hydrogen diffusion in the steel. Interestingly, the second steady state current was marginally higher for the mild steel compared to the nanostructured bainitic steels. To further understand this increase in mild steel a third and fourth transient plot was done, which showed a further increase (Figure 4.4).



**Figure 4.4 Hydrogen permeation curves for the mild steels showing multiple transient curves.**

The reason for such an increase in permeation current may be associated with the formation and propagation of cracks. In fact, the fluctuation in permeation current represented cracks being created. The observed difference in the diffusion of hydrogen can be attributed to the microstructure of the steels. The grain boundaries and the grain lattice having low trap binding energies are the most probable path for diffusion. Other features such as microvoids, austenite/ferrite interface and the ferrite phase also have low trap binding energies and are considered as reversible traps. On the other hand, inclusions, precipitates and austenite phase are associated with high binding energies. Generally, diffusion of hydrogen is higher in steel with a microstructure containing lower trap binding energy. Hence, hydrogen diffusion through grain boundaries is higher than through the grain lattice (Haq et al. 2013), and for lattice diffusion, the ferrite phase exhibits higher hydrogen diffusivity as compared to the austenite phase (Xu et al. 1993; Olden et al. 2008).

Primarily, the microstructure of the nanostructured bainitic steel is comprised of a very fine bainitic ferrite and retained austenite layers (30 to 400 nm). The refined

austenite/ferrite interface effectively traps hydrogen and also reduces the movement of the mobile untrapped hydrogen by a tortuosity factor caused by reduction of cross sectional area free for diffusion. The effective diffusivity of hydrogen in BS-200 was  $5.19 \times 10^{-8} \text{ cm}^2/\text{s}$  and an order of magnitude lower than for BS-350 ( $9.08 \times 10^{-7} \text{ cm}^2/\text{s}$ ). The schematic model illustrating the interaction of hydrogen within the different steels is shown in Figure 4.5.

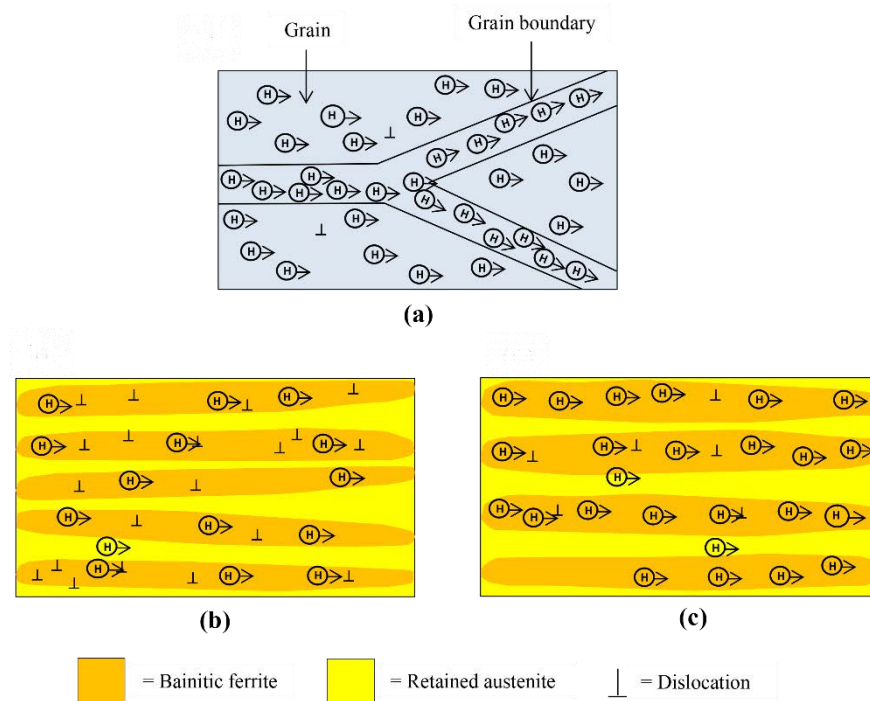


**Figure 4.5 Schematic model illustrating interaction between hydrogen and the different microstructure of (a) mild steel, (b) BS-200, and (c) BS-350. (Note: not drawn to scale).**

In mild steel Figure 4.5(a), hydrogen diffused through the grain boundaries and the ferrite with minimal resistance, hence it showed a higher diffusion of  $1.82 \times 10^{-6} \text{ cm}^2/\text{s}$ . When comparing the nanostructured bainitic steels (Figure 4.5(b) and (c)), BS-200 exhibited high resistance to hydrogen diffusion as compared to BS-350. This can be attributed to the finer grains in BS-200, which increased the mean path for hydrogen diffusion. In addition to the influence of the grain refinement on the effective diffusivity of hydrogen,

the phases present in the steel had a contributory effect. The steel was isothermally transformed by a shear mechanism into a bainitic ferrite phase which contains high dislocation density, and the rest is the residual (retained) austenite phase. As the hydrogen prefers to diffuse through the ferrite phase due to the higher hydrogen diffusivity in this phase as compared to the austenite phase, the BS-200 steel was expected to show higher hydrogen diffusivity, as the BS-200 steel contained a higher volume fraction of the bainitic ferrite phase (~79 %) compared to the BS-350 steel (~47 %). Interestingly, the effective diffusivity of hydrogen observed for the BS-200 steel was lower than that of the BS-350 steel. Since the BS-200 steel was formed at a lower temperature as compared to the BS-350 steel, the BS-200 steel exhibited a higher dislocation density. Reports in the literature indicate that higher dislocation density reduces hydrogen mobility by acting as hydrogen trapping sites (Haq et al. 2013; Fielding et al. 2014; Kumnick and Johnson 1980). Hence, the lower effective diffusion observed in BS-200 steel can be attributed to the higher dislocation density ( $4.7 \times 10^{15}/\text{m}^2$ ) as compared to BS-350 steel ( $2 \times 10^{15}/\text{m}^2$ ). Overall, the study suggested that the high strength nanostructured bainitic steel exhibited lower effective diffusivity of hydrogen as compared to the mild steel due to the difference in the microstructures. The fine-grained nanostructured bainitic steel provided higher resistance to hydrogen diffusion. The lower hydrogen diffusion in BS-200 steel as compared to BS-350 steel was attributed to both finer grains and higher dislocation density in the bainitic ferrite phase.

Based on the hydrogen permeation studies, the effective diffusivity of hydrogen for nanostructured bainitic steel was lower than that of mild steel. Transformation temperature and consequent change in the microstructure played a significant role in the hydrogen permeation behaviour of nanostructured bainitic steel. BS-200 steel - (200 °C) which exhibited 79 % (volume fraction) of bainitic ferrite showed lower effective

diffusivity of hydrogen than BS-350 steel, with 47 % (volume fraction) bainitic ferrite. Finer microstructure constituents (i.e. bainitic ferrite and retained austenite) and higher dislocation density in the bainitic ferrite of BS-200 steel can be credited for its lower effective diffusivity of hydrogen, as compared to BS-350 steel and mild steel.

## **4.2 Effect of Hydrogen-Charging Current Density on Hydrogen Diffusion in Nanostructured Bainitic Steels (Publication)**

To understand the effect of the cathodic hydrogen-charging current density on the effective hydrogen diffusivity in the bainitic steel, a new set of samples was tested by increasing the charging current density. The influence of increased supply of hydrogen was then evaluated.

### **4.2.1 *Effective hydrogen diffusivity***

The hydrogen permeation curves for the nanostructured bainitic steels (BS-200 and BS-350) and the mild steel at different cathodic current densities; i.e. 10, 20 and 30 mA/cm<sup>2</sup>, are shown in Figure.4.6. The electrochemical permeation parameters which were obtained from the permeation curves are given in Table 4.3.

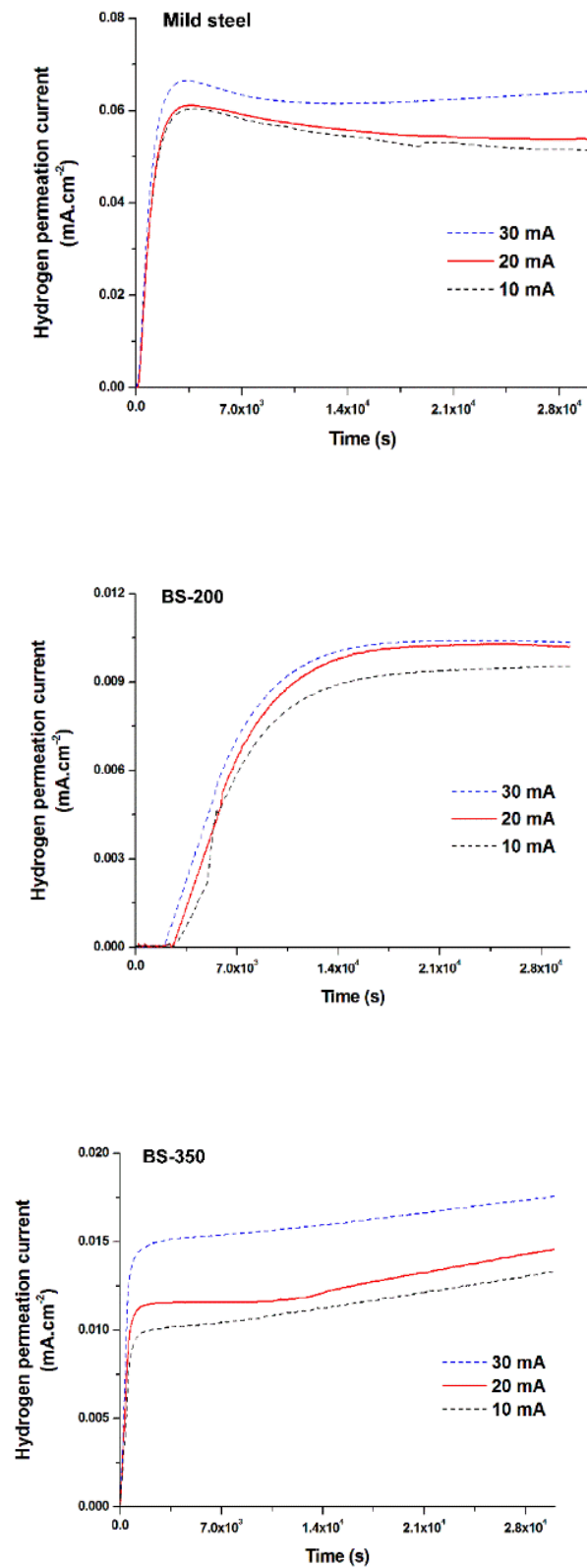


**Figure 4.6** Hydrogen permeation curves for mild steel, BS-200 and BS-350 nanostructured bainitic steels, cathodically hydrogen-charged at different hydrogen-charging current densities.

Table 4.3 Hydrogen permeation data for mild steel, BS-200 and BS-350 nanostructured bainitic steels.

| Material   | Charging current (mA/cm <sup>2</sup> ) | $I_p$ (A/cm <sup>2</sup> )   | $J$ (mol/cm <sup>2</sup> .s) | $Q$ (mol/cm.s)         | $t_b$ (s) | $D$ (cm <sup>2</sup> /s) |
|------------|--|------------------------------|------------------------------|------------------------|-----------|--------------------------|
| Mild steel | 10                                     | $6.03 \times 10^{-5} (0.35)$ | $3.12 \times 10^{-14}$       | $1.56 \times 10^{-15}$ | 82(15)    | $1.99 \times 10^{-6}$    |
|            | 20                                     | $6.11 \times 10^{-5} (0.20)$ | $3.17 \times 10^{-14}$       | $1.58 \times 10^{-15}$ | 60(10)    | $2.72 \times 10^{-6}$    |
|            | 30                                     | $6.65 \times 10^{-5} (0.30)$ | $3.45 \times 10^{-14}$       | $1.72 \times 10^{-15}$ | 35(5)     | $4.67 \times 10^{-6}$    |
| BS-200     | 10                                     | $9.58 \times 10^{-6} (0.15)$ | $4.96 \times 10^{-15}$       | $2.48 \times 10^{-16}$ | 2610(280) | $6.26 \times 10^{-8}$    |
|            | 20                                     | $1.02 \times 10^{-5} (0.26)$ | $5.28 \times 10^{-15}$       | $2.64 \times 10^{-16}$ | 2550(150) | $6.41 \times 10^{-8}$    |
|            | 30                                     | $1.04 \times 10^{-5} (0.23)$ | $5.39 \times 10^{-15}$       | $2.69 \times 10^{-16}$ | 1950(100) | $8.38 \times 10^{-8}$    |
| BS-350     | 10                                     | $1.00 \times 10^{-5} (0.20)$ | $5.18 \times 10^{-15}$       | $2.59 \times 10^{-16}$ | 150(20)   | $1.09 \times 10^{-6}$    |
|            | 20                                     | $1.15 \times 10^{-5} (0.23)$ | $5.96 \times 10^{-15}$       | $2.98 \times 10^{-16}$ | 100(10)   | $1.63 \times 10^{-6}$    |
|            | 30                                     | $1.52 \times 10^{-5} (0.34)$ | $7.88 \times 10^{-15}$       | $3.94 \times 10^{-16}$ | 60(10)    | $2.72 \times 10^{-6}$    |

Mean (SD); n = 3

The hydrogen flux through the sample was again measured in terms of steady state permeation current,  $I_p$  (A/cm<sup>2</sup>), and converted to steady-state hydrogen permeation flux,  $J$  (mol/cm<sup>2</sup>.s) accordingly. The permeation curves of the steels again also showed two regions; i.e. an increase in permeation current with respect to time and a relative steady-state current. Interestingly, the permeation curves for mild steel at high cathodic charging current of 10 mA/cm<sup>2</sup> displayed a peak current which slowly decayed with time to a steady-state level. Similar behavior has been reported for API X65 pipeline steel (Park et al. 2008; Scoppio and Barteri 1994), which was attributed to reactions at the surface or defects in the steel at high cathodic current density.

This phenomenon is reported to impede diffusion and/or induce cracks (Akiyama et al. 2011; Sakamoto and Katayama 1982; Fielding et al. 2014). The  $I_p$  for the mild steel charged at 10 mA/cm<sup>2</sup> was measured to be  $6.03 \times 10^{-5}$  A/cm<sup>2</sup>. The  $I_p$  values increased by ~1.3% and 9% when the charging current was increased to 20 mA/cm<sup>2</sup> and 30 mA/cm<sup>2</sup>, respectively.



The  $t_b$  for the mild steel decreased with the increase in the charging current density; i.e.  $10 \text{ mA/cm}^2 = 82 \text{ s}$ ,  $20 \text{ mA/cm}^2 = 60 \text{ s}$  and  $30 \text{ mA/cm}^2 = 35 \text{ s}$ , which suggested that the hydrogen diffused faster from the cathodic side to the anodic side with the increase in the charging current. Thus, the effective hydrogen diffusivity also increased with the increase in the charging current:  $10 \text{ mA/cm}^2 = 1.99 \times 10^{-6} \text{ cm}^2/\text{s}$ ,  $20 \text{ mA/cm}^2 = 2.72 \times 10^{-6} \text{ cm}^2/\text{s}$  and  $30 \text{ mA/cm}^2 = 4.67 \times 10^{-6} \text{ cm}^2/\text{s}$ .

In comparison to the mild steel, BS-200 exhibited a much lower  $I_p$  value ( $9.58 \times 10^{-6} \text{ A/cm}^2$ ) at  $10 \text{ mA/cm}^2$ . As the charging current increased to  $20 \text{ mA/cm}^2$  and  $30 \text{ mA/cm}^2$ , the  $I_p$  values increased to  $1.02 \times 10^{-5} \text{ A/cm}^2$  and  $1.04 \times 10^{-5} \text{ A/cm}^2$ , respectively. The  $t_b$  was significantly higher for BS-200 as compared to that of mild steel at all the charging current densities. With the increase in the charging current, the  $t_b$  of BS-200 marginally reduced. The calculated effective hydrogen diffusivity values for BS-200 are as follows:  $10 \text{ mA/cm}^2 = 6.26 \times 10^{-8} \text{ cm}^2/\text{s}$ ,  $20 \text{ mA/cm}^2 = 6.41 \times 10^{-8} \text{ cm}^2/\text{s}$  and  $30 \text{ mA/cm}^2 = 8.38 \times 10^{-8} \text{ cm}^2/\text{s}$ . The effective hydrogen diffusivity increased only marginally at  $20 \text{ mA/cm}^2$ , but the increase was significant at  $30 \text{ mA/cm}^2$ . However, it should be noted that the effective hydrogen diffusivity for BS-200 even at a high current density ( $30 \text{ mA/cm}^2 = 8.38 \times 10^{-8} \text{ cm}^2/\text{s}$ ) was significantly lower than that of mild steel at a low current density ( $2 \text{ mA/cm}^2 = 1.82 \times 10^{-6} \text{ cm}^2/\text{s}$ ) (section 4.1.3).

The  $I_p$  value of BS-350 at  $10 \text{ mA/cm}^2$  was  $1 \times 10^{-5} \text{ A/cm}^2$ , which is lower than that of mild steel, but higher than BS-200. With the increase in the charging current, the  $I_p$  values also increased, as was observed for BS-200. The  $t_b$  values of BS-350 were significantly lower than that of BS-200, whereas the difference between BS-350 and mild steel decreased with the increase in the charging current. The calculated effective hydrogen diffusivity values are as follows:  $10 \text{ mA/cm}^2 = 1.09 \times 10^{-6} \text{ cm}^2/\text{s}$ ,  $20 \text{ mA/cm}^2 = 1.63 \times 10^{-6} \text{ cm}^2/\text{s}$  and  $30 \text{ mA/cm}^2 = 2.72 \times 10^{-6} \text{ cm}^2/\text{s}$ . The effective hydrogen diffusivity values of

BS-350 were more than one-order of magnitude higher than those of BS-200. Overall, the increase in the cathodic hydrogen-charging current density had an effect on the hydrogen diffusivity in the nanostructured bainitic steels and mild steel. Generally, high cathodic charging current is expected to generate more hydrogen and make it available for diffusion through the material. The normalised percentage increase in hydrogen diffusivity for the steels relative to that obtained at a cathodic charging current of 10 mA/cm<sup>2</sup> was calculated and shown in Figure 4.7.

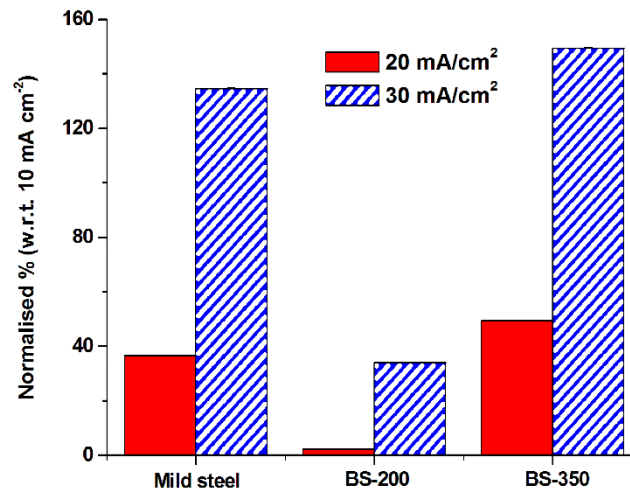


**Figure 4.7 Normalised percentage increase of the hydrogen diffusivity in mild steel, BS-200 and BS-350 nanostructured bainitic steels, normalised against hydrogen diffusion at 10 mA/cm<sup>2</sup>.**

The percentage increase was not significant (~2.4%) ( $p = 0.2$ ) for BS-200 at 20 mA/cm<sup>2</sup>. It was noted that, for BS-200, the hydrogen diffusivity at 30 mA/cm<sup>2</sup> was much lower than that of BS-350 and mild steel, at 2 mA/cm<sup>2</sup> (Kazum et al. 2016). The percentage increase in the diffusivity was highly significant for BS-350: 49 and 150% ( $p < 0.01$ ), and mild steel: 37, and 135% ( $p < 0.01$ ) at 20 and 30 mA/cm<sup>2</sup>, respectively.

Our previous study (section 4.1.3) at a low cathodic hydrogen-charging current density 2 mA/cm<sup>2</sup>, also showed a similar trend to that of the current density at higher cathodic

hydrogen-charging current densities (10, 20 and 30 mA/cm<sup>2</sup>); i.e. BS-200 exhibiting the lowest effective hydrogen diffusivity, followed by BS-350 and mild steel. It was also noted that the effective hydrogen diffusivity for both BS-200 and BS-350 steels increased significantly (20%;  $p < 0.01$ ) when the hydrogen-charging current density increased from 2 to 10 mA/cm<sup>2</sup>. However, the effective hydrogen diffusivity value at 30 mA/cm<sup>2</sup> suggests that BS-200 is highly resistant to hydrogen diffusion even at high cathodic hydrogen charging current density.

The microstructural features of the materials played a significant role in the hydrogen diffusivity behaviour. In our previous study (section 4.1.3), we reported that BS-200 consisted of nano-layers of bainitic ferrite ( $60 \pm 10$  nm thickness) and nano-layers of retained austenite ( $30 \pm 5$  nm thickness), whereas the thickness values of bainitic ferrite and retained austenite thickness were larger for BS-350; i.e. 200-400 nm and  $70 \pm 30$  nm, respectively. Since the BS-200 contains finer grains as compared to that of BS-350, it can be presumed that the austenite/ferrite interfaces per unit volume will be more for BS-200 than in BS-350, which can effectively trap more hydrogen and also reduce the diffusion of more mobile un-trapped hydrogen in BS-200. We previously reported that the volume fraction of the bainitic ferrite was  $79 \pm 2$  and  $47 \pm 2$  % for BS-200 and BS-350 steel, respectively (section 4.1.3). Although the hydrogen diffusivity in the ferrite phase is higher than in the austenite phase (Sakamoto and Katayama 1982) the higher dislocation density in the bainitic ferrite of BS-200 ( $4.7 \times 10^{15} \text{ m}^{-2}$ ) as compared to that in BS-350 ( $2 \times 10^{15} \text{ m}^{-2}$ ) (section 4.1.3), has contributed to the reduced hydrogen diffusivity in BS-200 (which contains 79% bainitic ferrite). It is well documented in the literature that dislocations reduce hydrogen mobility by acting as hydrogen trapping sites (Fielding et al. 2014; Kumnick and Johnson 1980; Pyng and Altstetter 1986; Perng et al. 1989). Hence, the microstructural differences; i.e. grain size, austenite/ferrite interface

and dislocation density, between the BS-200 and BS-350 are presumed to have contributed to the differences in the effective hydrogen diffusivity even at a high cathodic hydrogen-charging current.

### 4.3 Summary

- Hydrogen permeation studies showed that the nanostructured bainitic steels (BS-200 and BS-350) exhibited lower effective hydrogen diffusivity as compared to the mild steel at different cathodic hydrogen-charging current densities (10, 20 and 30 mA/cm<sup>2</sup>).
- BS-200 showed the lowest effective hydrogen diffusivity, followed by BS-350 and mild steel.
- An increase in the cathodic hydrogen-charging current density increased the effective hydrogen diffusivity of all the steels. However, the increase in BS-200 was relatively less as compared to BS-350 and mild steel, which can be attributed to the refined microstructure and the high dislocation density in the ferrite phase.
- Furthermore, the study confirms that BS-200 is highly resistant to hydrogen diffusion in that it exhibits low effective hydrogen diffusivity even at a high cathodic hydrogen-charging current.

## **Chapter 5      Hydrogen Depth Profiling in Nanostructured Bainitic Steel**

### **5.1 Introduction**

The electrochemical hydrogen permeation behaviour of the ultrahigh strength nanostructured bainitic steels suggested that further investigation is required, since the susceptibility to HIC depends mainly on mobility and concentration of hydrogen beyond the subsurface level. (Djukic et al. 2014; Li et al. 2013) reported that the degree of HIC can be evaluated on the basis of decrease in the hardness with distance from the edge of hydrogen induced fracture. Therefore, in this study, the interaction of hydrogen at different depths of the material is deemed essential, in order to evaluate its suitability in an environment of susceptibility. A non-destructible test method using the Vickers microhardness test was carried out on small sized samples of the nanostructured bainitic steel (BS-200, BS-350). Tests were carried out along the cross section of samples charged from one side and the results were compared to those from the uncharged specimens. ERDA hydrogen concentration and depth analysis was also performed to complement the results, and a comparison was also done with mild steel samples.

### **5.2 Microhardness**

The micrographs of the Vickers microhardness indent for the uncharged and H-charged samples are shown in Plate 5.1. Figure 5.1 is the plot of the surface hardness value for the steels recorded on the uncharged and H-charged samples.

For the mild steel, the micrograph of the indent for the charged sample showed a small reduction in the mean value of the diameters or diagonals of indent when compared to the uncharged sample. The values were automatically converted to hardness value by the

tester. Generally, a decrease in mean value of diameters relates to an increase hardness due to the presence of hydrogen in the sample.

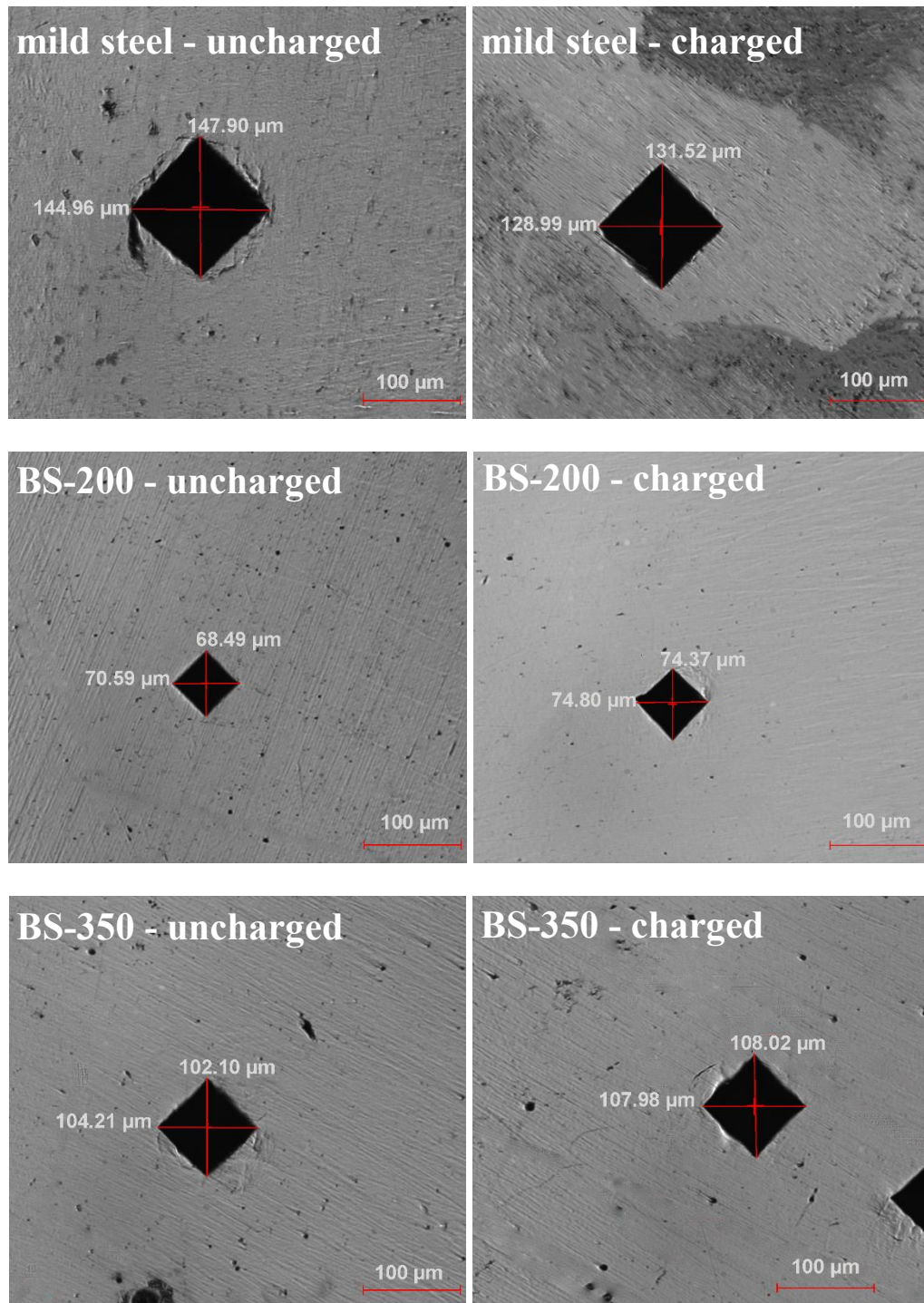


**Plate 5.1 Images of microhardness indent of the steels surface in uncharged and H-charged conditions of mild steel, BS-200 steel and BS3-50 steel.**

The Vickers hardness value was therefore higher by  $\sim 22\%$  in the charged sample, as shown in Figure 5.1. In contrast, the nanostructured bainitic steels exhibited softening by a marginal increment in the diameter of the indent after hydrogen charging.

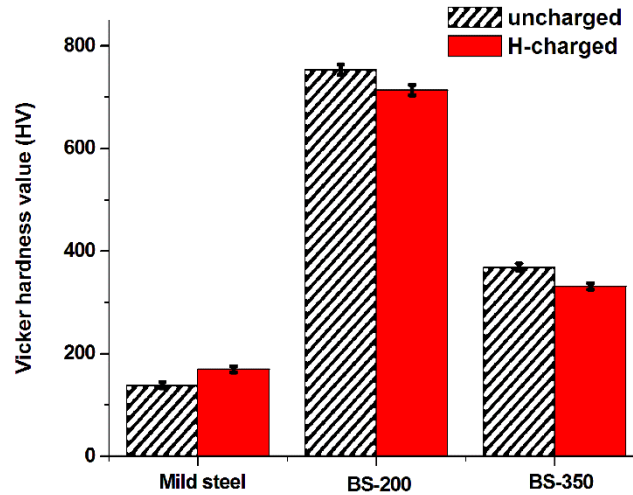


**Figure 5.1 Vickers surface hardness of the steels.**

The BS-200 and BS-350 showed a  $\sim 5\%$  and  $\sim 12\%$  decrease in hardness, respectively. The decrease was higher in BS-350 compared to BS-200, which suggests that the impact of hydrogen was higher in the BS-350 as compared to BS-200.

The hardening and softening effect observed in mild steel and nanostructured bainitic steel is attributed to the presence of hydrogen. It is reported in the literature that a large concentration of dissolved hydrogen in the lattices of iron reduces plasticity (Siddiqui and Abdullah 2005; Asano and Otsuka 1976) and supersaturation can lead to formation of blisters, voids and cracks, which generate stress, and new dislocation that enhances hardening. On the other hand, the interaction of a small amount of hydrogen with dislocation can enhance dislocation mobility and hence softening (Kirchheim 2012; Barnoush et al. 2012). Hence in mild steel, the high concentration of hydrogen in the

lattice of the body centred cubic (BCC) structure can lead to creation of new dislocations which enhances hardness. For the nanostructured bainitic steels, however, the high dislocation density in the bainitic ferrite phase interacted with the hydrogen to enhance local plasticity and hence softening. The softening was observed to be higher in BS-350 than in BS-200, since the high hydrogen concentration at the subsurface of BS-200 resulted in hydrogen atmosphere around the dislocation, which pinned the dislocation and increased the stress required for plastic deformation. This reduced the softening effect (Kirchheim 2012; Barnoush et al. 2012).

### **5.3 Cross-Section Hardness Profile**

The microhardness profile for the uncharged and H-charged steels along the cross-section are shown in Figure 5.2. The H-charged mild steel showed a higher hardness (26%) close to the charged surface ( $\sim 0.2$  mm), as compared to that of the uncharged sample. The hardness value reduced with distance but was still higher than that of the uncharged mild steel. It should be noted that the hardness values for the H-charged mild steel was higher than that of H-uncharged mild steel over the cross-section of the sample. As reported earlier, the nanostructured bainitic steels, on the other hand, exhibited some softening due to H-charging. The H-charged BS-200 showed 707 HV close to the H-charged side ( $\sim 0.2$  mm), whereas the uncharged sample showed 774 HV. Similarly, the H-charged BS-350 exhibited  $\sim 300$  HV close to the H-charged side, and the uncharged showed  $\sim 353$  HV. Comparing the nanostructured bainitic steels, the BS-200 showed a lower drop in hardness value ( $\sim 8\%$ ) near to the charged surface when compared to the drop in BS-350 ( $\sim 14\%$ ). The softening exhibited by BS-200 continued to drop to about 0.6 mm depth of the sample thickness from the charged side. No significant difference in hardness value was recorded after this depth. For the BS-350, however, there was an observed drop across the whole thickness of the sample. This suggests that the effect of hydrogen on



the mechanical property of the steel was more far reaching in BS-350 than in BS-200. Since the microstructure of the BS-200 is more refined as compared to BS-350 and the effective hydrogen diffusivity of hydrogen is lower in BS-200 (section 4.1.3), it is expected that the influence of hydrogen on BS-200 will be limited towards the subsurface of the steel.

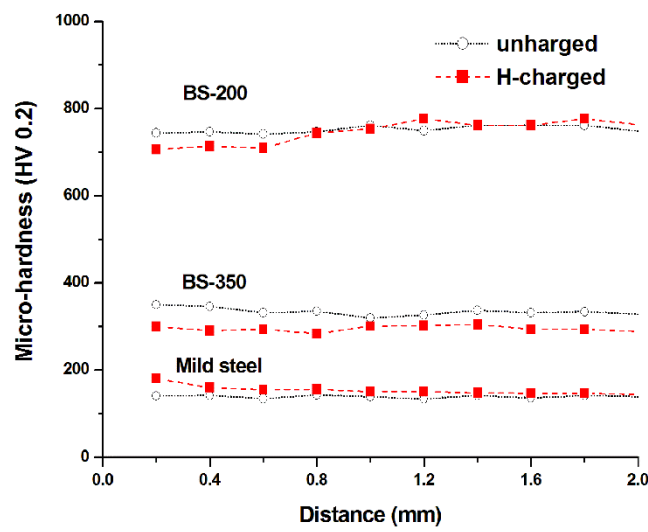


**Figure 5.2 Micro-hardness values for uncharged and H-charged steels taken laterally.**

#### **5.4 Subsurface Hydrogen Concentration by ERDA Analysis**

In order to investigate the subsurface hydrogen concentration, ERDA analysis was carried out. The hydrogen (H) yield against hydrogen depth profiling curve for the samples and the hydrogen concentration in at% are shown in Figure 5.3. All the steel samples showed a high H peak just near the charged surface. For mild steel samples, the average H peak was  $\sim 12$  cts at the subsurface depths of 0 to  $\sim 0.27 \mu\text{m}$ . The BS-350 samples exhibited a concentrated average H peak of  $\sim 13$  cts at up to  $\sim 0.24 \mu\text{m}$  depth, while BS-200 H peak was estimated to 17.5 cts at a smaller depth up to  $0.2 \mu\text{m}$ , given

that both BS-200 and BS-350 nanostructured bainitic steels were charged at 10 mA/cm<sup>2</sup> for 6 hours.

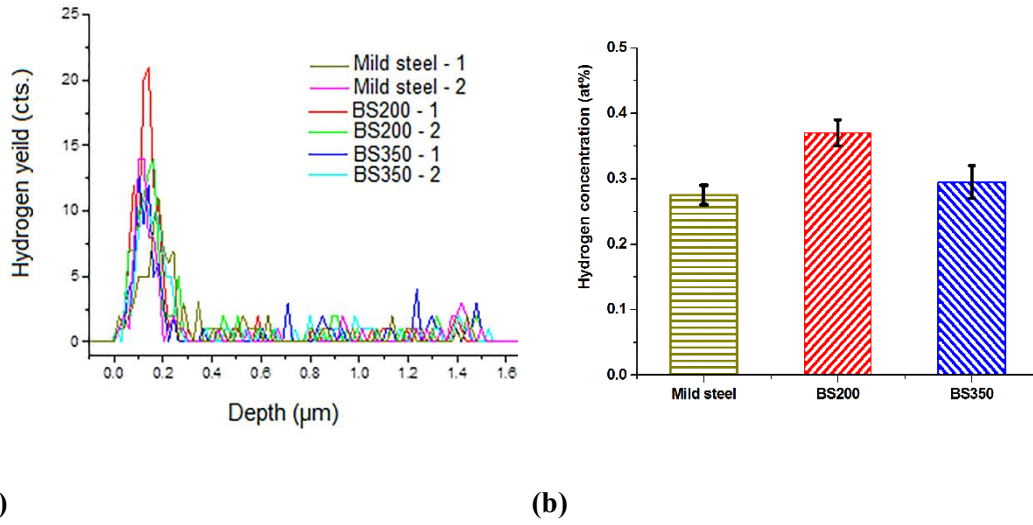


**Figure 5.3 (a) Hydrogen depth profile and (b) hydrogen concentration in at% for the mild steel.**

The observed higher H peak and the short depth in BS-200 suggests that more hydrogen was trapped at the subsurface as compared to BS-350 and mild steel. The hydrogen concentration in BS-200 was ~ 0.37 at% (Figure 5.3b), which was higher than that of BS-350 (~0.2 at %) and mild steel (0.25 at %). We reported earlier that the finer microstructural constituents (bainitic ferrite laths and retained austenite films) and higher dislocation density in the bainitic ferrite phase of BS-200 trapped more hydrogen and was responsible for lower effective diffusivity of the steel as compared to BS-350 and mild steel (section 4.1.3). The higher hydrogen concentration in BS-200 can thus be attributed to high solubility from low hydrogen diffusion in the steel. Based on these observations and the variation in hardness of BS-200 at subsurface, it can be concluded that crack initiation will be limited to the subsurface, and crack prorogation will be lower in the BS-200 compared to both BS-350 and mild steel.

## 5.5 Summary

- Hydrogen depth profiling carried out by ERDA techniques and microhardness testing showed that hydrogen diffused more deeply in mild steel than in BS-200.
- The subsurface hydrogen concentration was higher in BS-200 than in BS-350 and resulted in softening of the steel.
- The microstructure of the steel played a significant role; i.e. the higher dislocation density in the bainitic ferrite can be attributed to localised plasticity and hence softening. The softening was observed to be higher in BS-350 than in BS-200 because the high hydrogen concentration at the subsurface of BS-200 resulted into more dislocation nucleation which reduces the softening effect.
- In contrast mild steel exhibited hardening due to high hydrogen concentration.

## **Chapter 6      Hydrogen Permeation in TWIP Steel**

### **6.1 Introduction**

It is generally believed that high strength steels are more susceptible to HIC (Park et al. 2002). However, the literature clearly suggests that microstructure, rather than strength is the dominant factor in HIC susceptibility (Chang et al. 2001; Park et al. 2008). However, the role of microstructure on HIC is still debatable. For example, reports suggest that microstructures containing higher hydrogen traps are effective in reducing HIC susceptibility because less diffusible hydrogen is available to contribute to the cracking process (Chang et al. 2001; Hardie et al. 2006). Other reports suggest otherwise: that the lower the diffusivity of hydrogen in the microstructure, the higher the solubility, and hence the greater the vulnerability of the steel to HIC (Park et al. 2008; Huang et al. 2010).

High manganese twinning-induced plasticity (TWIP) steels are stable austenitic steels which exhibit a good combination of both high tensile strength (800-1000 MPa) and exceptional elongation (> 50%) (Allain et al. 2004; Grassel et al. 2000). These attractive properties make TWIP steels potential candidates for engineering applications where both high strength and ductility are critical. Often the steels are protected from general forms of corrosion by cathodic protection systems, which may generate high amount of hydrogen that can cause HIC. Given that TWIP steels are austenitic material, they should show very low hydrogen diffusivity at low temperature and hence lower HIC susceptibility. However, reports show that some TWIP steels have shown evidence of HIC susceptibility. Since HIC susceptibility is related to the hydrogen diffusion behaviour in their microstructures (Li et al. 2013; Han et al. 2005), it would be useful to know the hydrogen permeation rate and hydrogen diffusivity in TWIP steels to

understand the HIC mechanism. Hence, in this study, a Devanathan-Stachurski (DS) cell was used to experimentally determine the hydrogen permeation rate and hydrogen diffusivity of TWIP steel at room temperature. The effect of temperature was also investigated and compared with that of mild steel.

## 6.2 Microstructure

The micrographs of the TWIP steel and mild steel are shown in Plate 6.1. The TWIP steel microstructure exhibited fine grains with an average grain size of  $\sim 5 \mu\text{m}$  and a large number of annealing twins. Based on EBSD observation, there is no evidence of any second phase precipitates.

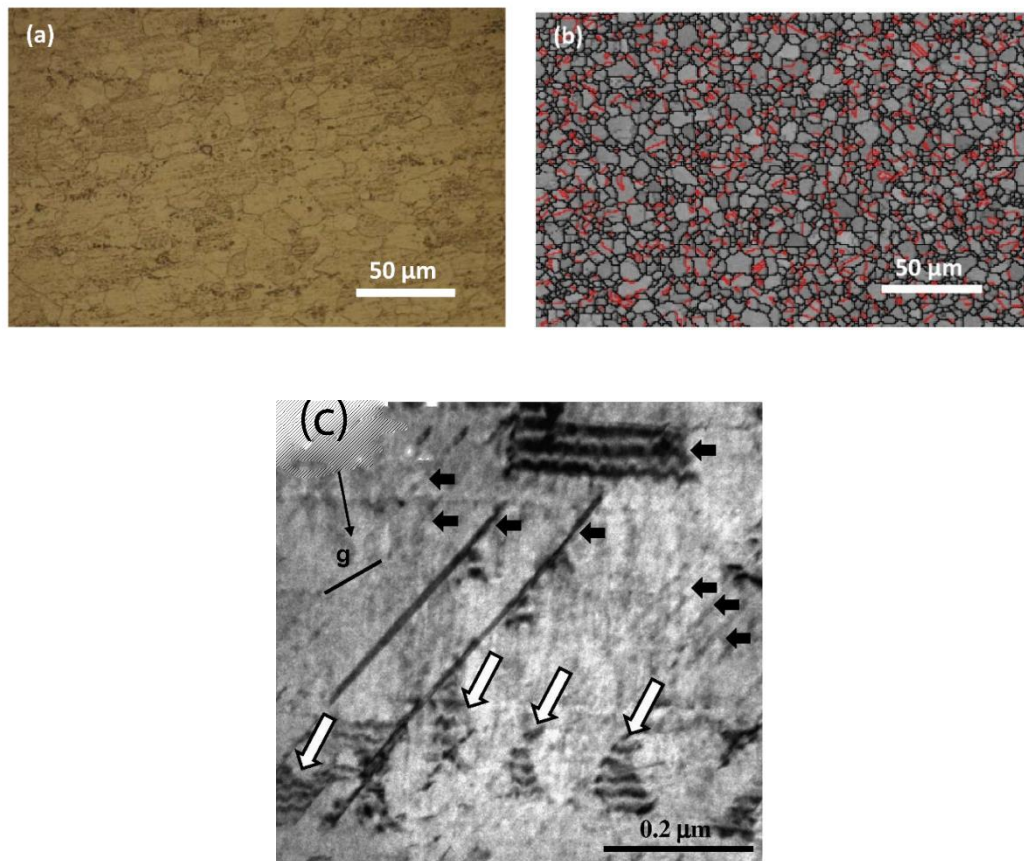


**Plate 6.1 (a) Optical micrograph of mild steel, and (b) EBSD micrograph of TWIP steel and (c) TEM micrograph showing dislocation in white arrows (Beladi et al. 2011). (Note: The black and red lines in (b) represent high angle (>15°) boundary and annealing twin boundaries respectively).**

The dislocation densities by line intersection method could be as high as  $\sim 47.9 \times 10^{13}/\text{m}^2$  after 20 pct strain (Beladi et al. 2011). For the mild steel the grains were coarse and equiaxed with an average grain size of  $\sim 25 \mu\text{m}$ .

### 6.3 Hydrogen Permeation Rate at Room Temperature

The hydrogen permeation curves of the TWIP steel and mild steel obtained under a cathodic current density of  $10 \text{ mA}/\text{cm}^2$  at room temperature ( $25^\circ\text{C}$ ) are shown in Figure 6.1. The corresponding electrochemical permeation parameters are presented in Table 6.1. The permeation curve of the mild steel clearly showed a region of increasing permeation current with time which reached a peak current of  $6.03 \times 10^{-5} \text{ A}/\text{cm}^2$  (chapter 4), taken as the permeation current ( $I_p$ ) (Turnbull 1994; Skellerudsveen et al. 2010).

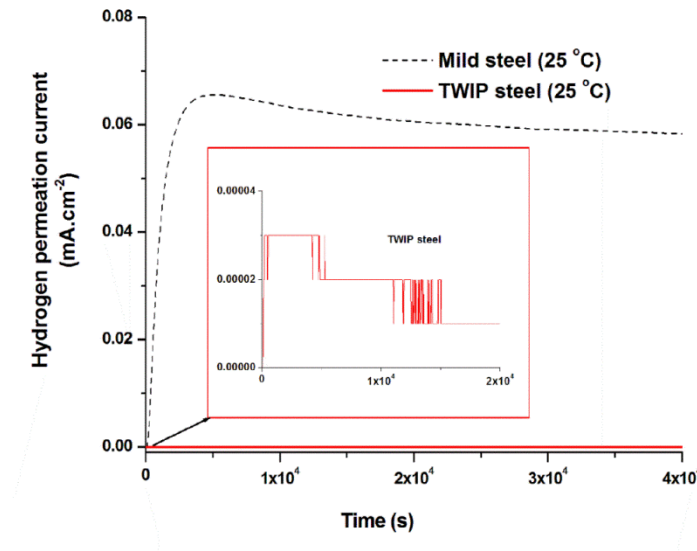


**Figure 6.1** Hydrogen permeation curves for the mild steel and TWIP steel cathodically charged ( $10 \text{ mA}/\text{cm}^2$ ) at room temperature; i.e. ( $25^\circ\text{C}$ ).

Table 6.1 Hydrogen permeation parameters of the mild steel and TWIP steel cathodically charged (10 mA/cm<sup>2</sup>) at 25 °C.

| Material    | $I_p$ (A/cm <sup>2</sup> )   | $Q$ (mol/cm.s)         |
|-------------|------------------------------|------------------------|
| Mild steel* | $6.03 \times 10^{-5}$ (0.35) | $1.56 \times 10^{-15}$ |
| TWIP steel  | $3.00 \times 10^{-8}$ (0.01) | $1.71 \times 10^{-18}$ |

Mean (SD); n = 3. \* chapter 4

The peak current decayed slightly with time. Interestingly, for the TWIP steel, the permeation plot showed no rise in permeation current throughout the charging period (over 1 hour) at room temperature. However, a further investigation of the raw data showed a very small increase in permeation current shortly after the charging. The inset section of the plot showed the small rise. The permeation curve for the TWIP steel was also observed to decay in a similar way as exhibited mild steel. This type of behaviour has been reported in the literature (Turnbull 1994; Park et al. 2008), and can be attributed to the reactions on the steel surface or defective sites, which may be inducing cracks due to high cathodic current density (Park et al. 2008; Beck et al. 1965; Sakamoto and Katayama 1982).

The measured permeation current density ( $I_p$ ) of TWIP steel samples was very low ( $3.00 \times 10^{-8}$  A/cm<sup>2</sup>) as compared to that of mild steel ( $6.03 \times 10^{-5}$  A/cm<sup>2</sup>) (chapter 4). Thus, the permeation rate of TWIP steel ( $1.71 \times 10^{-18}$  mol/cm.s) was also significantly lower as compared to mild steel ( $1.56 \times 10^{-15}$  mol/cm.s). The permeation curve for TWIP steel at room temperature also appeared very discontinuous since it was highly magnified. The mild steel curve was observed to display a similar trend when magnified. This can be due to a small fluctuation in oxidation current logged in by the recorder.

### 6.3.1 Electrolyte temperature on hydrogen permeation rate

Given that diffusion in austenite is very low at room temperature, the effect of temperature increase on the permeation behaviour of the steel was studied. This was done by heating the electrolytes to three different temperatures; i.e. 30 °C, 40 °C and 50 °C.

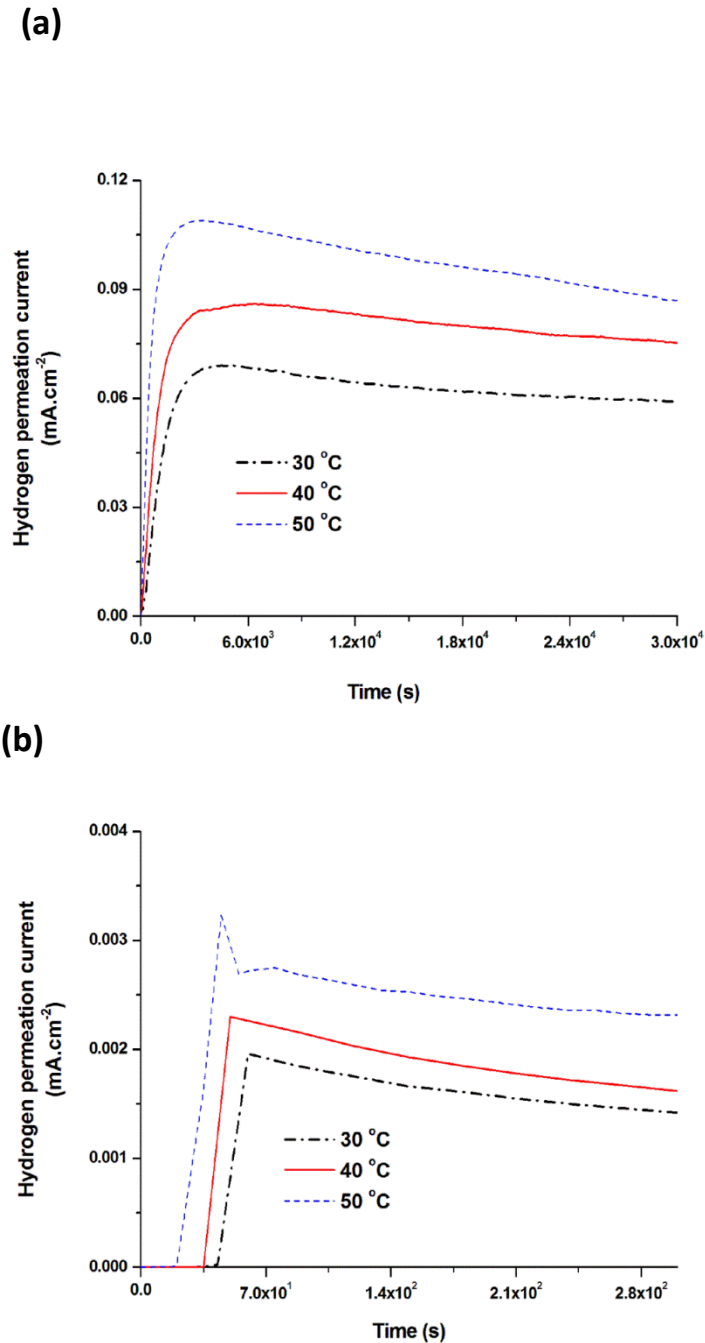


Figure 6.2 Hydrogen permeation curves and peak permeation current for: (a) mild steel, and (b) TWIP steel cathodically charged (10 mA/cm<sup>2</sup>) at different temperatures.



The hydrogen permeation curves for the steels obtained under 10 mA/cm<sup>2</sup> charging current at the different electrolyte temperatures are shown in Figure 6.2.

The corresponding electrochemical permeation parameters are presented in Table 6.2. As expected, the  $I_p$  values of mild steel were generally higher than that of TWIP steel and increased with the increase in the electrolyte temperature. Previously it was reported that the  $I_p$  values of mild steel was  $6.03 \times 10^{-5}$  A/cm<sup>2</sup> at 25 °C (chapter 4) and then  $7.10 \times 10^{-5}$  A/cm<sup>2</sup> at 30 °C;  $8.59 \times 10^{-5}$  A/cm<sup>2</sup> at 40 °C;  $1.90 \times 10^{-4}$  A/cm<sup>2</sup> at 50 °C.

Table 6.2 Permeation parameters of the mild steel and TWIP steel cathodically charged (10 mA/cm<sup>2</sup>) at different temperatures.

| Material   | T °C | $I_p$ (A/cm <sup>2</sup> )   | $Q$ (mol/cm.s)         |
|------------|------|------------------------------|------------------------|
| Mild steel | 30   | $7.10 \times 10^{-5}$ (0.40) | $2.02 \times 10^{-15}$ |
|            | 40   | $8.59 \times 10^{-5}$ (0.20) | $2.51 \times 10^{-15}$ |
|            | 50   | $1.09 \times 10^{-4}$ (0.50) | $3.19 \times 10^{-15}$ |
| TWIP steel | 30   | $1.95 \times 10^{-6}$ (0.02) | $5.55 \times 10^{-17}$ |
|            | 40   | $2.30 \times 10^{-6}$ (0.01) | $6.56 \times 10^{-17}$ |
|            | 50   | $3.10 \times 10^{-6}$ (0.02) | $8.84 \times 10^{-17}$ |

Mean (SD); n = 3

Accordingly, the permeation rate also increased with the increase in the electrolyte temperature:  $2.02 \times 10^{-15}$  mol/cm.s at 30 °C,  $2.51 \times 10^{-15}$  mol/cm.s at 40 °C<sup>1</sup>, and  $3.19 \times 10^{-15}$  mol/cm.s at 50 °C. The increase in permeation current density with a rise in temperature can be attributed to the increased diffusivity at higher temperature. In comparison with the mild steel, the  $I_p$  value for TWIP steel at 30 °C was lower by an order of magnitude ( $1.95 \times 10^{-6}$  A/cm<sup>2</sup>). The  $I_p$  values for TWIP steel increased with further increase in the temperature:  $2.30 \times 10^{-6}$  A/cm<sup>2</sup> at 40 °C and  $3.10 \times 10^{-6}$  A/cm<sup>2</sup> at 50 °C. The calculated permeation rates for TWIP steel were  $5.55 \times 10^{-17}$  mol/cm.s at 30°C,  $6.56 \times 10^{-17}$  mol/cm.s at 40 °C, and  $8.84 \times 10^{-17}$  mol/cm.s at 50 °C. It can also be

observed that the peak of the hydrogen permeation current density was attained faster in TWIP steel than in mild steel. Figure 6.2 shows that at different temperatures it took longer for mild steel to attain a steady state than TWIP steel. This can be due to large path of diffusion through the grain matrix and grain boundary in mild steel, while in TWIP steel it was mainly through the low energy grain boundaries. This suggests that diffusion was higher in TWIP steel than in mild steel, even though the TWIP steel was an austenite steel.

### **6.3.2 Multi-transient permeation curves: irreversible traps analysis**

In order to investigate the effect of any irreversible hydrogen trapping sites in the TWIP steel, hydrogen charging-degassing cycles were performed. During the degassing, background current was allowed to decrease over time to a steady state minimum current to eliminate any weakly trapped hydrogen from the system. This was then followed by recharging. The multi-transient permeation curves of both the TWIP steel and mild steel at 30 °C and 10 mA/cm<sup>2</sup> cathodic charging current are shown in Figure 6.3. The corresponding electrochemical hydrogen permeation parameters are presented in Table 6.3. For the mild steel, the  $I_p$  values marginally decreased for subsequent transients:  $7.10 \times 10^{-5}$  A/cm<sup>2</sup> (Transient I),  $7.04 \times 10^{-5}$  A/cm<sup>2</sup> (Transient II), and  $7.00 \times 10^{-5}$  A/cm<sup>2</sup> (Transient III). The  $I_p$  values of TWIP steel decreased in a similar way to mild steel through the three transients:  $1.95 \times 10^{-6}$  A/cm<sup>2</sup> (Transient I),  $1.84 \times 10^{-6}$  A/cm<sup>2</sup> (Transient II), and  $1.70 \times 10^{-6}$  A/cm<sup>2</sup> (Transient III). Since the permeation curves were not significantly different, it can be suggested that the effect of irreversible traps (such as precipitates or austenite grains) were minimal. Therefore, in TWIP steel, the bulk of diffusion is not through the austenite grain matrix (Turnbull 1994) since during degassing and subsequent transient no significant hydrogen was trapped irreversibly in the austenite grain.

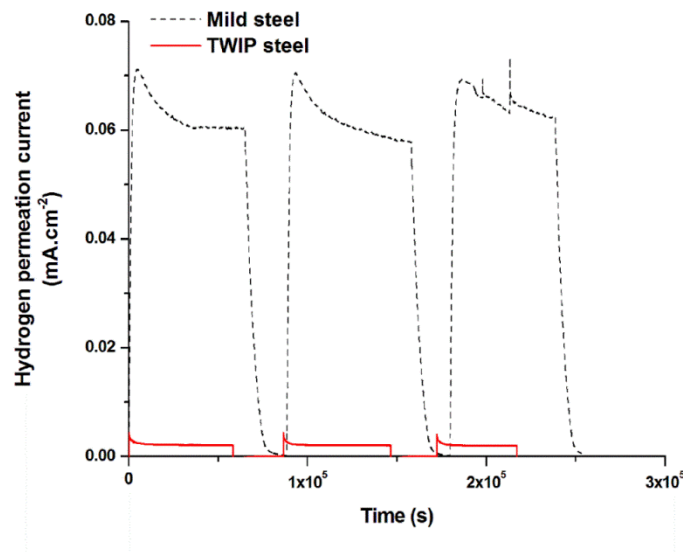


**Figure 6.3 Multiple transients of hydrogen permeation curves for the mild steel and TWIP steel cathodically charged (10 mA/cm<sup>2</sup>) at 30 °C.**

Table 6.3 Permeation current density from the multi-transient curves for the mild steel and TWIP steel cathodically charged (10 mA/cm<sup>2</sup>) at 30 °C.

| Material   | Transient I                  | $I_p$ (A/cm <sup>2</sup> )   |                              |
|------------|------------------------------|------------------------------|------------------------------|
|            |                              | Transient II                 | Transient III                |
| Mild steel | $7.10 \times 10^{-5}$ (0.40) | $7.04 \times 10^{-5}$ (0.20) | $7.00 \times 10^{-5}$ (0.60) |
| TWIP steel | $1.95 \times 10^{-6}$ (0.30) | $1.84 \times 10^{-6}$ (0.20) | $1.70 \times 10^{-6}$ (0.20) |

Mean (SD); n = 3

### 6.3.3 Effective hydrogen diffusivity

The calculated effective hydrogen diffusivity for the steels at different temperatures are presented in Tables 6.4. At room temperature, the  $t_b$  for TWIP steel was ~ 50 s which is lower by about ~64% as compared to  $t_b$  for mild steel (~ 82 s), which suggests that hydrogen was able to diffuse from the cathodic side to the anodic side of TWIP steel quicker than in mild steel.

Table 6.4 Effective hydrogen diffusivity and breakdown time for the mild steel and TWIP steel cathodically charged at different temperatures.

| Material   | $T$ °C | $t_b$ (s) | $D$ ( $\text{cm}^2/\text{s}$ ) | $C$ ( $\text{mol}/\text{cm}^3$ ) |
|------------|--------|-----------|--------------------------------|----------------------------------|
| Mild steel | 25     | 82 (15) * | $1.99 \times 10^{-6}$ (0.30) * | $7.84 \times 10^{-10}$           |
|            | 30     | 65 (5)    | $3.04 \times 10^{-6}$ (0.20)   | $6.64 \times 10^{-10}$           |
|            | 40     | 60 (2)    | $3.30 \times 10^{-6}$ (0.20)   | $7.61 \times 10^{-10}$           |
|            | 50     | 55 (4)    | $3.60 \times 10^{-6}$ (0.20)   | $8.86 \times 10^{-10}$           |
| TWIP steel | 25     | 50 (3)    | $3.95 \times 10^{-6}$ (0.30)   | $4.33 \times 10^{-13}$           |
|            | 30     | 45 (7)    | $4.39 \times 10^{-6}$ (0.30)   | $1.26 \times 10^{-11}$           |
|            | 40     | 30 (5)    | $6.59 \times 10^{-6}$ (0.40)   | $9.95 \times 10^{-12}$           |
|            | 50     | 25 (5)    | $7.91 \times 10^{-6}$ (0.30)   | $1.12 \times 10^{-11}$           |

Mean (SD); n = 3, \* (chapter 4)

The effective diffusivity values of the steels at room temperature; i.e. 25 °C, were as follows:  $3.95 \times 10^{-6} \text{ cm}^2/\text{s}$  (TWIP steel) and  $1.99 \times 10^{-6} \text{ cm}^2/\text{s}$  (chapter 4) (mild steel). The  $t_b$  values decreased with increasing temperature for both steels. The  $t_b$  value for TWIP steel decreased to 45 s, 30 s and 25 s as the electrolyte temperature was increased to 30 °C, 40 °C and 50 °C, respectively. Hence, the calculated effective diffusivity values for TWIP steel were  $4.39 \times 10^{-6} \text{ cm}^2/\text{s}$  at 30 °C,  $6.59 \times 10^{-6} \text{ cm}^2/\text{s}$  at 40 °C, and  $7.91 \times 10^{-6} \text{ cm}^2/\text{s}$  at 50 °C. However, for the mild steel,  $t_b$  was higher than that of TWIP steel at all the temperatures: 65 s at 30 °C, 60 s at 40 °C, 55 s at 50 °C. Thus, the calculated effective hydrogen diffusivity values for mild steel:  $3.04 \times 10^{-6} \text{ cm}^2/\text{s}$  at 30 °C,  $3.30 \times 10^{-6} \text{ cm}^2/\text{s}$  at 40 °C and  $3.60 \times 10^{-6} \text{ cm}^2/\text{s}$  at 50 °C were lower than that of the TWIP steel. The hydrogen solubility in the TWIP steel was about two orders of magnitude lower as compared to that of mild steel at room temperature. However, as the temperature was increased there was a small reduction and a then slight increase in the solubility for each of the steel. However, generally the solubility was lower in TWIP steel since the diffusion was higher.

## 6.4 Discussion

The hydrogen permeation rate for the mild steel and TWIP steel cathodically charged at different temperatures is presented in Figure 6.4. The experimental results clearly showed that the hydrogen permeation rate of the TWIP steel was lower than the mild steel. At room temperature, the hydrogen permeation rate of the TWIP steel was three orders of magnitude lower than the mild steel. As the electrolyte temperature increased to 30 °C, there was a significant increase in the TWIP steel permeation rate. However, further increases in temperature to 40 °C and 50° C showed only smaller increase in the permeation rate.

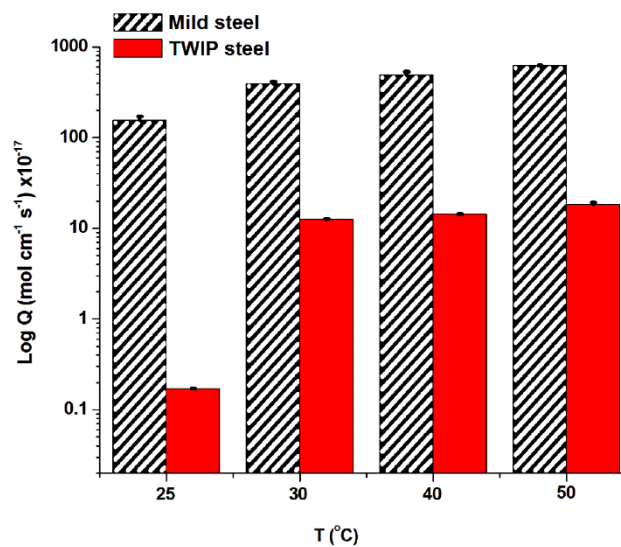


**Figure 6.4** Hydrogen permeation rate of the mild steel and TWIP steel cathodically charged (10 mA/cm<sup>2</sup>) at different temperatures.

Given that hydrogen diffusion in austenite structure at room temperature is known to be very low, the increase at higher temperature can be attributed to the combination of increased activation energy available for hydrogen diffusion and the possible differential thermal expansion in the path of hydrogen travel in the grain boundary and crystal structure of the austenite phase.

Generally, a substantial decrease in the  $I_p$  values on subsequent hydrogen charging-degassing cycles indicates the presence of irreversible hydrogen trapping sites in the material (Turnbull 1994; Skjellerudsveen et al. 2010). In the current study, the  $I_p$  values for the TWIP steel did not change significantly over the charging-degassing cycles, thus suggesting that no considerable irreversible hydrogen traps were involved in the system; i.e. irreversible traps such as the austenite grain or grain boundary precipitates did not adversely affect the path through which diffusion occurred. It should be noted also that TWIP steel is a stable austenite and there is no evidence of precipitate formation in the steel. On the 3<sup>rd</sup> transient for mild steel, the permeation current was observed to fluctuate, which has been attributed to the material cracking during the hydrogen permeation process. In fact, it has been reported that internal cracks became apparent in the ferrite phase when a duplex stainless steel (containing ferrite and austenite phase) was subjected to cathodic charging (Luu et al. 2002). However, the absence of such current fluctuations in TWIP steel confirms its high resistance to HIC by soluble hydrogen. Interestingly, the hydrogen diffusivity in the TWIP steel was higher than in the mild steel. As the temperature of the electrolytes was increased, the hydrogen diffusivity increased for both TWIP and mild steels. It was also reported in the literature that an increase in hydrogen diffusivity occurred with an increase in temperature for pure iron and steels (Han et al. 2015; Addach et al. 2005; Padhy et al. 2015). In order to elucidate the hydrogen permeation mechanism in the TWIP steel, the temperature dependence of hydrogen diffusivity was plotted using the Arrhenius relationship:

$$D = D_o \exp(-E/RT) \quad (6.1)$$

where  $D_o$  is the temperature-independent constant,  $E$  is (J/mol) the activation energy for diffusion,  $R$  (J/mol.K) is the gas constant and  $T$  (K) is the temperature. Figure 6.5 shows

that the effective hydrogen diffusivity values in both the steels follow the Arrhenius relationship over the test temperature range.

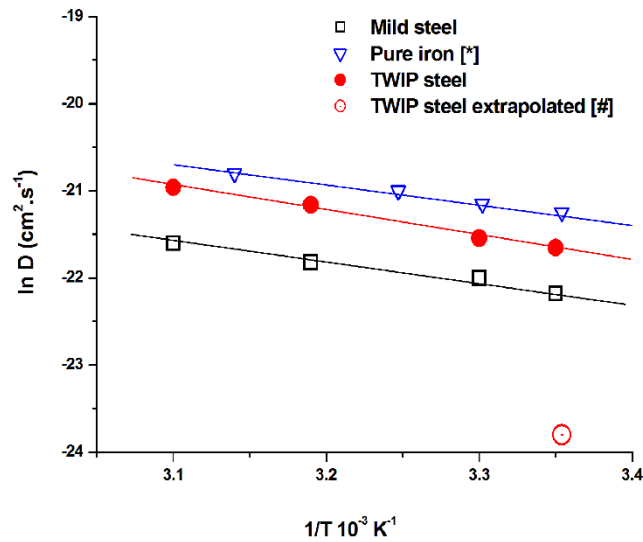


**Figure 6.5 Arrhenius plot of the effective hydrogen diffusivity of mild steel compared with the literature values.**

(Note: \* = Addach et al. 2005, # = Han et al. 2015).

For the purpose of comparison, the hydrogen diffusivity at (25 °C) values of pure iron ( $5.8 \times 10^{-6} \text{ cm}^2/\text{s}$ ) (Luu et al. 2002) and TWIP steel ( $4.62 \times 10^{-11} \text{ cm}^2/\text{s}$ ) (Han et al. 2015) obtained from the literature were also included in Figure 6.5. Interestingly, the hydrogen diffusivity of the TWIP steel reported by Han et al. 2015 was five orders of magnitude lower than the value obtained in this study ( $3.95 \times 10^{-6} \text{ cm}^2/\text{s}$ ). It must be noted that the value reported was an extrapolation from high temperature values. Further, the difference in hydrogen diffusivity values at low temperature can be attributed to variations in experimental conditions; i.e. low pressure hydrogen gas was used by Han et al. 2015, whereas in this study the electrochemical charging provided high concentrations of hydrogen for diffusion.

The calculated activation energy for hydrogen diffusion was marginally lower in the TWIP (19.20 kJ/mol) steel than in the mild steel (21.40 kJ/mol). These values are in the range reported for low energy-barrier sites such as grain boundaries (18 - 20 kJ/mol) (Koyama et al. 2014). For ferrite and austenite grains, the reported activation energy values were 21-27 kJ/mol (Takai et al. 2003) and 49 - 58 kJ/mol (Ningshen et al. 2001), respectively. It is clear from the activation energy values that austenite grains are high energy-barrier sites, whereas the grain boundaries and ferrite grains are low energy-barrier sites. Thus, it can be suggested that the hydrogen diffusion path in the TWIP steel was primarily through the low energy-barrier grain boundaries. It has been reported that austenite steel exhibits lower hydrogen effective diffusivity when compared to ferritic steel (Ronevich et al. 2010; Luppó et al. 1999). The penetration depth of hydrogen in austenite steel at ambient temperature was reported to be limited to near-surface grains (Bai et al. 2016; Han et al. 2014); i.e.  $\sim 3 \mu\text{m}$  in depth after 1 h charging with  $10 \text{ mA/cm}^2$ . Accordingly, in this study (TWIP steel grain size  $\sim 5 \mu\text{m}$ ), the hydrogen should have been locked up in the surface grains if the hydrogen diffusion is mainly through the austenite grains. In contrast, the  $t_b$  was only 50 s for the 0.5 mm thick TWIP steel sheet. Hence, the hydrogen diffusion can be said to be mainly through the grain boundaries. In fact, reports in the literature indicate that, in austenite steel, hydrogen-assisted cracking was observed mainly along the grain boundaries (Koyama et al. 2014).

For the mild steel, the ferrite grains and grain boundaries act as pathways for hydrogen diffusion and result in a higher permeation rate and a longer breakthrough time ( $t_b$ ), and also a longer time to reach the peak current as compared to that of the TWIP steel. It has been reported that the grains and grain boundaries are the path for hydrogen diffusion in the ferrite microstructure (Luu and Wu 1996; Arafin and Szpunar 2011). A schematic



model illustrating the hydrogen permeation pathways in TWIP steel and mild steel are shown in Figure 6.6.

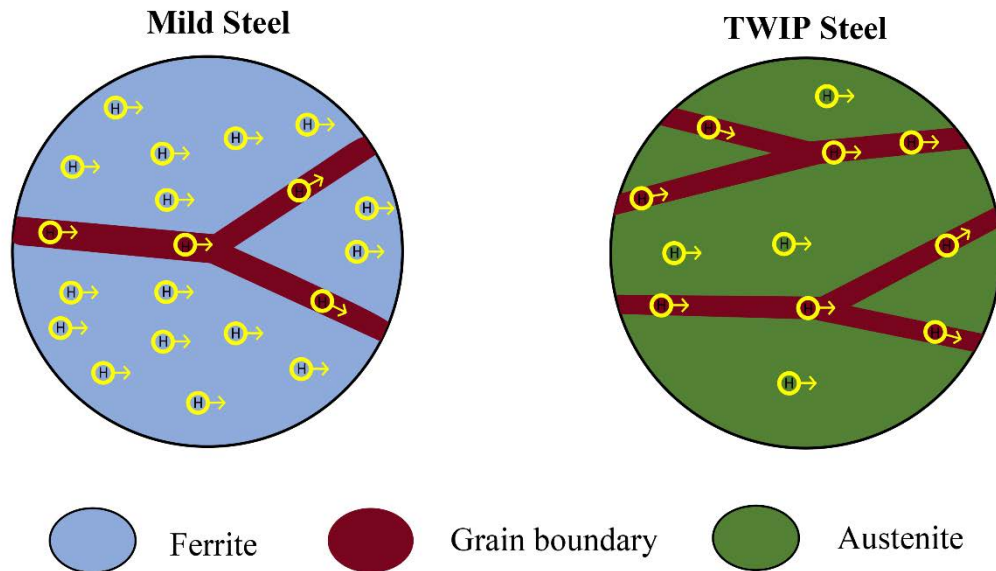


**Figure 6.6 Schematic diagram illustrating hydrogen permeation in mild steel and TWIP steel.**

The hydrogen permeation in the TWIP steel was predominantly through the grain boundaries, whereas in the mild steel it occurred through both the ferrite grains and grain boundaries. Based on the electrochemical hydrogen permeation studies, the hydrogen permeability rate for the TWIP steel was significantly lower than that of mild steel at room temperature; i.e. 25 °C. Increasing the electrolyte temperature increased the hydrogen permeation rate for the TWIP steel.

However, the permeation rate of TWIP steel even at 50 °C was lower than the mild steel at room temperature. Multi-transient permeation curves revealed that there were no significant irreversible hydrogen traps in the TWIP steel. The effective hydrogen diffusivity was, however, higher in the TWIP steel than in the mild steel at all the four test temperatures. Given that no evidence of precipitates was observed along grain

boundaries of the TWIP steel, no strong irreversible hydrogen traps were found. Due to the similarity in the multiple transient curves and the higher rate of diffusion, it can be suggested that the path of hydrogen diffusion in the TWIP steel occurred primarily through the low energy-barrier grain boundaries. Based on the high hydrogen diffusivity of TWIP steel, it can be concluded that the steel will be prone to HIC in tensile load due to the increased mobility of hydrogen to probable crack sites. The steel will be more prone to intergranular fracture along the path of diffusion. However, if the steel is not under any form of load, the low hydrogen solubility or concentration may not be high enough to initiate HIC. Hence, a tensile test of the steel in a hydrogen pre-charged condition will probably not show significant HIC due to the low concentration, but in a continuous or in-situ charging condition, the results may differ. Therefore, further testing is being designed to evaluate HIC susceptibility in those loading conditions.

## **Chapter 7      Hydrogen Induced Cracking (HIC) in TWIP Steel**

### **7.1 Introduction**

The data on hydrogen diffusivity on TWIP steel from the previous chapter is not sufficient to accurately determine the HIC susceptibility of steel. Since high hydrogen diffusivity and solubility are related and are known to enhance HIC, further tests are required to evaluate the effect of hydrogen solubility or concentration on the mechanical properties of tensile samples. It can be suggested that pre-charged tensile samples that exhibit HIC fail only due to the hydrogen that has become trapped and dissolved in the microstructure. On the other hand, in-situ charged samples will show a reduction in mechanical properties, primarily due to trapped or increased mobile hydrogen towards the tips of cracks in crack propagation. Hence in this chapter, tests were performed on pre-charged and in-situ charged tensile samples using a slow strain rate method at different temperatures (25, 30, 40 and 50 °C). Results were compared to the data generated from an uncharged sample. Mild steel was also tested to provide a comparison between ferrite and austenite TWIP steels.

### **7.2 Tensile Properties of Pre-charged Samples**

The stress-strain curves and plot of the mild steel samples tested at the strain rate of  $2 \times 10^{-4}$  /s in the uncharged and hydrogen pre-charged conditions at different temperatures are presented in Figures 7.1 a and b. The ultimate tensile strength (UTS) for the uncharged mild steel was ~346 MPa. The UTS for the mild steel marginally increased as the charging temperature was increased from room temperature: 25 °C = ~359 MPa, 30 °C = ~352 MPa and 50 °C = ~351 MPa.

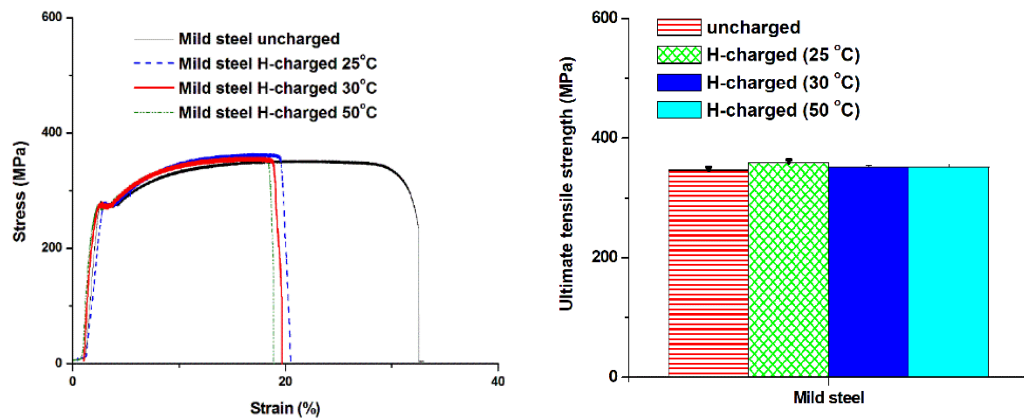


**Figure 7.1 Stress-strain plots of mild steel samples in uncharged and H-charged conditions.**

A similar trend has been observed when the charging time was increased for low carbon steel (Chin et al. 2011), which may be related to increased hydrogen concentration. The H-charged mild steel sample showed a significant loss in ductility as compared to the uncharged sample. Compared to the original specimen, the fractured uncharged mild steel exhibited strain to failure,  $\epsilon_f$ , of 33% (Figure 7.2).

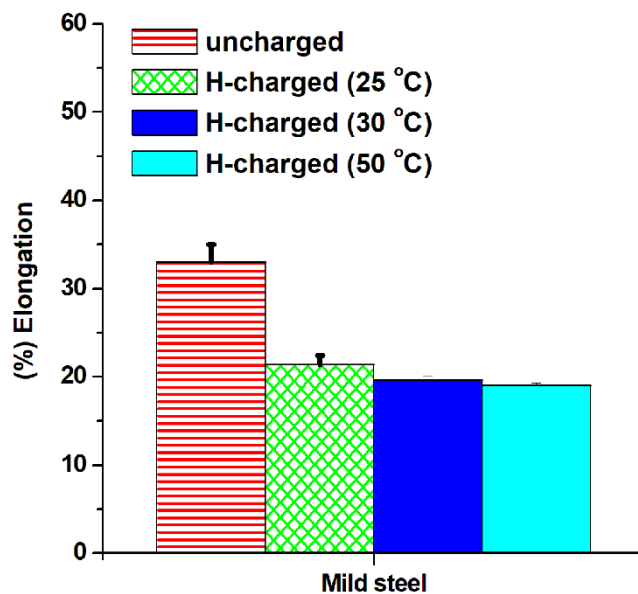


**Figure 7.2 % elongation of mild steel samples plotted in bar charts.**

For the H-charged mild steel at 25 °C, the sample exhibited lower elongation: ~21%  $\epsilon_f$  compared to the uncharged sample (33%). Interestingly, subsequent hydrogen charging at higher temperature also show a significant loss in the mechanical properties of charged samples compared to uncharged sample, but in between the temperatures, the properties were only marginally different. This suggests that for mild steel, the charged samples were fully affected under the experimental condition regardless of an increase in temperature.

In comparison to mild steel, the uncharged TWIP steel sample exhibited about 3-fold higher UTS; i.e. ~1029 MPa and a significantly higher  $\epsilon_f$  (~54%) than mild steel (Figure 7.3).

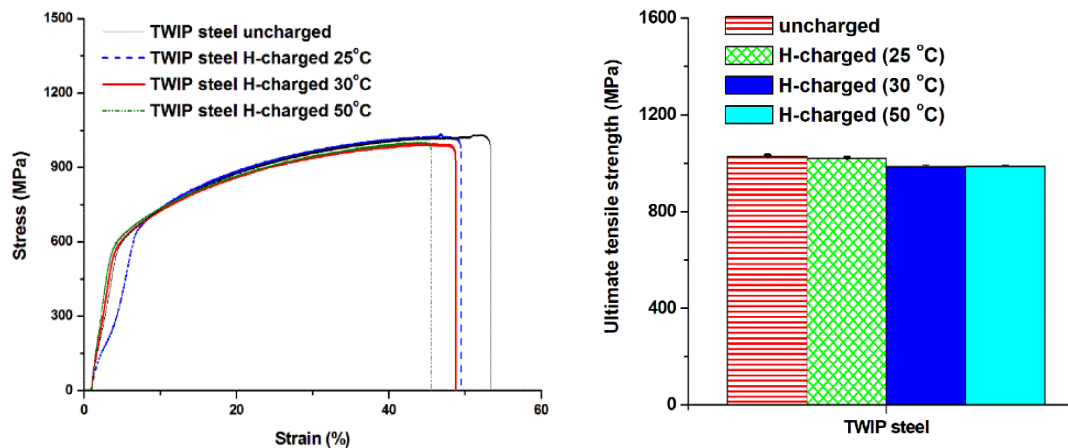


**Figure 7.3 Stress-strain plots of TWIP steel samples in uncharged and H-charged conditions.**

The H-charged TWIP steel samples also generally showed higher mechanical properties as compared to mild steel under similar test conditions. In contrast to mild steel, the UTS for H-charged TWIP steel decreased marginally as the temperature of the charging electrolyte was increased. It decreased from ~1029 MPa by about 0.9% at room temperature (25 °C). A further decrease was observed at higher temperature: ~ 4.3% as the temperature was increased through to 50 °C. Small variations in yield strength by

hydrogen in austenitic stainless steel are a common occurrence (Park et al. 2015). The H-charged TWIP steel at 25 °C exhibited ~49%  $\epsilon_f$ , which marginally decreased with the increase in charging temperature. The values of  $\epsilon_f$  for the H-charged TWIP steel above room temperature are as follows: 30 °C = ~ 48%, and 50 °C = 47% respectively. In general, there was no significant loss in ductility for the H-charged TWIP steel as compared to the uncharged TWIP steel.

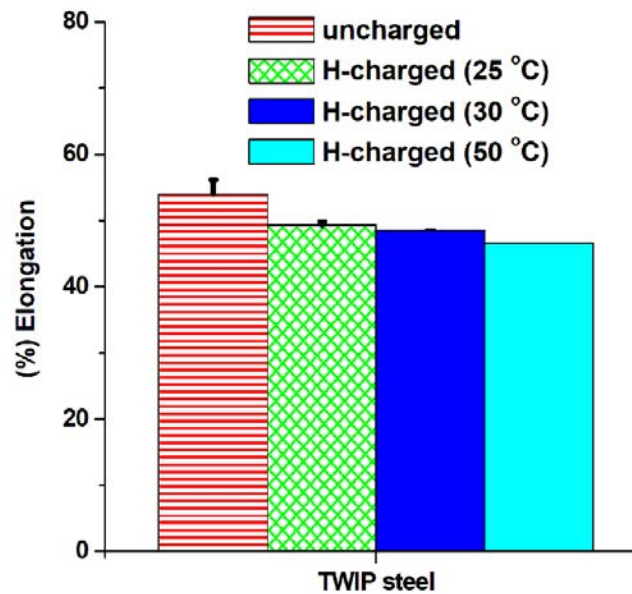


**Figure 7.4** Elongation of TWIP steel samples plotted in bar charts.

The  $\epsilon_f$  was 47% for TWIP steel and was much higher when compared to that of mild steel (19%) at 50 °C. This suggested that TWIP steel has not lost its ductility and hence is less prone to HIC when compared to mild steel. This result can be attributed to low hydrogen solubility in TWIP steel in the pre-charged condition.

### 7.3 Macrographs of Fractured Samples

The macrographs of the fractured mild steel and TWIP steel samples under the uncharged and H-charged conditions are as shown Plate 7.1. The uncharged mild steel sample exhibited a large %RA (reduction in area) compared to the H-charged samples. The

fractured surface of uncharged mild steel exhibited a %RA = ~54% when compared to the original sample (Figure 7.5).

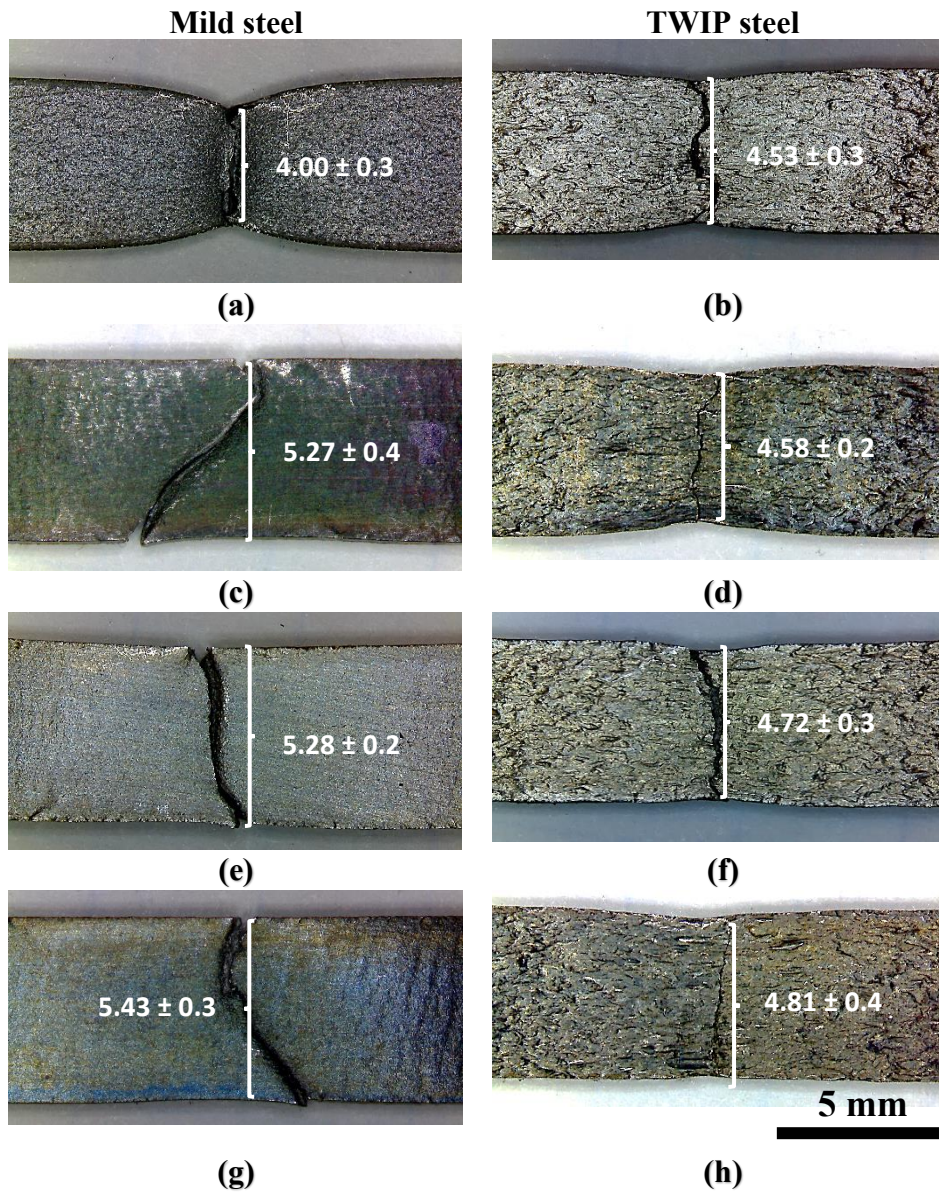


**Plate 7.1** Macrographs of the fractured tensile specimens uncharged (a, b), H-charged 25° C (c, d), H-charged 30° C (e, f) and H-charged 50° C (g, h).



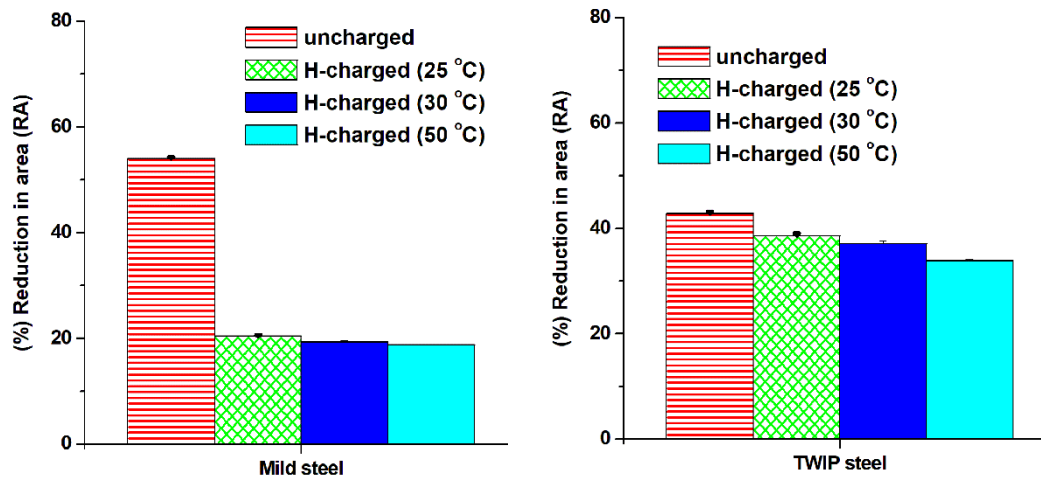


**Figure 7.5 % reduction in area (RA) of the samples plotted in bar charts.**

Subsequent increase in temperature and resulting increase in hydrogen concentration in the material lead to a reduction in RA and hence susceptibility of the steel to HIC. Since there was a decrease in the ductility as a result of lower values of RA for subsequent higher temperature of H-charged steels compared to the uncharged sample, it can be suggested that some form of HIC was occurring. In TWIP steel the %RA was not significant. Hence, the decrease in the mechanical properties was more substantial in mild steel compared to TWIP steel for each corresponding temperature. The influence of hydrogen on mild steel can therefore be said to be more significant when compared to that of TWIP steel.

## 7.4 Fractography

Typical fracture surfaces of the mild steel in the uncharged and H-charged condition are shown in the SEM images (Plate 7.2). Corresponding fracture surfaces at the edge and central regions are presented. The fractured surface at the edge and centre of the uncharged mild steel revealed a relatively uniform distribution of spherical dimple features and micro-voids, which is a well-known characteristic of ductile fracture.



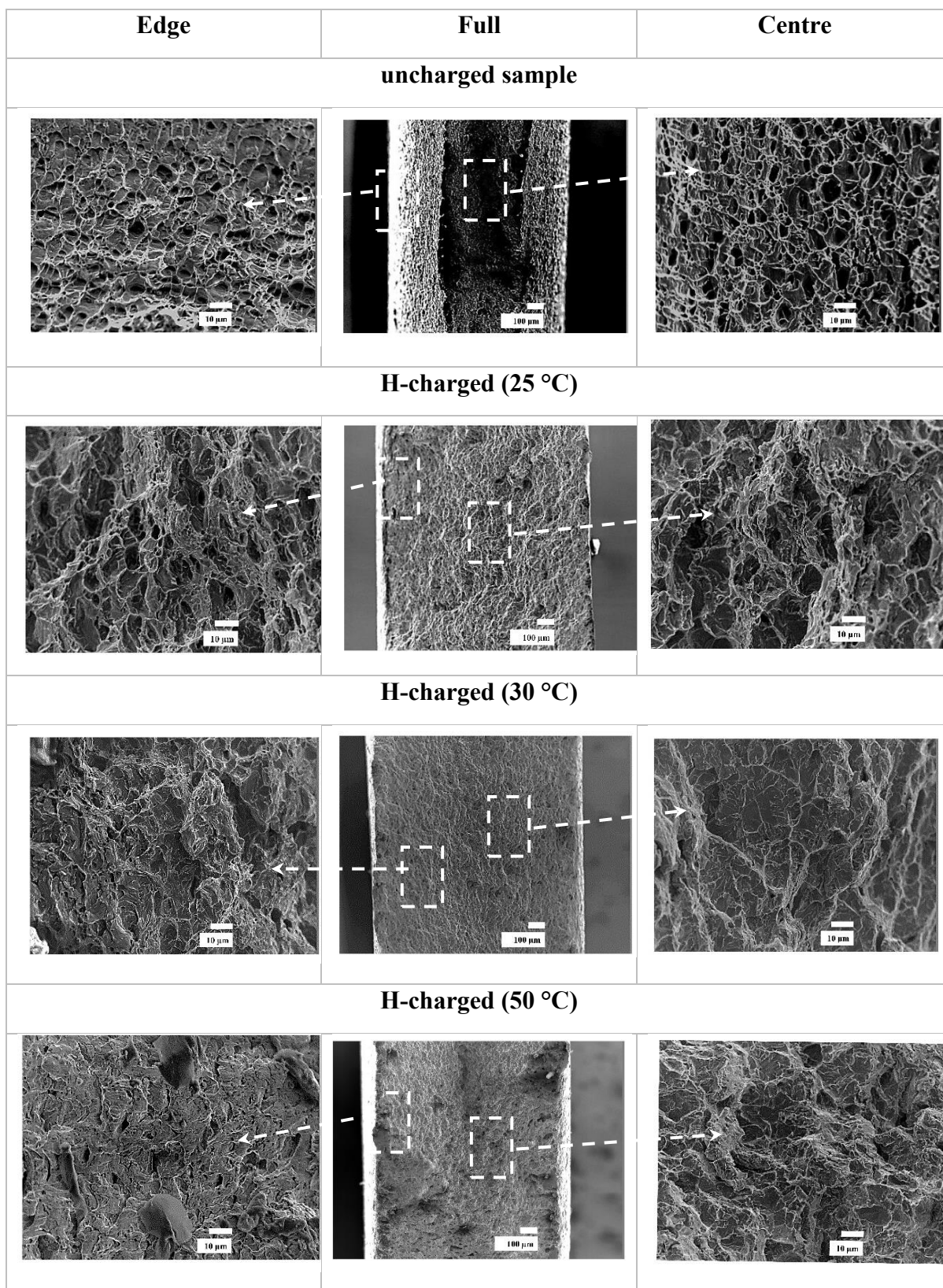


**Plate 7.2 Fractured surfaces of mild steel showing the edge, full and centre section: uncharged, H-charged 25 °C, H-charged 30 °C and H-charged 50 °C.**

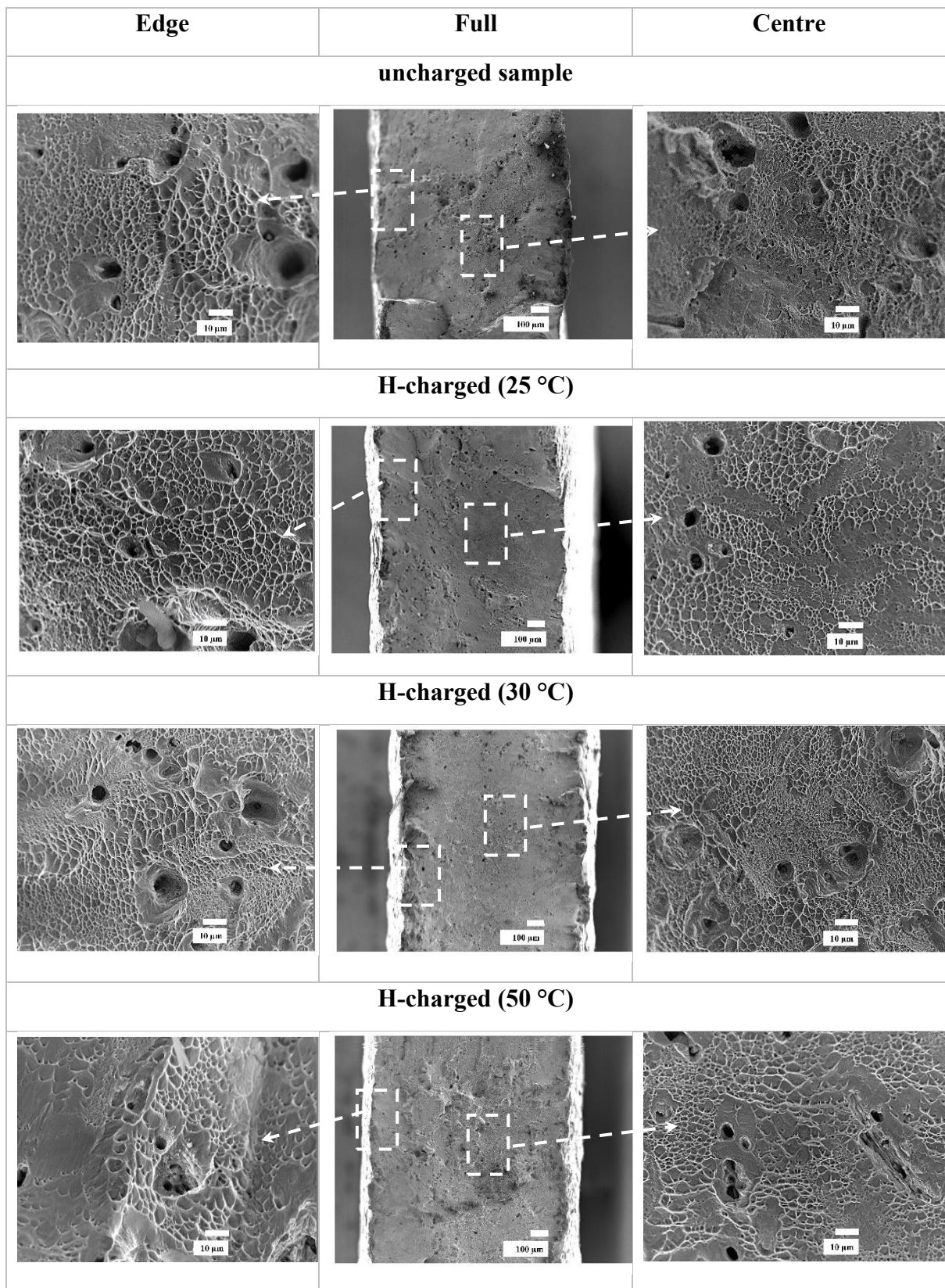


**Plate 7.3 Fractured surfaces of TWIP steel showing the edge, full and centre section: uncharged, H-charged 25 °C, H-charged 30 °C and H-charged 50 °C.**

Fracture surfaces for TWIP steel in an uncharged condition, as shown in Plate 7.3 (edge and centre) of the sample, revealed a series of ductile features, showing a relatively uniform distribution of very fine dimples and several visible micro-voids, which are also consistent with ductile failures. However, a noticeable difference was observed with the H-charged samples. The sample tested as H-charged (25 °C) mild steel showed a brittle failure revealed by transgranular cracking characterised by cleavage steps, river patterns and feather markings. The intergranular features were prior sites where hydrogen became trapped along the grain boundaries. The dimples appear fewer and isolated, with a range of sizes. In addition, the fractured surface appeared with multiple cracks which could have been intensified by the hydrogen interaction with the sample. For the H-charged sample at a higher temperature, the dimples progressively became fewer in number. At 50 °C, the dimples completely disappeared, and the fracture surface showed a typical hydrogen induced brittle feature. The fracture surfaces of the steel in the central region showed a similar feature for each of the tested samples. This suggested that, for the H-charged samples, hydrogen interacted with the sample throughout: at the edge and in the central region. Also, as temperature of the charging electrolyte increased the features of embrittlement became more prominent.

Fracture surfaces at the edge and centre section of TWIP steel in H-charged conditions showed a similar series of relatively uniform distribution of very fine dimples at the lower temperature. As the temperature increased and hydrogen concentration increased, the edge section exhibited fewer and coarser dimples for TWIP steel H-charged at 50 °C.

A number of visible micro-voids are still revealed on H-charged samples, which are characteristics of ductile fracture. No occurrences of intergranular or mixed mode of intergranular and transgranular cracking consistent with brittle fracture were observed.

Thus, the effect of hydrogen on TWIP steel was again minimal as compared to mild steel in this condition. It can be said that the low solubility of hydrogen in the pre-charged condition of TWIP steel did not encourage HIC. This can be attributed to the higher rate of diffusion in TWIP steel as compared to mild steel, which experienced HIC due to low diffusion and consequent high solubility.

## 7.5 HIC Susceptibility of Pre-charged Samples

In order to quantify the HIC susceptibility of the steels, the hydrogen induce cracking indices ( $I_{HIC}$ ) were calculated based on the ratio of the mechanical properties (such as elongation and reduction in area) measured in H-charged to its corresponding measurement in uncharged condition. A low  $I_{HIC}$  suggest a high HE susceptibility and  $I_{HIC}$  value close to unity, means no significant effect due to H-charging. The calculated values of  $I_{HIC}$  for the steels are presented in Table 7.1 and Figure 7.6. The mild steel showed higher HIC susceptibility in each of the charging conditions than the TWIP steel. For the mild steel under H-charged conditions at room temperature, the  $I_{HIC}$  was found to be 0.59 with respect to % elongation. A further increase in temperature significantly affected the  $I_{HIC}$  ( $p < 0.01$ ), as temperature increased between 25 to 30 °C, and 25 to 50 °C respectively. The  $I_{HIC}$  with respect to % reduction in area showed a similar trend, with mild steel sample showing 0.38, 0.35 and 0.34 indices for 25, 30 and 50 °C respectively.

Table 7.1 The  $I_{HE}$  susceptibility indices for mild steel and TWIP steel

| Temperature (°C) | $\mathcal{E}_f$ | $RA$ | $\mathcal{E}_f$ | $RA$ |
|------------------|-----------------|------|-----------------|------|
| 25               | 0.59            | 0.38 | 0.95            | 0.90 |
| 30               | 0.59            | 0.35 | 0.93            | 0.87 |
| 50               | 0.57            | 0.34 | 0.84            | 0.79 |



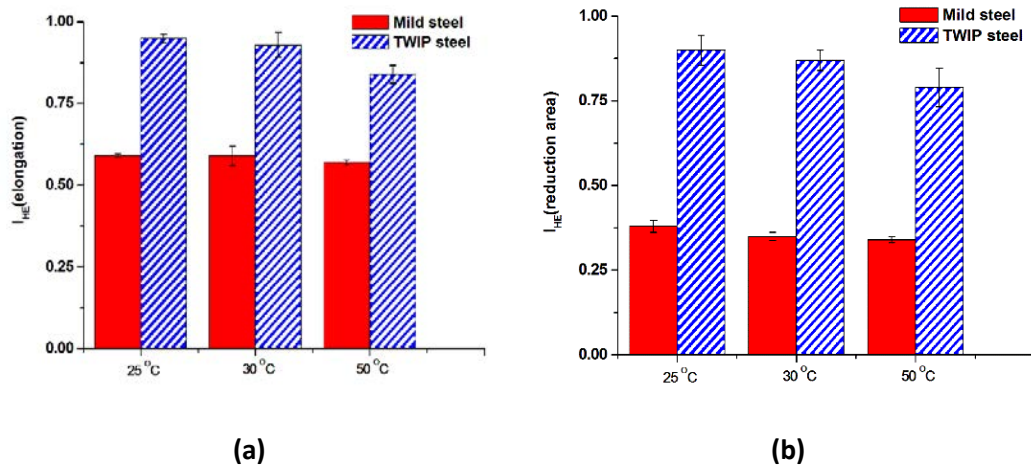


**Figure 7.6** The  $I_{HE}$  susceptibility indices (a) elongation and (b) reduction in area for mild steel and TWIP steel plotted in bar charts.

The  $I_{HIC}$  for TWIP steel on the other hand were close to unity; i.e. 0.99 with respect to % elongation for H-charged condition at room temperature. An increase in temperature only had a moderately decreasing effect on the HIC susceptibility for TWIP steel with ( $p=0.02$ ). The TWIP steel again showed values close to unity. The H-charged mild steel and TWIP steel specimen charged at 50 °C showed a lower  $I_{HIC}$  to the samples charged at other temperatures. This indicated the effect of h-interaction with the steels at 50 °C. Since the  $I_{HIC}$  for TWIP steel is still close to unity for each of the charged conditions compared to that of mild steel, it can be concluded that the HIC susceptibility of TWIP steel is very low compared to that of mild steel. The result can be attributed to the low hydrogen solubility due to high diffusivity in the pre-charged samples of TWIP steel.

## 7.6 Slow Strain Rate Testing of In-situ Charged Samples

Given that a high rate of hydrogen diffusion causes more hydrogen to arrive at crack tips and thus increases the susceptibility of steel to HIC, a second set of tests was performed. The tests aim to investigate the effect of hydrogen diffusivity on the tensile properties under continuous (in-situ) charged conditions. The stress-strain curves of the mild steel

samples tested previously at  $2 \times 10^{-4} \text{ s}^{-1}$  were compared to tests carried out on the uncharged and in-situ charged conditions at slow strain rate ( $5 \times 10^{-6} \text{ s}^{-1}$ ), as shown in Figure 7.7 and 7.8.

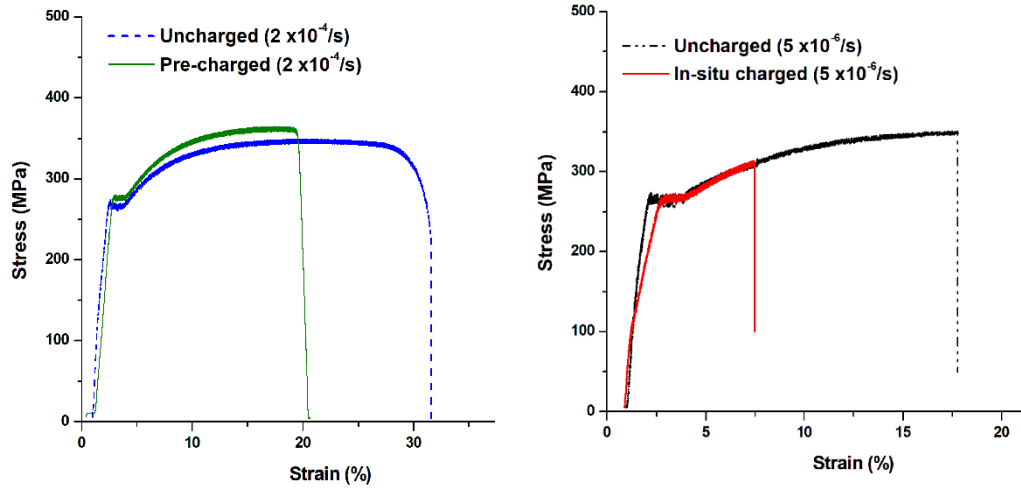


**Figure 7.7** Stress-strain plots of mild steel samples in: (a) pre-charged and (b) in-situ charged conditions.

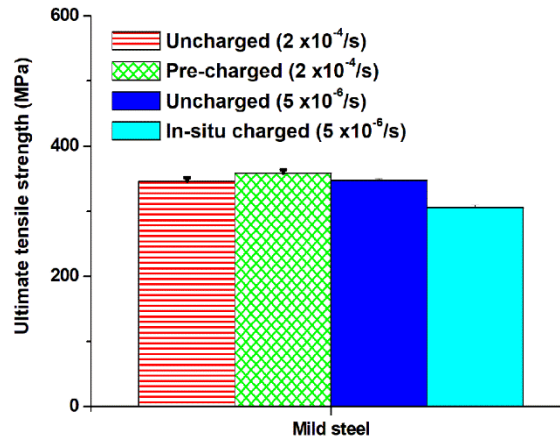


**Figure 7.8** Ultimate tensile strength of the mild steel samples plotted in bar charts.

The ultimate tensile strength (UTS) for the uncharged mild steel at a strain rate of  $2 \times 10^{-4} \text{ s}^{-1}$  was  $\sim 346 \text{ MPa}$ . The UTS was higher:  $359 \text{ MPa}$ , when pre-charged with hydrogen at the same strain rate. At the slow strain rate of  $5 \times 10^{-6} \text{ s}^{-1}$ , the UTS of the uncharged mild

steel was 347 MPa, which was similar to the result obtained at the higher strain rate (346 MPa). Interestingly, at the slow strain rate and in-situ charged condition, the UTS for the charged mild steel sample decreased by  $\sim 12\%$  to 305 MPa when compared to uncharged sample (Figure 7.8).

Figure 7.9 shows the plot of the % elongation of the mild steel plotted as bar charts. Relative to the original specimen, the fractured mild steel exhibited an 18% reduction in  $\% \mathcal{E}_f$  as compared to the uncharged sample. The loss in ductility is expected, as the steel was subjected to continuous charging for an extended period of time, and the high hydrogen solubility in steel and the continuous availability of more hydrogen arriving at crack site due to the tension applied should further enhance the HIC susceptibility when compared to the pre-charged sample.

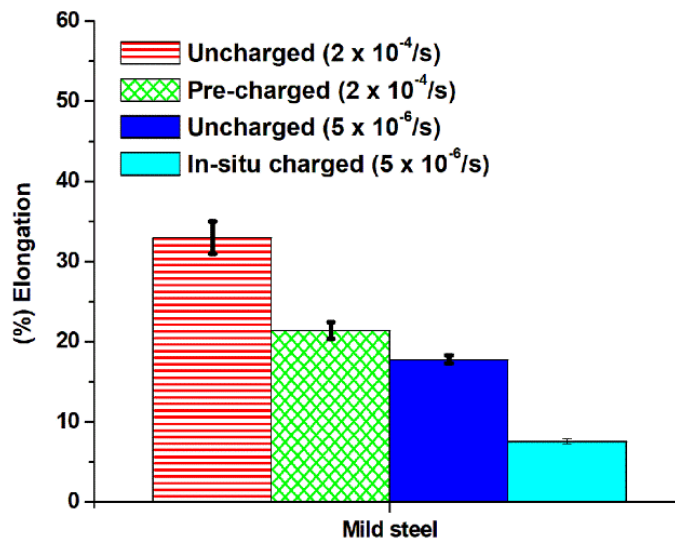


**Figure 7.9 % elongation ( $\mathcal{E}_f$ ) of mild steel samples plotted in bar charts.**

On the other hand, the TWIP steel samples generally (Figure 7.10 and 7.11) showed higher mechanical properties as compared to mild steel under similar test conditions. The UTS, at the strain rate of  $2 \times 10^{-4} s^{-1}$ , was  $\sim 1029$  MPa for the uncharged sample. It

decreased by about 0.9% for the pre-charged sample. The UTS value at the slow strain rate ( $5 \times 10^{-6} \text{ s}^{-1}$ ) for the uncharged TWIP steel was 1016 MPa. This value was significantly reduced by ~33% to ~681 MPa for the in-situ charged sample.

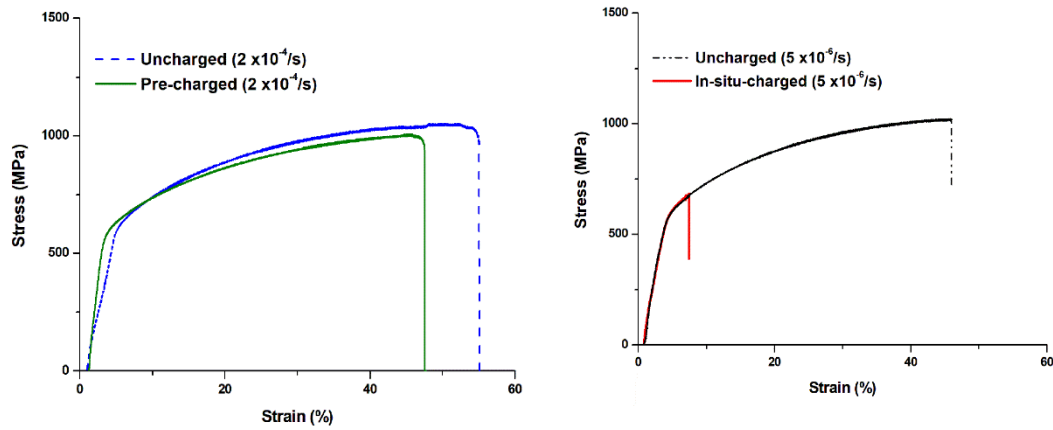


**Figure 7.10 Stress-strain plots of TWIP steel samples in: (a) pre-charged and (b) in-situ charged conditions.**

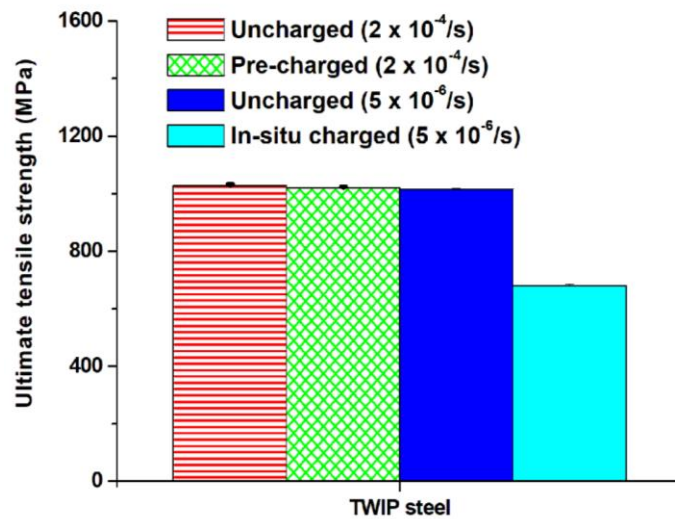


**Figure 7.11 Ultimate tensile strength of the TWIP steel samples plotted in bar charts.**

Hence, in the in-situ charged condition at this strain rate ( $5 \times 10^{-6} \text{ s}^{-1}$ ), the  $\% \mathcal{E}_f$  of the TWIP steel was significantly reduced (by ~83%), as shown in Figure 7.12. Also, in comparison to the pre-charged sample there was a significant loss of ductility. The loss



in ductility can be attributed to the high hydrogen mobility along the grain boundaries, which is continuously made available at crack tips and defect site, which further enhanced HIC in the steel.

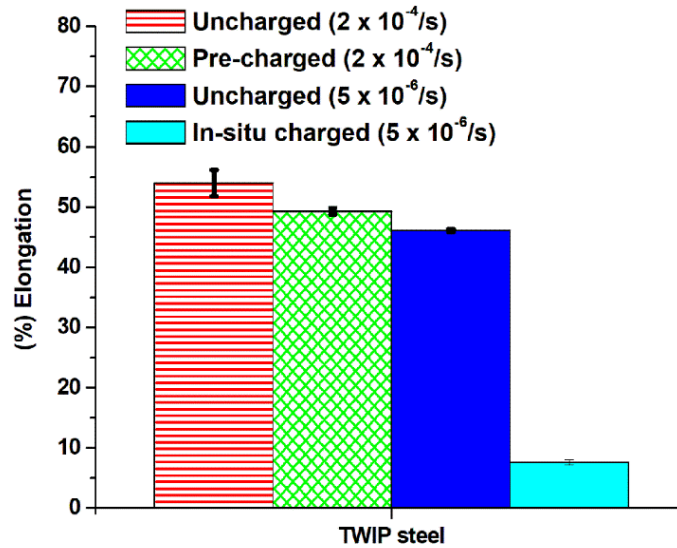
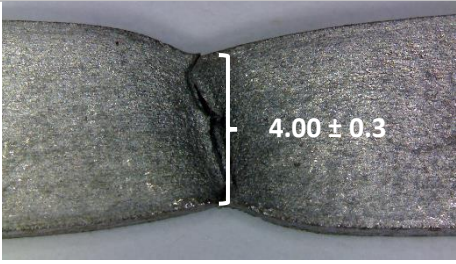
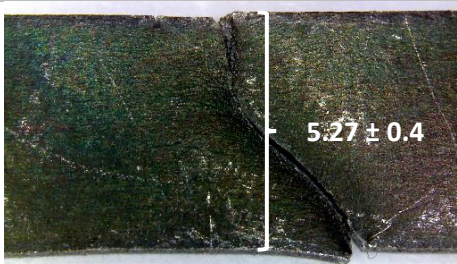
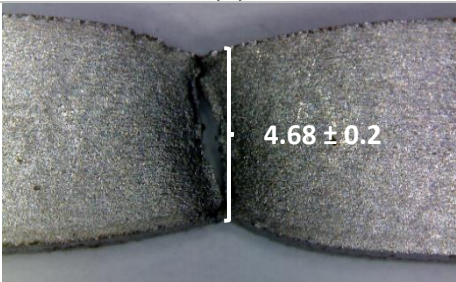
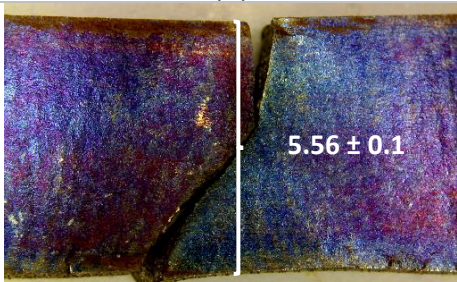


Figure 7.12 % elongation ( $\mathcal{E}_l$ ) of TWIP steel samples plotted in bar charts.

## 7.7 Macrographs of Fractured Samples

The macrographs of the fractured mild steel and TWIP steel samples under the uncharged and hydrogen pre-charged and in-situ charged conditions are shown in Plate 7.4. In comparison, the charged mild steel sample exhibited ~12% *RA* which is smaller by 40% to that exhibited by the uncharged sample at the same slow strain rate. Interestingly, the % *RA* exhibited at the slow strain rate was smaller by about 20% than at the high strain rate. This is consistent with the strain rate sensitivity as reported in the literature (Roth and Mohr 2014). The loss of this mechanical property in the in-situ charged sample at the slow strain rate can therefore be attributable partly to the continuous charging and high hydrogen concentration at possible crack sites.

| Mild steel  |  |
|---|--|
| Uncharged   | Charged  |
|  |  |
| (a)   | (b)  |
|  |  |
| (c)   | (d)  |

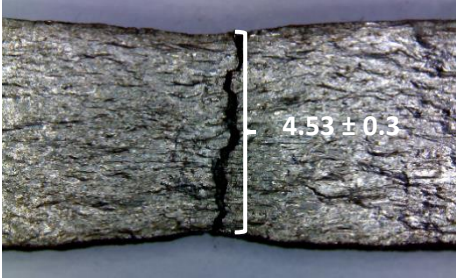
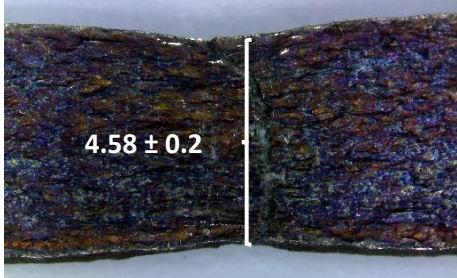
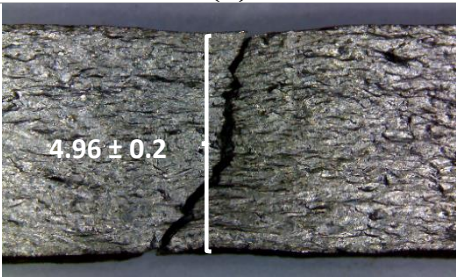
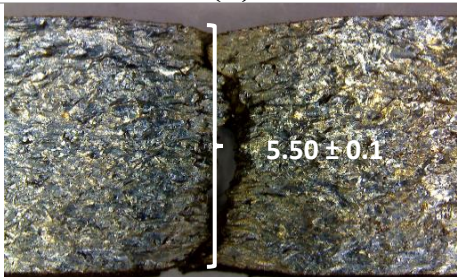
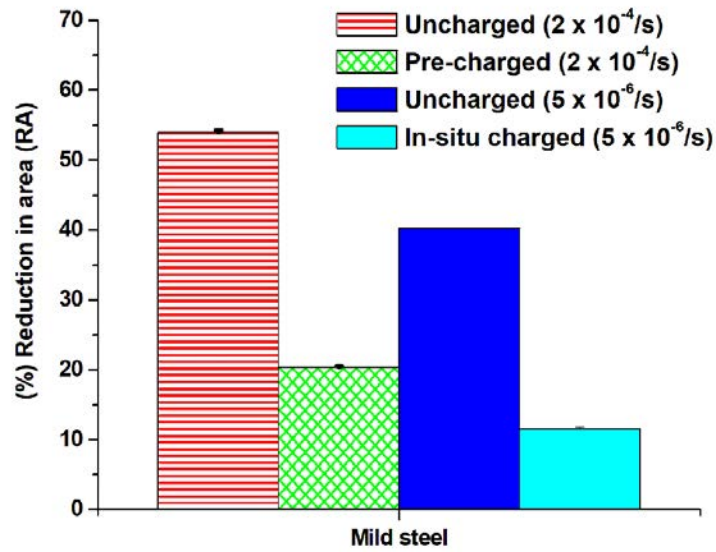
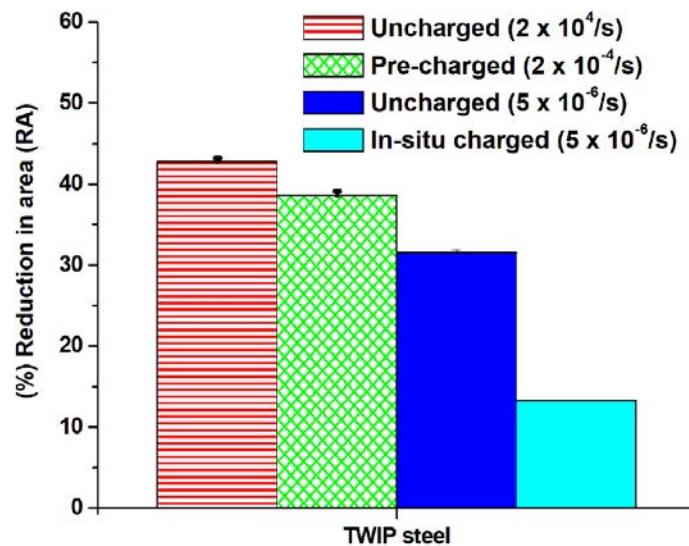
| TWIP steel  |  |
|---|--|
| Uncharged   | Charged  |
|  |  |
| (a)   | (b)  |
|  |  |
| (c)   | (d)  |
|   | 5 mm   |

Plate 7.4 Macrographs of the fractured tensile specimen of uncharged and charged steels at the strain rates  $2 \times 10^{-4}$ /s (a, b) and  $5 \times 10^{-6}$ /s (c, d).



**Figure 7.13 % reduction in area (*RA*) of mild steel samples plotted in bar charts.**

For the TWIP steel sample tested at slow strain rate, the % *RA* was similarly lower compared to the test done with high strain rate by ~23%. At the slow strain rate, the uncharged TWIP steel exhibited 32 % *RA*, which was higher by ~60% when compared to the in-situ hydrogen charged sample (Figure 7.14).



**Figure 7.14 % reduction in area (*RA*) of TWIP steel samples plotted in bar charts.**

The reduction in ductility as a result of lower values of % *RA* for hydrogen charged steels suggested that some form of HIC was occurring. However, the reduction in the mechanical properties was higher in mild steel compared to TWIP steel under the pre-charged condition. In the in-situ charged condition, both steels exhibited reduced mechanical properties, with TWIP steel showing a more severe effect. Hence, the influence of hydrogen on mild steel was therefore more severe in the pre-charged condition, but this was reversed in in-situ charged condition. It was previously reported that diffusion in TWIP steel was higher than in mild steel due to the hydrogen diffusion primarily in the grain boundary. Therefore, in in-situ charged conditions, hydrogen was made available faster at the crack tips, causing TWIP steel to experience more HIC.

## **7.8 Fractography Analysis**

The respective fracture surfaces of the mild steel in the uncharged and hydrogen charged conditions are shown in Plate 7.5. For clarity, the uncharged, pre-charged and in-situ-charged fractured surfaces are displayed. The fractured surface at the centre of the uncharged mild steel strained at  $2 \times 10^{-4} \text{ s}^{-1}$  revealed a relatively uniform distribution of spherical dimple features and micro-voids, which is a well-known characteristic of ductile fracture. However, a noticeable difference was observed in the pre-charged samples at this strain rate. The mild steel revealed a brittle failure, shown by transgranular cracking characterised by cleavage steps, river patterns and feather markings. The intergranular features were previously observed where hydrogen became trapped along the grain boundaries. The micro-voids disappeared, but the intergranular features observed could have occurred as a result of the hydrogen interaction with the sample.



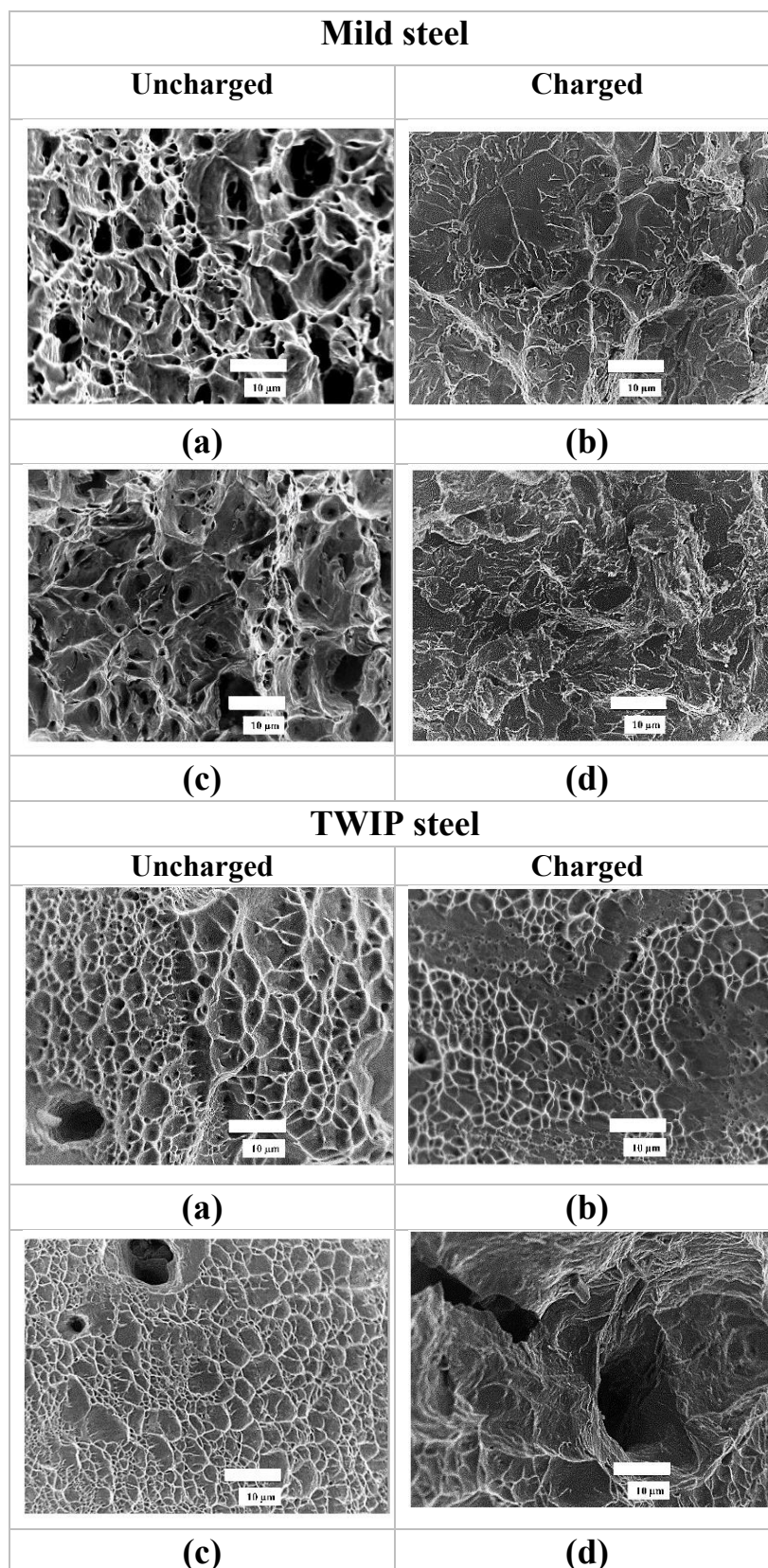


**Plate 7.5** Fractured surfaces showing centre section of uncharged and charged steels at the strain rates  $2 \times 10^{-4}/s$  (a, b) and  $5 \times 10^{-6}/s$  (c, d).

The samples tested at the low strain rate showed distinct features: the uncharged sample also revealed dimples which with smaller size of micro-voids compared to the uncharged sample at a higher strain rate (Plate 7.5). In addition, this sample revealed some cracks which were not observed at the high strain rate. Evidently, slow (lower) strain rate create more cracks. This could be responsible for the lower tensile properties displayed by the steel at the low strain rate and reported as strain rate sensitivity (Roth and Mohr 2014). Brittle features can be observed in the in-situ charged sample, similar to that observed in the pre-charged condition.

The fracture surfaces for TWIP steel in the uncharged condition tested at the high strain rate is shown in Plate 7.5. The sample revealed a series of ductile features, showing a relatively uniform distribution of fine dimples and a number of visible micro-voids, which are also consistent with ductile failures. Fracture surfaces for TWIP steel in pre-charged conditions at the high strain rate similarly showed a series of distribution of very fine dimples. The dimples appeared fewer, shallower and smaller compared to the uncharged sample, but are still features consistent with a ductile failure. It should be mentioned, however, that though a ductile failure was observed, hydrogen has influence the dimples, but the effect was not severe since no features consistent with brittle fracture were revealed. At a lower strain rate, the uncharged TWIP steel showed fewer micro-voids compared to that at high strain rate. The dimples also appeared to be shallower, suggesting that the low strain rate had some effect on the properties of the steel. When the samples were strained at this slow strain rate in-situ charged condition, multiple features were observed: some isolated areas of dimples were revealed at the lower left of Plate 7.5, and a mixed mode of transgranular, intergranular and quasi brittle cracks characterised by tear ridges were also observed. As compared to the pre-charged sample, the in-situ charged TWIP steel exhibited more cracks consistent with brittle failure.

## 7.9 HIC Susceptibility

To quantify the HIC susceptibility of the steels, the hydrogen induced cracking indices ( $I_{HIC}$ ) were calculated based on the ratio of the mechanical property (such as %  $\mathcal{E}_f$  and % $RA$ ) measured in hydrogen charged compared to its corresponding measurement in uncharged condition. A low  $I_{HIC}$  suggested a high HIC susceptibility, and  $I_{HIC}$  value close to unity indicated no significant effect due to hydrogen charging. The calculated values of  $I_{HIC}$  for the steels are presented in Table 7.2 and Figure 7.15.

Table 7.2 The  $I_{HE}$  susceptibility indices for mild steel and TWIP steel

| Temperature (°C) | $\mathcal{E}_f$ | $RA$ | $\mathcal{E}_f$ | $RA$ |
|------------------|-----------------|------|-----------------|------|
| Pre-charged      | 0.65            | 0.38 | 0.91            | 0.90 |
| In-situ charged  | 0.43            | 0.28 | 0.17            | 0.42 |

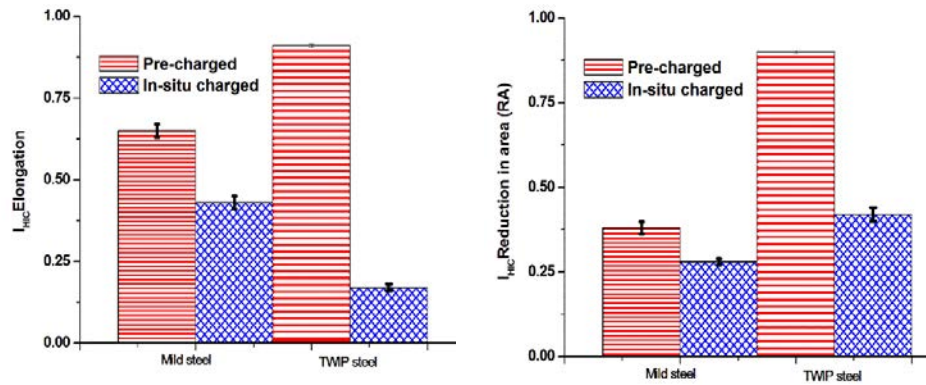


Figure 7.15 The  $I_{HIC}$  susceptibility indices (a) elongation and (b) reduction in area for mild steel and TWIP steel plotted in bar charts.

The mild steel showed high HIC susceptibility in both the pre-charged condition (strain rate  $2 \times 10^{-4} \text{ s}^{-1}$ ) and in-situ charged conditions. For the mild steel at pre-charged condition and room temperature, the  $I_{HIC}$  was found to be 0.65 with respect to %  $\mathcal{E}_f$ , and 0.38 with respect to % $RA$ . In the in-situ charged condition, as expected, the susceptibility

to HIC increased by more than 25%, as more hydrogen was available for diffusion to the cracks sites during in-situ charging. The TWIP steel, however, showed less susceptibility in the pre-charged condition when compared to mild steel.

The  $I_{HIC}$  was found to be 0.91 and 0.91 with respect %  $\epsilon_f$  and %  $RA$ , respectively. This is because the high diffusion of hydrogen did not leave enough room for hydrogen to be dissolved in the steel. Interestingly, however, during in-situ charging the TWIP steel showed high susceptibility. This can be attributed to the high diffusion rate in the TWIP steel grain boundaries, as shown in chapter 6, and the effect of strain rate which is severe in slow strain rate (Hinton and Procter 1983, Roth and Mohr 2014), probably because the initiation of cracks allowed more available hydrogen to be trapped and therefore reduced ductility. Hence, during pre-charging TWIP steel experienced ductile failure because hydrogen generation was discontinued and the concentration per unit grain was low enough in the steel to cause substantial damage. However, this was reversed in the in-situ condition: the sample was continuously charged, and as the rate of diffusion of hydrogen was high through the grain boundaries in TWIP steel, more hydrogen became available to diffuse to crack tips. Thus, because of the high hydrogen diffusivity in TWIP steel grain boundaries, the cracks are easily propagated at slow strain rate. This is consistent with the multiple features observed: dimples, intergranular and quasi brittle feature in TWIP steel.

## 7.10 Summary

The HIC susceptibility of TWIP steel was studied using a tensile test method at two different strain rates, in hydrogen pre-charged and in-situ charged conditions. The results were compared to those from mild steel. Based on the susceptibility indices ( $I_{HIC}$ ), the resistance to HIC suggested that TWIP steel was more resistant than mild steel in pre-



charged condition due to low hydrogen solubility from the high diffusion rate. The resistance however decreases in in-situ charged conditions more significantly in TWIP steel than in mild steel. The results were attributed to the higher level of hydrogen available for diffusion in in-situ charged condition than in pre-charged condition.

## Chapter 8      Conclusions

The effective hydrogen permeation and hydrogen induced cracking behaviour of ultrahigh-strength steels (nanostructured bainitic steels and TWIP steel) were compared to mild steel using electrochemical techniques, in an environment which replicated industry conditions in which there is high hydrogen evolution as a result of cathodic protection. Electrochemical permeation results showed that the effective hydrogen diffusivity in nanostructured bainitic steel was lower compared to mild steel. The microstructural differences played a significant role in lowering hydrogen diffusion in BS-200 as compared to BS-350 and mild steel. The effective hydrogen diffusivity in the steels was found to increase with increases in temperature, but the increase was still small in BS-200 compared to BS-350 and mild steel. Depth profiling analyses carried out on the steel by hardness test and ERDA showed that the concentration of hydrogen was more limited to the subsurface region of BS-200 than in BS-350 and mild steel, suggesting that BS-200 will be less susceptible to HIC.

The hydrogen permeability rate for the TWIP steel was significantly lower than that of mild steel but the effective hydrogen diffusivity was higher in the TWIP steel than in the mild steel at all different test temperatures. Based on the activation energy calculation and the absence of any significant irreversible traps, it was concluded that the diffusion path in TWIP steel was primarily through the grain boundaries. The result of the HIC susceptibility of TWIP steel based on susceptibility indices ( $I_{HIC}$ ) suggested that TWIP steel was more resistant than mild steel in pre-charged conditions due to low solubility. The resistance however decreases under in-situ charged conditions more in TWIP steel than in mild steel.

## References

- Aeiyaeh, S., Zaid, B., Lacaze, P. C. (1999). "A one-step electrosynthesis of PPy films on zinc substrates by anodic polymerization of pyrrole in aqueous solution." *Electrochim. Acta*, 44, 2889-2898.
- Addach, H., Bercot, P., Rezrazi, M., Wery, M. (2005). "Hydrogen permeation in iron at different temperatures." *Mater. Lett.*, 59, 1347-1351.
- Agmetalminer Inc. "Metal prices." <http://agmetalminer.com/metal-prices/titanium>. Accessed 18 October 2018.
- Akiyama, E., Matsukado, K., Li, S. (2011). "Constant-load delayed fracture test at atmospherically corroded high strength steels." *Appl. Surf. Sci.*, 257, 8275-8281.
- Arafin, M. A., Szpunar, J. A. (2011). "Effect of bainitic microstructure on the susceptibility of pipeline steels to hydrogen induced cracking." *Mater. Sci. Eng. A*, 528, 4927-4940.
- Asano, S., Otsuka, R. (1976). "The lattice hardening due to dissolved hydrogen in iron and steel." *Scripta Metall. Mater.*, 10, 1015.
- Bai, Y., Momotani, Y., Chen, M. C., Shibata, A., Tsuji, N. (2016). "Effect of grain refinement on hydrogen embrittlement behaviours of high-Mn TWIP steel." *Mater. Sci. Eng. A*, 651, 935-944.
- Barnoush, A., Asgari, M., Johnsen, R. (2012). "Resolving the hydrogen effect on dislocation nucleation and mobility by electrochemical nanoindentation." *Scripta Mater.*, 66, 414-417.
- Beck, W., Bockris, J. O., McBreen, J. (1965). "Hydrogen permeation in metals as a function of stress, temperature and dissolved concentration." *P. R. Soc. London*. DOI: 10.1098/rspa.1966.0046, 5, 220-235.
- Beladi, H., Adachi, Y., Timokhina, I., Hodgson, P. D. (2009). "Crystallographic analysis of 218 nanobainitic steels." *Scripta Mater.*, 60, 455-458.
- Boiadjieva, T., Mirkova, L., Kronberger, K., Steck, T., Monev, M. (2013). "Hydrogen permeation through steel electroplated with Zn or Zn-Cr coatings." *Electrochim. Acta*, 114, 790-798.
- Bouaziz, O., and Guelton, N. (2001). "Modelling of TWIP effect on work-hardening". *Mater. Sci. Eng. A*, 319-321, 484-487.
- Brass, A. M., Chene, J., Gonzalez, J. (1994). "Tritium distribution at the crack tip of high-strength steels submitted to stress corrosion cracking." *Metall. Trans. A*, 25, 1159-1167.

Brass, A. M., and Chanfreau, A., (1990). "Electrochemical permeation hydrogen in high purity nickel at 100 °C." *Scripta Metall. Mater.*, 24, 499-504

Caballero, F. G., and Bhadeshia, H. K. D. H. (2004). "Very strong bainite." *Curr. Opin. Solid St. M.*, 8, 251–257.

Caballero, F. G., Miller, M. K., Babu, S. S., Garcia-Mateo, C. (2007). "Atomic scale observations of bainite transformation in a high carbon high silicon steel." *Acta Mater.*, 55, 381-390.

Chang, K. D., Gu, J. L., Fang, H. S., Yang, Z. G., Bai, B. Z., Zhang, W. Z. (2001). "Effects of heat-treatment process of a novel bainite/martensite dual-phase high strength steel on its susceptibility to hydrogen embrittlement." *ISIJ Int.*, 41, 1397-1401.

Chen, S. S., Wu, T. I., Wu, J. K. (2004). "Effects of deformation on hydrogen degradation in a duplex stainless steel." *J. Mater. Sci.*, 39, 67-71.

Chin, K. G., Kang, C. Y., Sin, S. Y., Hong, S., Lee, S., Kim, H. S., Kim, K. H., Kim, N. J. (2011). "Effects of Al addition on deformation and fracture mechanisms in two high manganese TWIP steels." *Mater. Sci. Eng. A*, 528, 2922-2928.

Chou, S., Tsai, W. (1999). "Effect of grain size on the hydrogen-assisted cracking in duplex stainless steels." *Mater. Sci. Eng. A*, 270, 219-224.

Cwiek, J. (2010). "Prevention methods against hydrogen degradation of steel." *J. of Achiev. Mater. Manuf. Eng.*, 43, 214-221.

Dadfarnia, M. Novak, P., Ahn, D. C., Liu, J. B., Sofronis, P. (2010). "Recent advances in the study of structural materials compatibility with hydrogen." *Adv. Mater.*, 22, 1128-1135.

Dailymetal. "Current prices of metallic materials." <http://www.dailymetalprice.com>. Accessed 18 October 2018.

Dean, F. W. H. (2005). "Measurement of hydrogen permeation through structural steel sections of varying thickness at 19 °C." *Mater Sci. Technol.*, 21, 347-351.

Depover, D., Escobar, P., Wallaert, E., Zermout, Z., Verbeken, K. (2014). "Effect of hydrogen charging on the mechanical properties of advanced high strength steels." *Int. J. Hydrogen. Energ.*, 39, 4647-4656.

Depover, T., Eeckhout, E. V., Verbeken, K. (2016). "The impact of hydrogen on the ductility loss of bainitic Fe-C alloys." *Mater. Sci. Tech-Lond.*, 32, 1625-1631.

Devanathan, M. A. V., Stachurski, Z. (1962). "The adsorption and diffusion of electrolytic hydrogen in palladium." *P. R. Soc. A*, 270, 90-102.

Djukic, M. B., Zeravcic, V. S., Bakic, G., Sedmak, A., Rajicic, B. (2014). "Hydrogen embrittlement of low carbon structural steel." *Procedia Mater. Sci.*, 3, 1167-1172.

Dong, C. F., Liu, Z. Y., Li, X. G., Cheng, Y. F. (2009). "Effects of hydrogen-charging on the susceptibility of X100 pipeline Steel to hydroegn –induced cracking." *Int. J. Hydrogen Energ.*, 34, 9879-9884.

Duprez, L., Verbeken, K., Verhaege, M. (2008). "Effect of hydrogen on the mechanical properties of multiphase high strength steels." *Proceedings of the 2008 International Hydrogen Conference*, 62-69.

Elhoud, A. M., Renton, N. C., Deans, W. F. (2010). "Hydrogen embrittlement of super duplex stainless steel in acid solution." *Int. J. of Hydrogen Energ.*, 35, 6455-6464.

Escobar, D. P., Minambres, C., Duprez, L., Verbenken, K., Verhaege, M. (2011). "Internal and surface damage of multiphase steels and pure iron after electrochemical hydrogen charging." *Corros. Sci.*, 53, 3166-3176.

Escobar, D. P., Verbeken, K., Duprez, L., Verhaege, M. (2012). "Evaluation of hydrogen trapping in high strength steels by thermal desorption spectroscopy." *Mater. Sci. Eng. A*, 551, 50-58.

Fielding, L. C. D., Song, E. J., Han, D. K., Bhadeshia, H. K. D. H., Suh, D. W. (2014). "Hydrogen diffusion and the percolation of austenite in nanostructured bainitic steel." *P. R. Soc. Lond. A-Conta.*, 470, 1-13.

Garcia-Mateo, C., Caballero, F. G., Bhadeshia, H. K. D. H. (2003). "Hard bainite." *ISIJ Int.* 43, 1238-1243.

Hardie, D., Charles, E. A., Lopez, A. H. (2006). "Hydrogen embrittlement of high strength pipeline steels." *Corros. Sci.* 48, 4378 - 4385.

Han, D. K., Lee, S. K., Noh, S. J., Kim, S. K., Suh, D. W. (2005). "Effect of aluminium on hydrogen permeation of high-manganese twinning-induced plasticity steel." 99, 45-48.

Han, D. K., Kim, Y. M., Han, H. N., Bhadeshia, H. K. D. H., Suh, D.-W. (2014). "Hydrogen and aluminum in high-manganese twinning-induced plasticity steel." *Scripta Mater.*, 80, 9-12.

Haq, A. J., Muzaka, K., Dunne, D. P., Calka, A., Pereloma, E. V. (2013). "Effect of microstructure and composition on hydrogen permeation in X70 pipeline steels." *Int. J. Hydrogen. Energ.*, 38, 2544-2556.

Hinton, B. R. W., Procter, R. P. M., (1983). "The effect of strain-rate and cathodic potential on the tensile ductility of X-65 pipeline steel." *Corros. Sci.*, 23, 101-123.

Hilditch, T. B., Lee, S. B., Speer, J. G. (2003). "Response to hydrogen charging in high strength automotive sheet steel products." *SAE Technical Paper*; doi:10.4271/2003-01-0525.

- Hirth, J. P. (1980). "Effects of hydrogen on the properties of iron and steel." *Metall. Trans. A*, 11, 861-890.
- Hong, G. W., Lee, J. Y. (1983). "Discussion of permeation measurements of hydrogen trapping in 1045 steels." *Metall. Mater. Trans. A*, 14, 156-58.
- Huang, F., Liu, J., Deng, Z. J., Cheng, J. H., Lu, Z. H., Li, X. G. (2010). "Effect of microstructure and inclusions on hydrogen induced cracking susceptibility and hydrogen trapping efficiency of X120 pipeline steel." *Mater. Sci. Eng. A*, 527, 6997–7001.
- Ichitani, K., Kanno, M. (2003). "Visualization of hydrogen diffusion in steels by high sensitivity hydrogen microprint technique." *Sci. Technol. Adv. Mater.*, 4, 545-551.
- Kacar, R. (2004). "Effect of solidification mode and morphology of microstructure on the hydrogen content of duplex stainless weld metal." *Mater Design*, 25, 1-9.
- Kannan, M. B., Raja, V. S. (2006). "Evaluation of hydrogen embrittlement susceptibility of over aged 7010 Al alloy." *J. Mater. Sci.*, 41, 5495-5499.
- Kannan, M. B., Dietzel, W., Raman, R. K. S. (2007). "Hydrogen-induced cracking in magnesium alloy under cathodic polarization." *Scripta Mater.*, 57, 579-581.
- Kappes, M., Iannuzzi, M., Rebak, R. B., Carranza, R. M. (2014). "Sulfide stress cracking of nickel-containing low-alloy steels." *Corros. Rev.*, 32, 101-128.
- Karz, Y., Tymiak, N., Gerberich, W. W. (2001). "Nano-mechanical probes as new approaches to hydrogen/deformation interaction studies." *Eng. Fract. Mech.*, 68, 619-646.
- Kazum, O., Kannan, M., Beladi, H., Timokhina, I. B., Hodgson, P. D., Khoddam, S. (2014). "Aqueous corrosion performance of nanostructured bainitic steel." *Mater. Design*, 54, 67-71.
- Kazum, O., Kannan, M., Beladi, H., Timokhina, I. B., Hodgson, P. D., Khoddam, S. (2013). "Selective dissolution of retained austenite in nano-bainitic steel." *Adv. Eng. Mater.*, 15, 1-3.
- Kirchheim, R. (2012). "Solid solution softening and hardening by mobile solute atoms with special focus on hydrogen." *Scripta Mater.*, 67, 767-770.
- Kim, W. K., Koh, S. U., Yang, B. Y., Kim, K. Y. (2008). "Effect of environmental and metallurgical factors on hydrogen induced cracking of HSLA steels." *Corros. Sci.* 50, 3336-3342.
- Kim, S. J., Yun, D. W., Suh, D. W., Kin, K. Y. (2012). "Electrochemical hydrogen permeation measurement through TRIP steel under loading condition of phase transition." *Electrochem. Commun.*, 24, 112-115.

- Kim, Y., Kim, Y., Kim, D., Kim, S., Nam, W., Choe, H. (2011). "Effects of hydrogen diffusion on the mechanical properties of austenite 316L steel at ambient temperature." *Mater. Trans.*, 52, 507-513.
- Kimura, A., Birnbaum, H. K. (1988). "Hydrogen induced grain boundary fracture in high purity nickel and its alloys-enhanced hydrogen diffusion along grain boundary." *Acta Metall. Mater.*, 36, 757-766.
- Kishi, A., Takano, N. (2010). "Effect of hydrogen cathodic charging on fatigue fracture of type 310S stainless steel." *J. Phys. Conf. Ser.*, 240 012050, 1-4.
- Koyama, M., Springer, H., Merzlikin, S. V., Tsuzaki, K., Akiyama, E., Raabe, D. (2014). "Hydrogen embrittlement associated with strain localization in a precipitation-hardened Fe-Mn-Al-C light weight austenitic steel." *Int. J. Hydrogen Energ.*, 39, 4634-4646.
- Koyama, M., Akiyama, E., Tsuzaki, K. (2012). "Hydrogen embrittlement in a Fe-Mn-C ternary twinning-induced plasticity steel." *Corros. Sci.*, 54, 1-4.
- Kumnick, A. J., Johnson, H. H. (1980). "Deep trapping states for hydrogen in deformed iron." *Acta Metall. Mater.*, 28, 33-39.
- Kusakin, P., Belyakov, A., Haase, C., Kaibyshev, R., Molodov, D. A. (2014). "Microstructure evolution and strengthening mechanisms of Fe-23Mn-0.3C-1.5Al TWIP steel during cold rolling." *Mater. Sci. Eng. A*, 617, 52-60.
- Li, Y., Zhao, L., Pan, H. (2013). "Hydrogen permeation behavior and associated phase transformation in annealed AISI304 stainless steel." *Mater. Struct.*, 46, 621-627.
- Loidl, M., Kolk, O. (2011). "Hydrogen embrittlement in HSSs limits use in lightweight body." *Adv. Mat. Res.*, 169, 22-25.
- Lunarska, E., Ososkov, Y., Jagodzinsky, Y. (1997). "Correlation between critical hydrogen concentration and hydrogen damage of pipeline steel." *Int. J. Hydrogen Energ.*, 22, 279-284.
- Luu, W. C., Liu, P. W., Wu, J. K. (2002). "Hydrogen transport and degradation of a commercial duplex stainless steel." *Corros. Sci.*, 44, 1783-1791.
- Luu, W. C., Wu, J. K. (1996) "The influence of microstructure on hydrogen transport in carbon steels." *Corros. Sci.*, 38, 239-245.
- Luppo, M. I., Hazarabedian, A., Ovejero-Garcia, J. (1999). "Effects of delta ferrite on hydrogen embrittlement of austenitic stainless steel welds." *Corros. Sci.*, 41, 87-103.
- Mayer M., SIMNRA User's Guide, Report IPP9/113, Max-Planck Institut für Plasmaphysik, Garching, Germany, (1997).
- Mateo, C. G., Caballero, F. G., Bhadeshia H. K. D. H. (2003). "Acceleration of low-temperature bainite." *ISIJ Int.*, 43, 1821-1825.

Ningshen, S., Uhlemann, M., Schneider, F., Khatak, H. S. (2001). ‘Diffusion behaviour of hydrogen in nitrogen containing austenitic alloys.’ Corros. Sci. 43, 2255-2264.

Nishimura, R., Shiraishi, D., Maeda, Y. (2004) “Hydrogen permeation and corrosion behaviour of high strength steel MCM 430 in cyclic wet-dry SO<sub>2</sub> environment.” Corros. Sci. 46, 225-243.

Novak, P., Yuan, R., Somerday, B. P. (2010). “A statistical physical-based, micro-mechanical model of hydrogen-induced intergranular fracture in steel.” J. Mech. Phys. Solids, 58, 206-226.

Olden, V., Thaulow, C., Johnsen, R. (2008). “Modelling of hydrogen diffusion and hydrogen induced cracking in supermartensitic and duplex stainless steels.” Mater. Design, 29, 1934– 48.

Padhy, G. K., Ramasubbu, V., Parvathavarthini, N., Wu, C. S. (2015). “Influence of temperature and alloying on the apparent diffusivity of hydrogen in high strength steel.” Int. J. Hydrogen Energ., 40, 6714-6725.

Park, I. J., Jeong, K. H., Jung, J. G., Lee, C. S., Lee, Y. K. (2012). “The mechanism of enhanced resistance to the hydrogen delayed fracture in Al-added Fe-18Mn-0.6C.” Int. J. Hydrogen Energ., 37, 9925-9932.

Park, Y. D., Maroef, I. S., Landau, A., Olson, D. L. (2002) “Retained austenite as a hydrogen trap in steel welds.” Weld. Res. 81, 27-35.

Park, G. T., Koh, S. U., Jung, H. G., Kim, K. Y. (2008). “Effect of microstructure on the hydrogen trapping efficiency and hydrogen induced cracking of linepipe steel.” Corros. Sci., 50, 1865-1871.

Park, I-J., Lee, S -M., Jeon, H-H., Lee, Y-K. (2015). “The advantage of grain refinement in the hydrogen embrittlement of Fe-18Mn-0.6C twinning-induced plasticity steel.” Corros. Sci., 93, 63–69.

Peet, M., Babu, S. S., Miller, M. K., and Bhadeshia, H. K. D. H. (2004). “Three-dimensional atom probe analysis of carbon distribution in low-temperature bainite.” Scripta Mater., 50, 1277-1281.

Perng, T. P., and Altstetter, C. J. (1987). “Comparison of hydrogen gas embrittlement of austenitic and ferritic stainless steels.” Metall. Trans. A. 18A, 123-34.

Perng, T., Johnson, M., Altstetter, C. J. (1989). “Influence of plastic deformation on hydrogen and permeation in stainless steels.” Acta Metall. Mater. 37, 3393-3397.

Pressouyre, G. M., Bernstein, I. M. (1979). “A kinetic trapping model for hydrogen-induced cracking.” Acta Metall. Mater., 27, 89-100.

Pyng, P., Altstetter, C. J. (1986). “Effects of deformation on hydrogen permeation in austenitic stainless steels.” Acta Metall. Mater., 34, 1771– 1781.



- Qi, Y., Luo, H., Zheng, S., Chen, C., Lv, Z., Xiong, M. (2014). "Comparison of tensile and impact behaviour of carbon steel in H<sub>2</sub>S environments." *Mater. Design*, 58, 234-41.
- Robertson, W. M., and Thompson, A. W. (1980). "Permeation measurements of hydrogen trapping in 1045 steel." *Metall. Trans. A.*, 11A, 553-557.
- Ronevich, J.A., Speer, J.G., Maatlock, D. K. (2010). "Hydrogen Embrittlement of Commercially Produced." *Advanced High Strength Sheet Steels, SAE Int. J. Mater. Manuf.*, 3(1), 255-267.
- Roth, C. C., Mohr, D. (2014). "Effect of strain rate on ductile fracture initiation in advanced high strength steel sheets: experiments and modelling." *Int. J. Plasticity*, 56, 19-44.
- Ronevich, J. A., Kim, S. K., Speer, J. G., Matlock, D. K. (2012). "Hydrogen effects on cathodically charged twinning-induced plasticity Steel." *Scripta Mater.*, 66, 956-959.
- Sakamoto, Y., Katayama, H. (1982). "Electrochemical determination of diffusivity and solubility of hydrogen in an austenitic type 304 steel." *J. Jpn. Inst. Met.*, 46, 805-814.
- Scoppio, L., Barteri, M. (1994). "Methods of hydrogen uptake measurements by electrochemical permeation test on low alloy steels. In: Turnbull A, Editor. Hydrogen transport and cracking in metals. "Cambridge (UK): The University Press. 204-251.
- Siddiqui, R. A., Abdullah, H. A. (2005) "Hydrogen embrittlement in 0.31% carbon steel used for petrochemical applications." *Adv. Mater. Res-Switz.*, 170, 430-435.
- Skjellerudsveen, M, Akselsen, O. M., Olden, V., Johnsen, R., Smirnova, A. (2010). "Effect of microstructure and temperature on hydrogen diffusion in X70 grade pipeline steel and its weldments. In: Proceedings of EuroCorr, European Federation of Corrosion, Moscow.
- So, K. H., Kim, J. S., Shun, Y. S., Park, K. T., Lee, Y. K., Lee, C. S. (2009). "Hydrogen delayed fracture properties and internal hydrogen behavior of a Fe-18Mn-1.5Al-0.6CTWIP steel." *ISIJ int.* 49, 1952-1959.
- Stevens, M. F., Bernstein, I. M. (1989). "Microstructural trapping effects on hydrogen induced cracking of a microalloyed steel." *Metall. Trans. A*, 20A, 909-19.
- Szost, B. A., Vegter, R. H., Pedro, E. J., Castillo, R. A. (2013). "Hydrogen-trapping mechanisms in Nanostructured steels." *Metall. Mater. Trans. A*, 44A, 4542-4550.
- Szost, B. A., Vegter, R. H., Castillo, R. A. (2013). "Developing bearing steels combining hydrogen resistance and improved hardness." *Mater. Design*, 43, 499-506.
- Takai, K., Watanuki, R. (2003). "Hydrogen in trapping states innocuous to environmental degradation of high-strength steels." *ISIJ International*, 43, 520-526.

- Timokhina, I. B., Beladi, H., Xiong, X. Y., Adachi, Y., and Hodgson, P. D. (2011). "Nanoscale microstructural characterization of a nanobainitic steel." *Acta Mater.*, 59, 5511–5522.
- Tsuru, T., Latanision, R. M. (1982). "Grain boundary transport of hydrogen in nickel." *Scripta Metall. Mater.*, 16, 575-578.
- Turnbull, A., (1994). "Standardisation of Hydrogen permeation measurement by electrochemical technique, In: Hydrogen transport and cracking in metals." Division of Materials Metrology, UK, 129-141.
- Turnbull, A., Maria, M. S., Thomas, N. D. (1989). "The effect of H<sub>2</sub>S concentration and pH on hydrogen permeation in AISI 410 stainless steel in 5% NaCl." *Corros. Sci.*, 29, 89-104.
- Uhlemann, M., Chatterjee, U. K., Ningshen, S. (2002). "Studies on hydrogen embrittlement of nitrogen containing austenitic alloys." *Mater. Sci. Tech-Lond.*, 18, 1179-1187.
- Valentini, R., Salina, A. (1994). "Influence of microstructure on the hydrogen embrittlement behavior of 2.25Cr-1Mo steel." *Mater. Sci. Tech-Lond.*, 10, 908-914.
- Venezuela, J., Liu, Q., Zhang, M., Zhou, Q., Atrens, A. (2015). "The influence of hydrogen on the mechanical and fracture properties of some martensitic advanced high strength steels studied using the linearly increasing stress test." *Corros. Sci.* 99, 98–17.
- Worldsteelprice Inc. "Current prices of steels." <http://worldsteel price.com>. Accessed 18 October 2018.
- Xiukui, S., Jian, X., Yiyi, L. (1989). "Hydrogen permeation behavior in metastable austenitic stainless steels 321 and 304." *Acta Metall. Mater.*, 37, 2171-2176.
- Xu, J., Sun, X. K., Chen, W. X., Li, Y. Y. (1993). "Hydrogen permeation and diffusion in iron-based superalloys." *Acta Metall. Mater.*, 4, 1455-1459.
- Yang, H. K., Zhang, Z. J., Zhang, Z. F. (2013). "Comparison of work hardening and deformation twinning evolution in Fe-22Mn-0.6C-(1.5Al) twinning-induced plasticity steels." *Scripta. Mater.*, 68, 992-995.
- Yagodzinsky, Y., Todoshchenko, O. Papula, S., Hanninen, H. (2010). "Hydrogen solubility and diffusion in austenitic stainless steels studied with thermal desorption spectroscopy." Doi:10.1002/srin.201000227.
- Yoozbashi, M. N., Yazdani, S. (2011). "Mechanical properties of nanostructured, low temperature bainitic steel designed using a thermodynamic model." *Mater. Sci. Eng. A*, 527, 3200–3205.
- Younes, C. M., Steele, A. M., Nicholson, J. A., Barnett, C. J. (2013). "Influence of hydrogen content on tensile properties and fracture of austenitic stainless steel welds." *Int. J. Hydrogen Energ.*, 38, 4864-4876.

Zakroczyński, T., Glowacka, A., Swiatnicki, W. (2005). "Effect of hydrogen concentration on the embrittlement of a duplex stainless steel." *Corros. Sci.*, 47, 1403–1414.

Zan, N., Ding, H., Guo, X., Tang, Z., Bleck, W. (2015). "Effect of grain size on hydrogen embrittlement in a Fe-22Mn-0.6C TWIP steel." *Int. J. Hydrogen Energ.*, 40, 10687-10696.

Zappfe, C., Sims, C. (1941). "Hydrogen embrittlement, internal stress and defects in steels." *Trans. AIME* 145: 225–227.

Zheng, S., Zhou, C., Wang, P., Chen, C., Chen, L. (2013). "Effects of the temperature on the hydrogen permeation behaviour of L360NCS pipeline steel in 1Mpa H<sub>2</sub>S environments." *Int. J. Electrochem. Sc.*, 8, 2880-2891.

Zhou, C., Zheng, S., Chen, C., Lu, G. (2013). "The effect of the partial pressure of H<sub>2</sub>S on the permeation of hydrogen in low carbon pipeline steel." *Corros. Sci.*, 67, 184–92.